Study of deep Earth structure using body waves

by

Hrvoje Tkalčić

Diploma of Physics (University of Zagreb) 1996

A dissertation submitted in partial satisfaction of the requirements for

the degree of

Doctor of Philosophy

in

Geophysics

in the

GRADUATE DIVISION

of the

UNIVERSITY of CALIFORNIA at BERKELEY

Commitee in charge:
Professor Barbara Romanowicz, Chair
Professor Douglas Dreger
Professor Imke de Pater

2001

The dissertation of Hrvoje Tkalčić is approved:

Chair **Date**

Date

Date

University of California at Berkeley

2001

Study of deep Earth structure using body waves

by

Hrvoje Tkalčić

to my family and friends

Acknowledgments

Going through numerous acknowledgments and searching for ideas about what should be written in this section, I discovered that 90% of them start with acknowledging their research advisers. My case is not an exception. If I had space for only one paragraph, it would have been completely devoted to acknowledging my advisor Barbara Romanowicz. Her hard work, dedication, intelligence, self-discipline, leadership, and numerous other qualities, sometimes remind me of the characteristics of one of those out-of-space superheroes. If I think that way, it is indeed easier to comprehend all her achievements. Besides countless hours of meetings and discussions, we have probably exchanged about two thousand e-mail messages in the course of five years I have spent at Berkeley. It is difficult to find proper words to say how much I appreciate the time and the effort she put in my success. I also had a chance and pleasure to meet her wonderful family.

I met Doug Dreger while I was a first year graduate student. Through him, I got a chance to participate in an interesting and challenging project on Long Valley Caldera non double-couple earthquakes. Doug is an extremely insightful and polite person, and was very helpful and always available. I hope that both our friendship and collaboration will continue in the future. I still owe him several "shogi" games (after I learn it, of course).

Besides Barbara and Doug, I am particularly grateful to Eric Clévédé, Yuan-Cheng Gung, Ed Garnero, Nicolas Houy, Dave Stegman and Bob Uhrhammer, amazing individuals from whom I've learnt a great deal of what I know today, and without whose enthusiasm, altruism, unconditional willingness to share their knowledge and expertise through very productive dialogs, would be very difficult, if not impossible, to achieve the goal of completing this thesis. I also had a pleasure to interact with great professors and people like Walter Alvarez, Mark Bukowinski, Roland Burgmann, Raymond Jeanloz, Imke de Pater, Mark Richards and Annie Souriau.

As a graduate student, I also had a privilege to work with undergraduates students, and this was a significant part of my teaching experience. Special thanks to Nicolas Houy, Kim Brower, Dipti Vaghela, Lindsey Fratessa and Shawn Lawrence. Some of the results we got together are incorporated in this thesis, while some others will be studied in more details in future.

It has been a memorable experience to interact with numerous scientists and graduate students at the Berkeley Seismo Lab and the department, some of whom became my close friends. Thanks to Adrian Lenardić, Yuan-Cheng Gung, Ed Garnero, Nicolas Houy, Charles Mégnin, Eric Clévédé, Nikola Brozović, Dave Stegman, David Dolenc, Mike Pasyanos, Fred Gueydan, Mike Antolik, Sofia Akber, Sierra Boyd, Kanani Lee, Asya Kaverina, Lisa Hammersley, Fumiko Tajima, Ulrike Kastrup, John Stock, Irene Sanchez, Roula Roumelioti, Carine Sansorney, Roland Gritto, Roland Mundil, John Lynch, Cliff Riebe, Sander Caldwell, Helge Gonnermann, Ludovic Bréger, Akiko To, Kim Knight, Junkee Rhie, Mark Panning, Sebastien Rousset, Wu-Cheng Chi, David Schmidt, Christianne Stidham, Charley Paffenbarger, Bob Nadeau, Rick McKenzie, Lind Gee, Mark Jellinek, Stephen Zatman, Hank Houck, Jospeh Durek, Yann Capdeville, Frederique Rolandone, Doug Neuhauser, Peggy Hellweg, Mark Murray and Geoff Clitheroe.

I must say that one of the greatest things in Berkeley, besides its human diversity and cosmopolitan atmosphere, is the diversity of food that its numerous restaurants offer. I would like to thank to many local restaurants' and cafes' owners and personnel, for feeding me great food all these years. I will avoid listing all of them, as I don't want to forget anyone. Also, special thanks to Charles and Kristine for treating me with some of their favorite meals.

Very special thanks go to Charley Paffenbarger, Doug Neuhauser, Rick McKenzie, Eleanor Blair, Christina Jordan and Bari Burton from Seismo Lab for being a super staff, and making my life and the lives of other graduate students much easier. Also, I would like to express my sincere thanks to Mei Griebenow who helped me a lot regarding various issues throughout my stay at UC Berkeley. I am grateful to John Friday, Bill Karavas and Dave Rapkin, for doing an excellent job in installing and maintaining seismological instruments. Also, I am grateful to Terry Arcuri for helping me to buy and maintain my 1973 Ford Maverick.

Last, but not least, it would be difficult to complete this thesis without the presence of my family and all the people in my life whom I missed and who missed me, but who at the same time showed a great moral support to my endeavor.

Table of Contents

Table of Contents **vi**

List of Figures **vii**

1 Anomalous Moment Tensors **6**
1.1 Abstract 6
1.2 Introduction and motivation 7
1.2.1 Geological setting of Long Valley Caldera 7
1.2.2 History of events 7
1.2.3 Seismic moment tensor and methodology 8
1.3 Results and discussion 9
1.4 Conclusions for LVC earthquakes 13
1.5 Anomalous non-double-couple events in Iceland 14

2 PKP Waves **33**
2.1 PKP waves 33
2.2 Inner core anisotropy 34
2.3 Data and measurements 35
2.4 Forward modeling of the lowermost mantle 36
2.5 Conclusions 38

3 Constraints on D" structure using PKP(AB-DF), PKP(BC-DF) and PcP-P travel time data from broadband records **52**
3.1 Abstract 52
3.2 Introduction 53
3.3 Datasets and data selection 55
3.3.1 PKP(AB-DF) dataset 55
3.3.2 PKP(BC-DF) dataset 58
3.3.3 PcP-P dataset 59
3.4 Corrections for mantle structure 60
3.5 Global Sampling and Parametrization 63
3.6 Discussion of resulting models 65

3.6.1 Fits to the data 68
3.7 Discussion and conclusions 70
3.8 Acknowledgements 71

4 Short scale heterogeneity in the lowermost mantle: insights from PcP-P and ScS-S data 98
4.1 Abstract 98
4.2 Introduction and Motivation 99
4.3 Data 101
4.4 Results 102
4.4.1 Comparison of PcP-P residuals with tomographic models 102
4.4.2 Eastern Asia 102
4.4.3 Central America 104
4.4.4 African plume 105
4.4.5 Eastern edge of Pacific superplume 107
4.5 Conclusions 108
4.6 Acknowledgments 109

Bibliography 122

List of Figures

1.1 Location map showing the Long Valley Caldera, resurgent dome, Inyo-Mono craters chain, and earthquakes we investigated. The deviatoric part of the full moment tensor solutions (each has a significant isotropic component) for EVT1-4 is plotted. The deviatoric moment tensor solutions for REF1 (inset) and EVT5 and EVT6 are compared showing that for these events predominantly double-couple solutions are obtained. The locations of 1980 LVC earthquakes are shown as stars and those with significant non-double-couple (NDC) components are shown as filled stars. The event labeled WC is the 1978 Wheeler Crest earthquake that also had a large non-double-couple component. The Devil's Postpile dilatational strain meter (POPA) is shown by the filled square. The inset shows the relative location of the Berkeley Digital Seismic Network stations used in our analysis to the study area. . . 16

1.2 The deviatoric (a) and full moment tensor (b) inverse results are compared for EVT4. In both cases three-component (transverse, radial and vertical from left to right) displacement data (solid) is compared to synthetic seismograms (dashed). The station azimuth and maximum trace amplitudes are (314^o, 5.16×10^{-4} cm), (290^o, 1.23×10^{-3} cm), (276^o, 1.03×10^{-3} cm), (223^o, 2.05×10^{-3} cm), and (218^o, 6.99×10^{-4} cm) for ORV, CMB, BKS, KCC and PKD, respectively. The strike, rake and dip of the two nodal planes of the best double couple, the scalar seismic moment, the percent double couple (DC), percent compensated linear vector dipole (CLVD), percent isotropic (ISO), the variance of the data to the model, and lower hemisphere projection of the P-wave radiation pattern are provided. 17

1.3 The same as in Figure 1.2 is compared for EVT6 in (a) and (b). The station azimuth and maximum trace amplitude for EVT6 are (315^o, 3.03×10^-4 cm), (294^o, 9.41×10^-4 cm), (279^o, 3.93×10^-4 cm), (245^o, 9.49×10^-4 cm), and (222^o, 3.90×10^-4 cm) for ORV, CMB, BKS, KCC and PKD, respectively. 19

1.4 The deviatoric (a) and full moment tensor (b) inverse results are compared for EVT1. For explanation of the parameters, see the caption of Figure 1.2 20

1.5 The deviatoric (a) and full moment tensor (b) inverse results are compared for EVT2. For explanation of the parameters, see the caption of Figure 1.2 21

1.6 The deviatoric (a) and full moment tensor (b) inverse results are compared for EVT3. For explanation of the parameters, see the caption of Figure 1.2 22

1.7 Jackknife test illustrating the stability of the isotropic component for the three anomalous events (diamonds) compared to that for the double-couple events (squares) as a function of the numbers of stations used in the inversion. The symbols show the mean percent ISO with one standard deviation error bars. The sign of the volumetric component is dilation for EVT1-4 and EVT5-6, and compression for REF1. The orientation of the T-axes for all of the station permutations for EVT4 are quite stable (inset), however several of the single station inversions deviate from the main cluster of T-axes. 23

1.8 Vertical component P-waveforms recorded at the closest station, KCC. The displacement data has been bandpass filtered between 0.10 and 8.0 Hz, and is organized in increasing seismic moment order from bottom to top. The long dashed lines mark the direct arrival, and the short dashed lines show arrivals that are interpreted to be due to earth structure effects. 24

1.9 Dilatational strain observed at Devil's Postpile (POPA; Fig. 1) is compared to cumulative $M > 1.5$ seismicity in the south moat of LVC. Three steps in cumulative seismicity are observed. The step in seismicity on 22 November is seen to correlate well with a compressional strain transient. 25

1.10 Location map showing Iceland, the event we investigated (yellow star) (September 29, 1996, UTC 10:48:25.5), and Iceland Hotspot *PASSCAL* experiment stations used in calculating Green's functions and data processing. The stations used in the inversion are indicated by yellow color. 26

1.11 The deviatoric moment tensor inverse result for Bárdarbunga event. Three-component (transverse, radial and vertical from left to right) displacement data (solid) is compared to synthetic seismograms (dashed). The station azimuth and maximum trace amplitudes are indicated below the records. The strike, rake and dip of the two nodal planes of the best double couple, the scalar seismic moment, the percent double couple (DC), percent compensated linear vector dipole (CLVD), percent isotropic (ISO), the variance of the data to the model, and lower hemisphere projection of the P-wave radiation pattern are provided. 27

1.12 The full moment tensor inverse result for Bárdarbunga event. For the explanation of the parameters, see Figure **??**. 28

1.13 Sensitivity test illustrating the stability of: **(top)** the CLVD (presented by the value of ϵ) and **(bottom)** isotropic components as a function of the number of stations used in the inversions. The symbols show the mean ϵ and percent ISO with one standard deviation error bars. 29

2.1 Cross-section of Earth showing the paths of P, PcP, PKPdf, PKPbc and PKPab body waves. 40

2.2 Theoretical travel-time curves for PKP branches for ak135 reference model 41

2.3 Top: Projections of the raypaths for the Fiji Islands events (yellow stars) recorded at the Geoscope station TAM. Bottom: Seismograms corresponding to the paths shown above. PKP(DF) and PKP(AB) arrivals are indicated by black arrows. Red dashed line corresponds to ak135 model predictions for PKP(DF) arrival times. The hypocenter information and distance to the station are plotted to the left of each seismogram. 42

2.4 Top: Projections of the raypaths for the southern hemisphere events (yellow stars) recorded at the GSN station NRIL. Bottom: Seismograms corresponding to the paths shown above. PKP(DF) and PKP(AB) arrivals are indicated by black arrows. Red dashed line corresponds to ak135 model predictions for PKP(DF) arrival times. The hypocenter information and distance to the station are plotted to the left of each seismogram. 43

2.5 Applying Hilbert transform and changing the polarity of PKPab phase produces a waveform similar to PKPdf. 44

2.6 Overlapping the PKPdf waveform from the original trace and the PKPab waveform from the Hilbert-transformed trace, allows a measurement of the travel time shift between them, with great accuracy. 45

2.7 Earthquakes (stars) and stations (triangles) used to collect PKP(AB-DF) differential travel time measurements. 46

2.8 The dataset of PKP(AB-DF) differential travel time residuals plotted with respect to the angle ξ between the PKP(DF) leg in the inner core and the rotation axis of Earth. Residuals are calculated with respect to the ak135 model [*Kennett et al.*, 1995]. Standard ellipticity corrections were applied. All earthquake locations and origin times are corrected with respect to the relocation catalog of [*Engdahl et al.*, 1998]. 47

2.9 Same as Figure **??**, but the subsets of PKP(AB-DF) data corresponding to specific geographic coverage of their paths are indicated with different symbols. Triangles correspond to the earthquakes from South Sandwich Islands region recorded in Alaska and north Asia. Solid squares correspond to south American earthquakes recorded in Asia. White diamonds correspond to Fiji Island region earthquakes recorded at stations in Africa and Europe. 48

2.10 The subset of PKP(AB-DF) differential travel time residuals corresponding to the paths from Fiji Island region events recorded in Europe, plotted as a function of station azimuth. 49

2.11 Top: PKP path from South Sandwich Islands to NRIL station. Bottom: Cross-section through the Earth, along the profile indicated in the top figure, with [*Mégnin and Romanowicz*, 2000] S velocity model in the background. PKP(AB), PKP(BC) and PKP(DF) rays are shown by black lines. 50

2.12 Observed AB-DF travel time residuals (gray diamonds) for events located in the Fiji Islands region as a function of azimuth from the source (left) and angle ξ with respect to the earth's rotation axis (right). Predicted anomalies (black triangles) are (a)(b) for the tomographic model by [*Grand et al.*, 1997] converted to P using a constant scaling factor 0.55, (c)(d) for inner core anisotropy model by [*Creager*, 1992], and (e)(f) for the MMM model by [*Bréger et al.*, 2000]. 51

3.1 Cross-section of Earth showing the paths of P, PcP, PKPdf, PKPbc and PKPab body waves. 72

3.2 **(a)** The declustered subsets of PKP(AB-DF) differential travel time residuals used in this study. Different symbols, corresponding to data from different analysts are explained in the legend. Residuals are calculated with respect to the ak135 model and plotted with respect to the angle ξ between the PKP(DF) leg in the inner core and the rotation axis of Earth. Standard ellipticity corrections were applied. All earthquake locations and origin times are corrected with respect to the relocation catalog of [*Engdahl et al.*, 1998]. Some specific polar paths are indicated by numbers as follows: 1) Svalbard Sea to SPA; 2) 63N,143W to SPA; 3) 79N,124E to SPA; 4) 67N,173W to SPA; 5) 60N,153W to SPA; 6) mid-Atlantic ridge to Alaska; 7) South Sandwich Islands to COL; 8) South Sandwich Islands to BILL; 9) South Sandwich Islands to SEY; 10) southeast Pacific to NRIL; 11) South Sandwich Islands to COL and NRIL; 12) mid-Atlantic ridge to Alaska; 13) south of New Zealand to FRB; 14) Bouvet Islands to COLA and INK; 15) Aleutian Islands to SYO; 16) Sea of Okhotsk to SYO; 17) south of New Zealand to KBS; 18) various locations to SYO; 19) and 20) Aleutian Islands to SYO. **(b)** Same as (a), where circles and pluses correspond to paths for which PKP(DF) bottoms in the quasi-western and quasi-eastern hemisphere, respectively, as defined by [*Tanaka and Hamaguchi*, 1997]. . . . 73

3.3 **(a)** The declustered subsets of PKP(BC-DF) differential travel time residuals used in this study. Different symbols, corresponding to data from different analysts are explained in the legend. Some specific polar paths are indicated by numbers as follows: 1) Novaya Zemlya to SNA; 2) Alaska to SPA; 3) South Sandwich Islands to MBC; 4) Alaska and north Canada to SPA; 5) South Sandwich Islands to northeast Asia and Alaska; 6) 52S,140E to NOR; 7) Siber to SBA; 8) 53S,160E to NOR; 9) 62N,154E, 64N,125E and 60N,169E to SPA; 10) 60N,153W to SPA; 11) various locations to SYO; 12) south of Australia to NOR. **(b)** Same as (a), where now circles and pluses correspond to paths with PKP(DF) bottoming in the quasi-western and quasi-eastern hemisphere, respectively. 75

3.4 PcP-P travel time residuals plotted at the surface projections of PcP bouncing points. Triangles and circles indicate positive and negative residuals, respectively. The size of the symbol represents the value of the residual, the thickness of symbol lines scales with epicentral distance of the measurement: the thicker the line, the larger the epicentral distance. The largest symbols represent a travel-time anomaly of 2.8 seconds. 77

3.5 **(a)** Variance reduction in PKP(AB-DF) data as a function of scaling coefficient h, as defined in text, for various P models, for the whole mantle (solid lines) and for the whole mantle stripped of D"(dashed lines); **(b)** Same as (a), for the PcP-P dataset. 78

3.6 Average relative velocity variations in the lowermost 300 km of the mantle needed to explain PcP-P residuals, as a function of the length of PcP leg in the same layer. Mantle corrections are taken into account (from [*Kárason and Hilst*, 2001]. 79

3.7 Surface projections of PKP(AB) and PcP legs sampling the lowermost 300 km of the mantle. Diamonds represent penetration points of PKP(DF) into the core (their legs sampling the lowermost 300 km of the mantle would projects as points since they traverse that layer at almost vertical incidence). 80

3.8 The sampling of D" in terms of number of counts per block (number of rays crossing each particular block: **(a)** before the variable-size block algorithm is applied; **(b)** after the variable-size block algorithm is applied. The critical number of counts per block is set to be 3 in this example. White areas represent blocks that have been rejected because of insufficient sampling. Note that in (b), blocks have changed shape and increased their size in areas of poor sampling and remain small in well-sampled areas. 81

3.9 **(a)** The synthetic checker-board input model, parametrized in terms of equiangular cells of size 5x5^o (same as in inversion); **(b)** The corresponding output model, for the optimal damping. White non-gridded areas are non-sampled blocks. 82

3.10 Models **(a)** TRH_KC and **(b)** TRH_KCa, for the optimal damping. These one layered models represent P velocity perturbations with respect to model ak135 in the bottom 300 km of the mantle. TRH_KC was obtained by inverting PKP(AB-DF) and PcP-P data simultaneously, without inner core anisotropy. For TRH_KCa, the same dataset was inverted, but first corrected for the transverse isotropy model of [*Tromp*, 1995]. Blackened areas represent non-sampled regions. 83

3.11 One layer models of P-wave velocity perturbations in the lowermost 300 km of the mantle, obtained from different combinations of data, as described in Table 2: **(a)** TRH_KC; **(b)** TRH_KCeq; **(c)** TRH_KCnsa. The models are here shown in polar projections centered on the south pole (left) and north pole (right). 85

3.12 **(a)** Variance reduction in various PKP(AB-DF) datasets from Table 2 calculated from corresponding models of the lowermost 300 km of the mantle (indicated by different symbols in figure as explained in the legend), plotted as a function of damping parameter. Residuals are corrected for the KH2001m model above the lowermost 300 km of the mantle. Appropriate weighting is applied for the paths with similar geometry in calculating variance reduction, as explained in the text; **(b)** the percentage of blocks with perturbations exceeding ±1% for the same models as in (a). 87

3.13 Variance reduction in the complete PKP(BC-DF) dataset obtained for models TRH_K and TRH_KC (indicated by different symbols in figure), plotted as a function of damping parameter. Residuals are corrected for the KH2001m model above the lowermost 300 km of the mantle. Appropriate weighting is applied for the paths with similar geometry in calculating variance reduction as explained in the text. 88

3.14 Observed versus predicted PKP(AB-DF) residuals, plotted as a function of ξ for: **(a)** TRH_KC; **(b)** TRH_KCeq; **(c)** TRH_KCnsa; **(d)** TRH_KCa; **(e)** The inner core anisotropy model TR95 used in the derivation of TRH_KCa. The predictions include the contribution of KH2001m. In (d), the predictions also include the contribution of TR95 shown in (e). 89

3.15 Observed versus predicted PcP-P residuals for: **(a)** TRH_KC; **(b)** TRH_KCeq; **(c)** TRH_KCnsa. The predictions include the contribution of KH2001m. Variance reduction and correlation coefficients are indicated. Solid line is the best linear fit. 91

3.16 Observed (diamonds) versus predicted (triangles) PKP(BC-DF) residuals as a function of ξ for: **(a)** model TRH_KC combined with KH2001m; **(b)** radial model of inner core anisotropy (TR95); **(c)** model TRH_KCa, combined with KH2001m and TR95. 93

4.1 PcP-P travel time residuals plotted at the surface projections of PcP bouncing points. Residuals are calculated with respect to $ak135$ model, and corrected for ellipticity. Triangles and circles indicate positive and negative residuals, respectively. The background model is: **(a)** S wave velocity model $SAW24B16$ by [*Mégnin and Romanowicz*, 2000]; **(b)** P wave velocity model by [*Obayashi and Fukao*, 1997] 110

4.2 Depth profile of PcP-P anomalies accumulated along the PcP and P paths through S wave model $SAW24B16$ scaled to P model using factor 0.55. The model is divided in 18 layers. The maximum, as well as the median value of PcP-P travel time contributions, are indicated in each layer by large and small circles, respectively. Red and gray symbols indicate travel time contributions calculated for positive and negative anomalies separately. The numbers indicate how many paths of total PcP-P dataset yielded in negative or positive anomalies in each layer. 111

4.3 Results for variance reduction in a subset of PcP-P residuals with PcP reflection points under Eurasia, obtained comparing PcP-P travel time data to S tomographic velocity models, using a two-parameter search for the thickness of the bottom layer and the value of R inside it. Variance reduction is shown as a function of obtained value of R in the bottom layer. Thickness of the lowermost layer is indicated by colors. For the same thickness, multiple curves from top to bottom represent decreasing value of R in the bottom layer from 3 to 1 by a step of 0.4. The S models used are: **(top left)** $SAW24B16$ by [*Mégnin and Romanowicz*, 2000]; **(top right)** $S362D1$ by [*Gu and Dziewonski*, 2001]; **(bottom)** $SB4L18$ by [*Masters et al.*, 1999] . . 112

4.4 Best fitting depth profiles of $R = \partial lnV_s/\partial lnV_p$ obtained by comparing PcP-P travel time data to S tomographic velocity models, using a parameter search for the thickness of the bottom layer and the value of R inside it. Comparison restricted to a subset of PcP-P residuals with PcP reflection points under Eurasia with global S tomographic models $SAW24B16$ (solid line, variance reduction 57%), and models $SB4L18$ and $S362D1$ (thick dashed line, variance reduction 60% and 52%, respectively). The thin dashed line corresponds to the best fitting depth profile of R using the global PcP-P dataset and model $SAW24B16$ (variance reduction 10%). Shaded area represents the uncertainty in the thickness of the lowermost layer for the parametrization used. 113

4.5 PcP-P (yellow symbols) and ScS-S (green symbols) travel time residuals plotted at the surface projections of PcP and ScS bouncing points beneath central America. The size of symbols is scaled in such a way that the largest absolute PcP-P residual corresponds to the largest absolute ScS-S residual. The background model is $SAW24B16$. Orange dashed lines delineate the slow velocity anomaly found in study by [*Wysession et al.*, 2001] 114

4.6 ScS-S residuals (diamonds) and mantle corrections (lines) for 3 S tomographic models from Figure **??**, for a single event recorded at MOMA array in United States [*Wysession et al.*, 2001]. Thick, medium and thin solid lines represent ScS-S, S and ScS mantle corrections, respectively. 115

4.7 **(top)** PcP-P travel time residuals plotted at the surface projections of PcP bouncing points for south Atlantic/south Africa region. The largest triangle and circle correspond to residuals of +3 s and -1.5 s, respectively. The background model is $SAW24B16$. Green crosses are ScS reflection points. The AB line connects South Sandwich Island region with the Tanzania network, and the CD line connects the same region with BGCA station; **(middle)** Cross-section through $SAW24B16$ along profile AB, with P and PcP paths from a South Sandwich Islands region event to SUR, BOSA and LBTB stations and a south Atlantic ridge event to Tanzania network; **(bottom)** Cross-section through $SAW24B16$ along profile CD, with P and PcP paths from a South Sandwich Islands region event to BGCA station. 116

4.8 **(top)** Subset of PcP-P travel time residuals for paths associated with the AB profile from Figure **??**, plotted as a function of PcP bouncing points longitude. The residuals are calculated with respect to $ak135$ model, and corrected for ellipticity; **(bottom)** ScS-S residuals originating from the two events in the south Atlantic: 07/25/94 (-56.343, -27.395) and 04/14/95 (-60.843, -20.023), plotted as a function of PcP bouncing points longitude. The S residuals are calculated with respect to $PREM$ model, and corrected for ellipticity. 118

4.9 **(top)** PcP-P (yellow symbols) and ScS-S (green symbols) travel time residuals plotted at the surface projections of PcP and ScS bouncing points for eastern Pacific region. The largest triangle and circle correspond to residuals of +9 s and -2.2 s, respectively. The background model is $SAW24B16$. The AB line connects the 94/02/12 event with station CMB in California; **(bottom)** Cross-section through $SAW24B16$ along profile AB, with the corresponding PcP and P paths. 119

Abstract

Study of deep Earth's structure using body waves

by
Hrvoje Tkalčić
Doctor of Philosophy in Geophysics
University of California at Berkeley
Professor Barbara Romanowicz, Chair

I present a work in which both source and structure aspects of the observational seismology are studied. In the first chapter of the thesis, we address anomalous behavior of the Long Valley Caldera earthquakes, with moment tensors being dominated by CLVD and volumetric components. We conclude that the the anomalous events may have been triggered by net fault-normal stress reduction due to high-pressure fluid injection or pressurization of fluid saturated faults due to magmatic heating. We currently study non-double-couple earthquakes in Iceland, in order to get better understanding of the physics behind their source processes.

The rest of the thesis is dedicated to studying of the deep mantle structure (and the inner core indirectly) using broadband differential and absolute travel time measurements of mostly P waves that travel through the Earth's core, and those that bounce of the core-mantle boundary. We present three such global datasets of hand-picked high quality measurements: PKP(AB-DF), PKP(BC-DF) and PcP-P, which we hope, will also be helpful in the future studies of the Earth's interior. We confirm by forward modeling and inversion that the lowermost mantle is a very heterogeneous region and that in order to make conclusions about the physical and chemical properties of the Earth's core, these heterogeneities have to be taken into account. Our models of D" are characterized by prominent fast features under mid America and east Asia, a fast belt across Pacific, a slow region under the southwestern Pacific and southern Africa, as well as sharp transitions from fast to slow, for instance under Alaska and south Atlantic. Heterogeneity itself cannot completely explain the trends observed in differential time residuals, when plotted as a function of the angle between P wave paths in the inner core and the Earth's spin axis, but it can account for most of the trend. Inner core anisotropy, with the fast P axis oriented parallel to the Earth's spin axis, which was hypothesized to exist as the main cause of the trends in travel time residuals and inner core sensitive normal modes splitting, thus can not be ruled out. However, anisotropy has to be very complex, which is difficult to reconcile with its plausible physical causes.

We use the core-mantle boundary reflected PcP and ScS seismic waves to investigate the nature of heterogeneities in the lowermost mantle. The PcP-P and ScS-S differential travel time residuals, calculated with respect to 1D Earth reference models, exhibit coherent spatial variations, when the same are projected at the PcP and ScS reflection points. Our observations include good spatial correlation between PcP-P and ScS-S residuals, revealing the existence of short scale heterogeneities previously overlooked by global tomographic models, as well as large discrepancy between the observed PcP-P and ScS-S residuals for some paths bottoming under slow anomalies. All these observations could be explained by the presence of strong chemical heterogeneities at the base of the mantle.

Approved:

Barbara Romanowicz, Chair Date

General introduction

The Earth is a very dynamic planet. Its surface reflects a continual evolution, in a mechanical, thermal and chemical sense. One of the major discoveries of the twentieth century was the recognition that the surface of our planet consists of many "plates" that are in continual motion. However, this discovery could not have been possible had there been no progress made in other fields of human knowledge, like geology, geodesy, geomagnetism, rock mechanics, seismology, astronomy, biology, chemistry, etc. Despite the fact that scientists from various disciplines participate in investigating Earth's interior processes, at the beginning of the twenty first century, our planet's interior still remains not completely understood. Partially, the reason for this lies in a limited tool to probe the Earth. Since the discovery of the major discontinuities inside the Earth in the first half of the twentieth century, seismology continues the leading role in investigation of the Earth's structure, although the progress in our understanding of global processes inside the Earth, could not be possible without developments in other fields such as experimental and theoretical mineral physics, geodynamics, geomagnetism, geochemistry and geodesy. Not less important are technological advances in instrumental seismology, developments in laboratory devices for high temperature and pressure experiments, and revolution in computer science and technology.

A seismological observation is possible due to the fact that elastic waves, upon being generated in the focus of an earthquake, travel through the bulk of the Earth, and are being recorded as seismograms by sensitive instruments - seismographs. A considerable part of seismological research, (and this work itself) is based on measurements of onset times or amplitudes of various seismic phases collected from digital recordings at stations located all around the world. A seismogram is a superposition of a source function, structure properties, and an instrument response. One of the fundamental problems in seismology is how to deconvolve these three components. Assuming that we are familiar with instrument characteristics, very often our knowledge about the Earth's structure is based on how well we understand the source process. Vice versa, without understanding the Earth's structure between source and receiver to a certain degree of precision, it is impossible to infer profound conclusions about the source mechanism itself.

This work has two parts; in the first one we study volcanic earthquakes and try to understand the way they radiate energy from the source. In the second part, by using travel times of seismic waves sensitive to the Earth's core and the lowermost mantle, we investigate lateral heterogeneities and anisotropy in the Earth, and try to identify and separate contributions to travel times coming from the core, from those coming from the mantle. We also address an important question, whether the 3D seismic velocity anomalies, as seen in tomographic models of the mantle, are of a thermal or a compositional nature.

In Chapter 1, in a study of the anomalous behavior of the focal mechanisms of the earthquakes in Long Valley Caldera, California, we encounter some of the above mentioned problems. Using 1D and 3D structural models, and a regional time-domain inversion method using complete waveforms at frequencies between 0.02 and 0.05 Hz, we invert for the focal mechanisms for a recent earthquake swarm (1997), and find that some of the events have a very low percentage of the double-couple components of the moment tensor, and correspondingly high CLVD and isotropic components. We infer that the physical source to explain this behavior could include opening the cracks under high pressure. We also rule out a possibility that the anomalous wave propagation due to complex structure associated with the eastern front of Sierra Nevada has an impact on our results.

The following chapters focus on the study of Earth's structure by using travel time measurements. One region of particular interest with regard to this work is the core-mantle boundary (CMB) region. It is a dynamic region which controls the transfer of heat, material, and angular momentum between the core and the mantle. By its diversity and contrasts in various parameters, it is comparable with Earth's surface. The D" layer comprises the lowermost 250-300 km of the mantle, and it is known from various seismological studies, that this layer is very heterogeneous in material properties on a variety of length scales. One of the most important questions that seismology has been addressing, is what is the nature of these heterogeneities; purely thermal variations, compositional variations due to possible chemical reactions, the existence of partial melt, or a combination of all mentioned features.

The second region of particular interest is the Earth's core. Being separated from the mantle by large contrasts in density, viscosity and other parameters, Earth's core has an important role in the dynamic processes, since it prevents convective motion to be continuous throughout the Earth's interior. The convective motions within the outer core itself, are one of the basic ingredients of Earth's magnetic field. In addition, the inner core interacts with Earth's magnetic field in such a way, that probably stabilizes it against more frequent reversals. Various seismological observations in the last fifteen years of the twentieth century, led to the two very interesting interpretations regarding the inner core: 1) that the inner core is anisotropic with fast compressional velocities on paths parallel to the spin axis and 2) that the inner core exhibits a super-rotation with respect to the rest of the planet.

In Chapter 2, as an introduction to Chapter 3, we describe the data and the methodology used. We recognize regular trends of PKP(AB-DF) differential travel time residuals, when plotted as a function of different parameters with respect to their geographical origin. It had been previously known that PKP(AB) legs are affected on their way through D" region. By assigning PKP(AB-DF) residuals to the structure in D" region, we challenge the traditional interpretation that the trend in PKP(AB-DF) residuals when plotted as a function of the angle between PKP(DF) leg in the inner core and Earth's spin axis (this angle is hereafter called ξ), comes purely from inner core anisotropy. We demonstrate that most of the trend in the residuals can be explained using an *ad hoc* P velocity model of the D" region, derived from an S model, boosted up only in its negative anomalies (modified mantle model, hereafter called MMM). However, there are some residuals, for the most anomalous polar paths, that remain unexplained, even after a correction for MMM model. In addition, PKP(BC-DF) residuals, which exhibit the same trend when plotted as a function of the angle ξ, could not be explained by MMM, as it doesn't contain enough lateral variations, although there are some areas near the CMB on the mantle side, which could account for rapid variations in PKP(BC-DF) residuals.

Following the work presented in Chapter 2, in Chapter 3 we inverted combined PKP(AB-DF) and PcP-P datasets to obtain the P velocity structure in the lowermost 300 km of the mantle. It is of a great interest to accurately estimate the effects of complex structure in the deep mantle and D" on PKP differential travel times, in order to assess how much of the data can be explained by mantle structure alone. We compare models obtained with and without polar PKP paths and find that their inclusion or exclusion does not significantly affect the resulting D" model. Our preferred model, obtained using PKP(AB-DF) and PcP-P data combined, explains about 90% of the variance in PKP(AB-DF), almost 60% of the variance in PcP-P and 27% of the variance in PKP(BC-DF), a significant portion considering that the PKP(BC-DF) dataset was not used in the inversion. The anomalous South Sandwich region to Alaska data cannot fully be explained by D" structure alone, unless very short wavelength lateral variations are introduced. Models that allow for a modest level of constant transverse anisotropy in the inner core, (compatible with normal mode splitting data) combined with the structure in D", perform somewhat better, but still fail to explain 2 sec in PKP(BC-DF) residuals.

In Chapter 4, using core reflected PcP and ScS waves in combination with P and S waves, respectively, we document the existence of compositional variations in D". We examine the behavior of compressional and shear velocity perturbations in the mantle through the logarithmic ratio $R = \partial lnV_s/\partial lnV_p$, at the local and regional scales. We compute variance reduction in PcP-P subsets by tracing the rays through several recent S, scaled to P tomographic models using a given ratio R, on the one hand, and directly comparing

PcP-P and ScS-S residuals on the other. The spatial distribution of anomalies of our PcP-P dataset when plotted at the bouncing PcP points, indicate that in some regions of the lowermost mantle, global mantle tomographic models don't have enough resolution to explain trends and fine variations in PcP-P and ScS-S travel time data.

Chapter 1

Anomalous Moment Tensors

This chapter is a modified version of a paper published in *Science*, [*Dreger et al.*, 2000], and also presented is a work in progress [*Tkalčić et al.*, 2002].

1.1 Abstract

Regional distance seismic moment tensor determinations and broadband waveforms of moment magnitude 4.6-4.9 earthquakes from a November 1997 Long Valley Caldera swarm, during an inflation episode, display evidence of anomalous seismic radiation characterized by non-double-couple (NDC) moment tensors with significant volumetric components. Observed coseismic dilation suggests that hydrothermal or magmatic processes are directly triggering some of the seismicity in the region. Similarity in the NDC solutions implies a common source process, and the anomalous events may have been triggered by net fault-normal stress reduction due to high-pressure fluid injection or pressurization of fluid saturated faults due to magmatic heating.

Using the same methodology, we investigate September 29, 1996 anomalous volcanic event originated beneath Bárdarbunga caldera in Iceland. The corresponding non-double-couple moment tensor is characterized by a significant CLVD component. Preliminary sensitivity tests show that isotropic component in moment tensor is not significant.

1.2 Introduction and motivation

1.2.1 Geological setting of Long Valley Caldera

The Long Valley Caldera (LVC) is located along the east side of the Sierra Nevada in the region of east-central California (Figure 1.1). It's part of a large and active volcanic system that also includes Mono-Inyo Craters volcanic chain. Volcanic activity in the area began about 3.6 Ma with basaltic and andesitic lava flows, followed by rhyodacite, erupted as flows and domes while magma chamber was growing underneath. LVC is tectonically and volcanically active. The Long Valley volcanic system, which erupted about 760 000 years ago, was responsible for the deposition of the Bishop Tuff and formation of a broad oval depression of Long Valley Caldera (15km by 32 km). This system, along with the younger fissure system of the Mono-Inyo Craters volcanic chain are the two magmatic systems operating in the region. Some of the most recent eruptions took place along the Inyo Craters volcanic chain and on Paoha Island in Mono Lake about 600 and 250 years ago, respectively.

1.2.2 History of events

A period of ongoing geologic unrest began in 1978 and culminated in mid May 1980 when four magnitude 6 events occured in a two day period. This earthquake swarm was accompanied by a ground deformation, an inflation of a resurgent dome ([*Hill et al.*, 1985], Figure 1.1), in the center of the caldera. As a result of this activity the US Geological Survey initiated extensive seismic, ground deformation and chemical monitoring in 1982. These surveys have revealed episodic seismicity swarms that correlate with the inflation of the resurgent dome, but confirmation of direct fluid involvement in the seismicity has been elusive. In May, 1980 four magnitude 6 earthquakes occurred. Two south of the LVC in the vicinity of the Hilton Creek fault, and two in the south moat of the caldera (Figure 1.1). The latest episode of LVC deformation began in 1997, and first became apparent in 2-color laser geodimeter data as increased inflation of the resurgent dome in June followed by earthquake swarm activity in the south moat in July. Deformation rates and swarm activity continued to increase through October to rates exceeding 2 cm/month and

100 $M > 1.2$ earthquakes per day. Swarm activity, strain and tilt rates increased on 22 November, 1997, with the onset of a series of $M > 4.0$ earthquakes. A borehole strain meter recorded a transient signal over the following week. Dome inflation, deformation and swarm activity returned to background rates in early 1998 (e.g. [*Langbein et al.*, 1998; *Hill*, 1998]).

1.2.3 Seismic moment tensor and methodology

Most earthquakes are caused by shear faulting. A shear fault is equivalent to a pair of couples which have torques that cancel each other (double-couple or DC). However, there are earthquakes which have source processes other than shear-faulting (non-double-couple or NDC), and their physical causes are not very well understood. A mathematical method for describing earthquake mechanisms is provided by the seismic moment tensor, M_{ij}, a generalized source representation that encompasses double-couple forces, more general types of shear forces and volumetric forces. M_{ij} is commonly decomposed into double couple, compensated-linear-vector-dipole (CLVD) and isotropic components (ISO) (e.g. [*Knopoff and Randall*, 1970; *Jost and Hermann*, 1989]), where each of the components of the moment tensor decomposition is represented as a percentage of the total. The CLVD consists of a major vector dipole with twice the strength and opposite sign to two orthogonal, minor vector dipoles, and can describe the separation or compression of a fault with no net volume change. The isotropic component has three orthogonal vector dipoles of equal magnitude, and resolves volumetric changes. NDC seismic moment tensors have been observed in a variety of tectonic and volcanic environments. Several mechanisms such as multi-planar rupture [*Wallace*, 1985; *Kuge and Lay*, 1994], non-planar rupture [*Frohlich*, 1994], and tensile failure [*Julian and Sipkin*, 1985] have been proposed to explain observed NDC moment tensors. In principle it should be possible to determine the isotropic components given body and surface wave data, however they are difficult to resolve [*Kawakatsu*, 1996; *Dufumier and Rivera*, 1997], and there have been only a few studies that have reported significant volumetric components [*Zheng et al.*, 1995; *Campus et al.*, 1996; *Hara et al.*, 1996; *Miller et al.*, 1998].

The seismic moment tensor, can be determined by the linear inversion of observed seismic ground motions using appropriately calibrated Green's functions. The method used inverts complete, three-component, long-period displacement seismograms for the 6 independent elements of the symmetric seismic moment tensor. Both data and synthetic seismograms are filtered using 8-pole butterworth causal filters. A synchronous and impulsive source time function, and spatial point-source are assumed. A linear inversion for moment tensor amplitudes is then possible. The event source depth is determined iteratively by performing independent inversions for depths of 5, 8, 11, 14 and 17 km. The percent CLVD is calculated from the minimum and maximum eigenvalues defined by ($|\lambda_3| > |\lambda_2| > |\lambda_1|$), where $\epsilon = |\lambda_1/\lambda_3|$, and $PCLVD = 200\epsilon$ and $PDC = 100 - 200\epsilon$. The percent isotropic (ISO) is the ratio of the isotropic moment to the sum of the isotropic and deviatoric moments. The DC consists of two vector dipoles of equal magnitude but opposite sign, resolving shear motion on faults oriented 450 to the principle eigenvectors of M_{ij}.

At least two of four magnitude 6 events from the 1980 swarm, one located at the caldera margin and the other 12 km to the south, as well as an earlier event in 1978, were found to have significant non-double-couple (NDC) seismic moment tensors (e.g. [*Given et al.*, 1982; *Ekstrom and Dziewonski*, 1983; *Julian*, 1983; *Barker and Langston*, 1983; *Wallace et al.*, 1982]).

1.3 Results and discussion

The recent 1997 swarm, between November 1997 and January 1998, has included over 1000 events of magnitude 2, about 100 events of magnitude 3 and 9 events in magnitude range 4. Routine analysis of seismic moment tensors by the Berkeley Seismological Laboratory revealed that a number of events in the November 1997 swarm displayed unusual seismic radiation patterns [*USGS Volcano Hazards Program*, 1997]. Seven events (Table 1.1) have been reanalyzed using our method, which inverts three-component, complete seismograms (including regional P and S body waves and Love and Rayleigh surface waves), recorded at the five closest Berkeley Digital Seismic Network (BDSN) stations (Figure 1.1), for the complete seismic moment tensor. We have constructed two catalogs of moment tensor solutions for these earthquakes. The first is a catalog of solutions constrained to have no volume change (DC and CLVD only, i.e. deviatoric moment tensor), while the second catalog is comprised of unrestrained solutions (DC, CLVD and isotropic components, i.e. full moment tensor (FMT)). As an example of the inverse procedure we compare the deviatoric and full moment tensor solutions for EVT4 (Figure 1.2 (a, b)). We typically find that CLVD components are $\leq 30\%$ for earthquakes in Northern California. Four events, EVT1-4, were found to have anomalous NDC moment tensors including large dilatational volumetric components, and three, EVT5-6 and REF1, resulted in nearly pure DC solutions (Table 1.2). The deviatoric inversion (Figure 1.2 (a)) yielded an anomalous solution with a 67% CLVD component, and the FMT solution (Figure 1.2 (b)) shows a large 42% isotropic moment, the sign of which indicates volumetric expansion. Also shown are deviatoric and full moment tensor solutions for EVT1, EVT2 and EVT3 in Figures 1.4, 1.5, and 1.6, respectively. In contrast, the deviatoric inversion for EVT6 yielded a nearly pure DC solution and the FMT inversion yielded a large DC component (Table 1.2, Figure 1.3 (a, b)). Tests of inversion sensitivity, forward modeling of the data, examination of Poisson ratio sensitivity, and 3-CLVD decompositions of deviatoric inversion results indicate that there is no tradeoff between a vertical-CLVD and the isotropic component that we report. To estimate the significance of the deviatoric and FMT solutions we evaluated the improvement in fit to the data using the F-test (Table 1.2). It is always possible to fit the data better with models with a greater number of unknowns. The F-test is used to determine whether a model with a change in the number of free parameters fits the data significantly better than what might be expected from random fluctuations in the data [*Menke*, 1989]. There are 5 unknowns in the DC inversions (depth, scalar seismic moment, strike, rake and dip), 6 in the deviatoric moment tensor inversion and 7 in the full moment tensor inversion. To perform the test the variance, σ^2, of the data is estimated from the model prediction error, $e_i = (data_i - synthetic_i)$, where $\sigma^2 = \sum e_i^2/(N - M)$ and N and M are the number of observations and model parameters respectively. The F statistic is the ratio of the two data variance estimates. Critical values of F above which the difference in the variance is significant can be calculated from the F distribution. For the calculations in this report, considering a 20s correlation length for the data the critical values of F are 1.36 (95% confidence) and 1.55 (99% confidence). A grid search algorithm was used to determine the best pure DC solution for each event. The FMT solutions of the anomalous events (EVT1-4) satisfy the F-test for significance above the 95% level relative to a reference DC solution. The F-test using the deviatoric solution as reference indicates $> 90\%$ significance for EVT1 and $> 95\%$ significance for EVT2-4. The FMT solution for these four events resulted in isotropic moments that are a considerable fraction of the deviatoric moment, and the improvement in fit is statistically significant whether the DC or the deviatoric NDC solution is used as a reference (Table 1.2). The maximum eigenvalue for all of the inversions is extensional and the corresponding eigenvectors are nearly horizontal and oriented to the SW. This orientation is consistent with regional strain and the inflation of the resurgent dome that is observed in the LVC [*Hill et al.*, 1985]. Deviatoric inversions for EVT5 and EVT6 resulted in large DC components and the FMT inversions resulted in isotropic components of 12% or less and large DC components. The F-tests for EVT5-6 indicate that the reduction in variance is not statistically significant above 95%, and in fact, it is only significant at the 65% level at best. REF1 located outside of the LVC is another event with a small, statistically insignificant, isotropic component.

For additional insight into the significance of the results we tested the stability of the solutions using subsets of the data to explore the possibility that a given station or combination of stations may be controlling the inversion. In our Jackknife test we performed inversions using all combinations of one, two, three, four and five stations for the LVC events (Figure 1.7), and find a clear separation between the anomalous events that satisfied the F-test and the reference events that did not. The reference events with small isotropic components ($\approx 10\%$) indicate that it is not possible to resolve isotropic components of 10% or less. The mean value of the isotropic percentage for EVT1-4 lies between $27 - 45\%$, and is found to be stable for all of the station-subsets. The stability of one- and two-station inversions indicates that azimuthally dependent path effects are not a factor in the inversion results of the anomalous events. The stability of the four-station inversions reveals that the isotropic component is not due to the dominance of any one station.

Broadband P-waveforms also show anomalous behavior (Figure 1.8). REF2 and REF3 are small events that have similar P-waveforms, and first-motion focal mechanisms, indicating that the observed P-wave complexity is most likely due to path effects. While it is possible that the complex P-waveform of these events is due to an identical source process, this is unlikely and the first P pulse is interpreted as direct P and the two that follow are likely reflected arrivals or mode conversions. Given the definitions of scalar seismic moment,

$M_0 = \mu AD$, and static stress drop, $\Delta\sigma = c\mu D/L$, where μ is the material rigidity at the source, A (equal to L^2) is the source area and D is the average slip, L is the source dimension and c is a geometrical constant approximately equal to 1, the following relationship for L is found: $L \approx (M_0/\Delta\sigma)^{1/3}$. The source duration, τ, is then found to approximately equal $(M_0/\Delta\sigma)^{1/3}/\beta$, where β is the seismic shear wave velocity. Assuming this constant stress drop scaling law and a value of 3 MPa, a source duration of 0.2 s is obtained for REF3 and 0.06 s for REF2. The observed duration of the direct P pulse is the same for the two events suggesting that seismic wave attenuation may be broadening the pulses. EVT6 resulted in a nearly pure DC solution that is similar to the first motion solutions of REF2 and REF3, and also seen to have a similar P waveform. The estimated source duration of 0.46 s, for a stress drop of 3 MPa, is consistent with the observed duration of 0.5 s, indicating that for the larger events the duration of the P-waves is a good representation of the source process time.

The P-waveforms of EVT1, EVT2 and EVT4 have unusually long duration. There is a 2.0 to 2.5 s source phase with superimposed shorter-period arrivals. Estimated static stress drops using these long source durations are $\ll 0.1$ MPa, and are outside the $1 - 10$ MPa range observed in most earthquakes [*Kanamori and Anderson*, 1975]. For example, assuming a stress drop of 3 MPa, a duration of 0.58 s is obtained, which is less than a third of the observed duration. EVT3 is an anomalous moment tensor event that has an emergent onset to the P-waveform, but does not have the long-period source component observed in the other three events.

The isotropic moment was used to estimate the change in source volume (ΔV) through the equation, $M_{0iso} = [\lambda + (2/3)\mu]\Delta V$ [*Aki and Richards*, 1980], where M_{0iso} is the scalar seismic moment of the isotropic component, and λ and μ are the Lame and rigidity elasticity constants. Assuming that $\lambda = \mu = 3 \times 10^{10}$ Pa, the estimated ΛV (Table 1.2) are much less than the 0.02 to 0.04 km^3/yr that can be attributed to the inflation of the resurgent dome [*USGS Volcano Hazards Program*, 1997]. For a spherical geometry the radii of the volume increase are 28, 39, 25 and 43 m for EVT1-4. Assuming a static stress drop of 3 Mpa, the fault dimension, L, of each event was determined from the deviatoric seismic moment, and the fault separation, $U_N = \Delta V/L^2$, was estimated (Table 1.2). U_N is of order 5 to 10 cm, which is consistent with observed openings of exhumed magmatic dikes, however it is noted that U_N is inversely proportional to L^2, and therefore subject to uncertainty. For example, a stress drop of 0.1 MPa results in separations of between 0.5 to 1.0 cm. An anomalous compressional volume strain transient was observed during this sequence on the POPA dilatational strain meter located 11 to 13 km to the west of the study events (Figure 1.1). This exponential-like strain event (Figure 1.9) apparently initiated with EVT1 at 12:06 UTC on 22 November and decayed with a 2.3 day time constant.

Coseismic extensional strain steps of -3.5, -6.3 and -19 nanostrain were observed with events EVT1, EVT2, and EVT3, respectively. EVT4 on 30 November produced a coseismic compressional strain step of 37 nanostrain with no additional transient nature. Coseismic strain offsets usually agree with calculations based on moment release by earthquakes [*Johnston et al.*, 1987]. Coseismic offsets for all events are about a factor of two or greater than offsets calculated for POPA assuming simple double-couple dislocations. These independent data support the contention that significant volume change occurred with these later earthquakes. Inclusion of the volume components inferred above into the offset calculation, reduces the discrepancy but still underestimates the observed offsets. This suggests that additional volumetric moment release occurred outside the pass band of the seismometers.

It has been suggested that NDC moment tensors for the 1980 events could be due to tensile failure due to injection of high-pressure fluid [*Julian and Sipkin*, 1985], simultaneous fault slip of two differently oriented DC sources [*Wallace*, 1985], and bias due to unaccounted for near-source crustal structure [*Wallace*, 1985]. None of these studies allowed for an isotropic component, and it is not known if the 1980 and 1997 events are similar in this regard; however, they are quite similar in terms of the NDC deviatoric moment tensor solutions.

1.4 Conclusions for LVC earthquakes

The observation of significant volumetric expansion components in the moment tensors of 1997 LVC seismicity indicates a direct relationship between at least some of the seismicity and hydrothermal or magmatic processes. Magma intrusion rapid enough to cause the May 1980 events cannot be ruled out [*Julian and Sipkin*, 1985], however the source process times of the 1997 events, although unusually long, are too short to be explained by the injection of low viscosity magma. The isotropic components may be due to the injection of high-pressure fluids or pressurization of a fluid saturated fault by heat from a nearby magmatic body. A northeast dipping dike from just north of the south moat of the caldera is one possible model that can explain the transient dilatational strain anomaly of 22 November, 1997 [*Langbein et al.*, 1998; *Hill*, 1998]. The modeled dike fails to bisect the faults in the south moat and a direct interaction seems unlikely, although it is possible that a network of fractures may allow effective fluid and heat transport. Right-lateral shear on an east striking fault coupled with a minor inflation source can also explain the strain data [*Langbein et al.*, 1998; *Hill*, 1998], and a possible scenario for the recent LVC activity is the evolution of the system from a locked fault, to stick-slip motion, to stable-sliding as fault pore pressure increases.

In addition, in a related study [*Panning et al.*, 2001], we demonstrated that near-source structure does not appear to falsely produce significant isotropic components of moment tensor inversions.

1.5 Anomalous non-double-couple events in Iceland

The highly non-double-couple nature of the focal mechanisms of several events beneath Bárdarbunga volcano in Iceland previously reported in the Harvard centroid moment tensor (CMT) catalog, was confirmed by analysis of long-period and intermediate surface wave data (e.g. [*Nettles and Ekstrom*, 1998]). From the inversion of P wave data, the same authors interpreted the source mechanisms as faulting on an outward dipping cone-shaped ring fault beneath the caldera. In a current study, we apply the same methodology described in the section about the Long Valley Caldera earthquakes, to determine how significant are the volumetric components in the moment tensors of these earthquakes.

We start with using the September 29, 1996 event of $M_w = 5.6$ and Iceland Hotspot experiment stations (Figure 1.10), with an intention of investigating several more smaller earthquakes from the same area in the future.

The most demanding task was calculation of Green's functions for Iceland area. By using a frequency wave-number integration (FKI) code, we produced a set of Green's functions using: a) an S waves crustal tomography model (*R. Allen, written communication*), b) crustal models determined by combining teleseismic receiver functions and surface wave dispersion curves [*Du and Foulger*, 2001].

We compare the deviatoric and full moment tensor solutions for September 29, 1996 Bárdarbunga event in Figures 1.11 and 1.12, respectively. The deviatoric inversion yielded an anomalous solution with a 67% CLVD component, while the FMT solution shows a similar, 66% CLVD component, accompanied with an insignificant volumetric contraction ($ISO = 2\%$).

We performed a sensitivity test, in which we examine the stability of CLVD (presented by the value of ϵ) (Figure 1.13 (top)) and isotropic components (Figure 1.13 (bottom)) as a function of the number of stations used in the inversion. As can be seen, as the number of stations increases, CLVD component becomes very stable, reaching a value of about 0.35. On the other hand, isotropic component percentage decreases with increasing number of stations. Despite the fact that in a recent paper [*Dreger and Woods*, 2001] illustrated that it is possible to identify the anomalous radiation of explosive events with as few as three stations, Figure 1.13 emphasizes the importance of a good azimuthal coverage in the inversions. Clearly, one station is insufficient to recover the percentage of CLVD component, and three stations can still yield a relatively high level of isotropic component. Future work will involve analyzing smaller events in the same area. If the same focal mechanism, with large CLVD components is obtained, this will challenge the hypothesis of faulting on a dipping cone-shaped ring fault [*Nettles and Ekstrom*, 1998], as it is highly unlikely that an order of magnitude smaller earthquake is capable to produce enough energy for failure on a cone fault below the magma chamber floor.

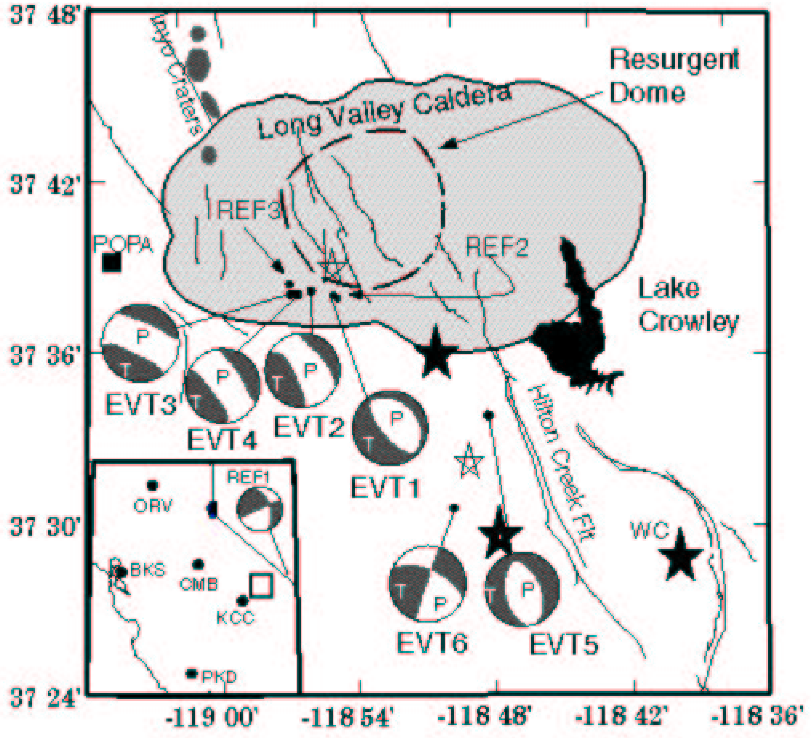

Figure 1.1. Location map showing the Long Valley Caldera, resurgent dome, Inyo-Mono craters chain, and earthquakes we investigated. The deviatoric part of the full moment tensor solutions (each has a significant isotropic component) for EVT1-4 is plotted. The deviatoric moment tensor solutions for REF1 (inset) and EVT5 and EVT6 are compared showing that for these events predominantly double-couple solutions are obtained. The locations of 1980 LVC earthquakes are shown as stars and those with significant non-double-couple (NDC) components are shown as filled stars. The event labeled WC is the 1978 Wheeler Crest earthquake that also had a large non-double-couple component. The Devil's Postpile dilatational strain meter (POPA) is shown by the filled square. The inset shows the relative location of the Berkeley Digital Seismic Network stations used in our analysis to the study area.

Figure 1.2. The deviatoric (a) and full moment tensor (b) inverse results are compared for EVT4. In both cases three-component (transverse, radial and vertical from left to right) displacement data (solid) is compared to synthetic seismograms (dashed). The station azimuth and maximum trace amplitudes are (314^o, 5.16×10^{-4} cm), (290^o, 1.23×10^{-3} cm), (276^o, 1.03×10^{-3} cm), (223^o, 2.05×10^{-3} cm), and (218^o, 6.99×10^{-4} cm) for ORV, CMB, BKS, KCC and PKD, respectively. The strike, rake and dip of the two nodal planes of the best double couple, the scalar seismic moment, the percent double couple (DC), percent compensated linear vector dipole (CLVD), percent isotropic (ISO), the variance of the data to the model, and lower hemisphere projection of the P-wave radiation pattern are provided.

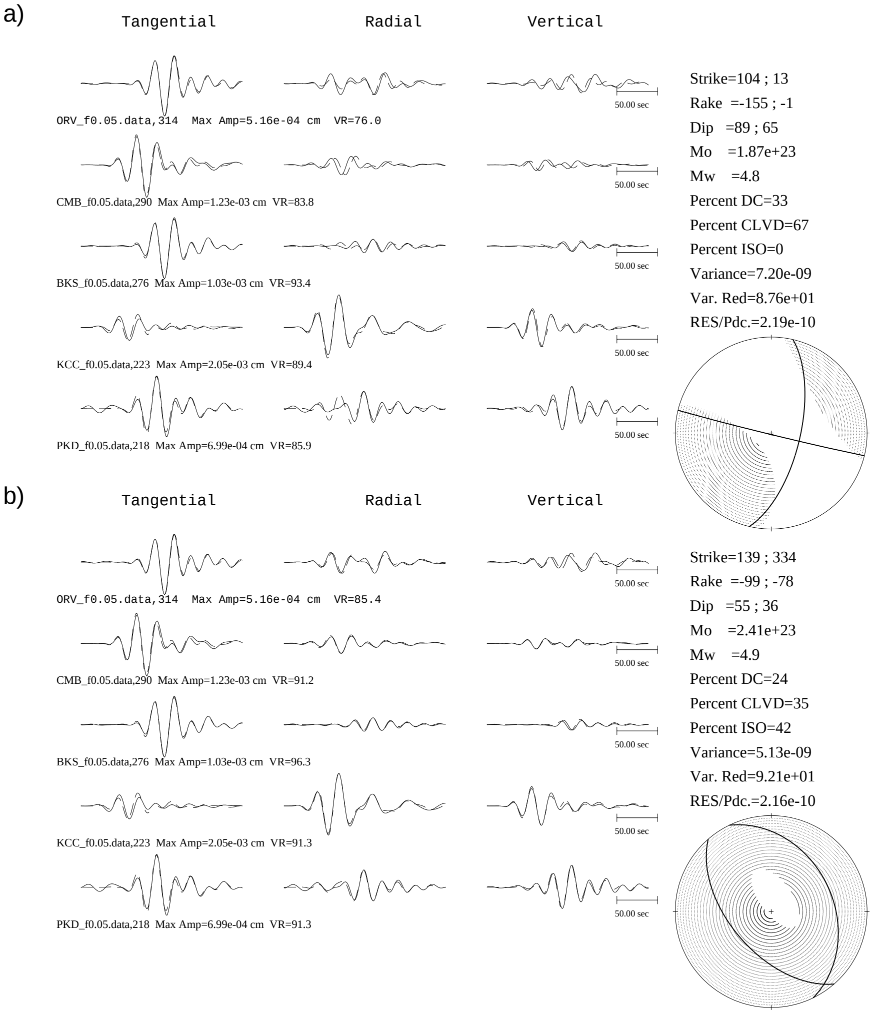
a)
Tangential
Radial
Vertical
ORV_f0.05.data,314 Max Amp=5.16e-04 cm VR=76.0
CMB_f0.05.data,290 Max Amp=1.23e-03 cm VR=83.8
BKS_f0.05.data,276 Max Amp=1.03e-03 cm VR=93.4
KCC_f0.05.data,223 Max Amp=2.05e-03 cm VR=89.4
PKD_f0.05.data,218 Max Amp=6.99e-04 cm VR=85.9
50.00 sec
Strike=104 ; 13
Rake =-155 ; -1
Dip =89 ; 65
Mo =1.87e+23
Mw =4.8
Percent DC=33
Percent CLVD=67
Percent ISO=0
Variance=7.20e-09
Var. Red=8.76e+01
RES/Pdc.=2.19e-10
b)
Tangential
Radial
Vertical
ORV_f0.05.data,314 Max Amp=5.16e-04 cm VR=85.4
CMB_f0.05.data,290 Max Amp=1.23e-03 cm VR=91.2
BKS_f0.05.data,276 Max Amp=1.03e-03 cm VR=96.3
KCC_f0.05.data,223 Max Amp=2.05e-03 cm VR=91.3
PKD_f0.05.data,218 Max Amp=6.99e-04 cm VR=91.3
50.00 sec
Strike=139 ; 334
Rake =-99 ; -78
Dip =55 ; 36
Mo =2.41e+23
Mw =4.9
Percent DC=24
Percent CLVD=35
Percent ISO=42
Variance=5.13e-09
Var. Red=9.21e+01
RES/Pdc.=2.16e-10

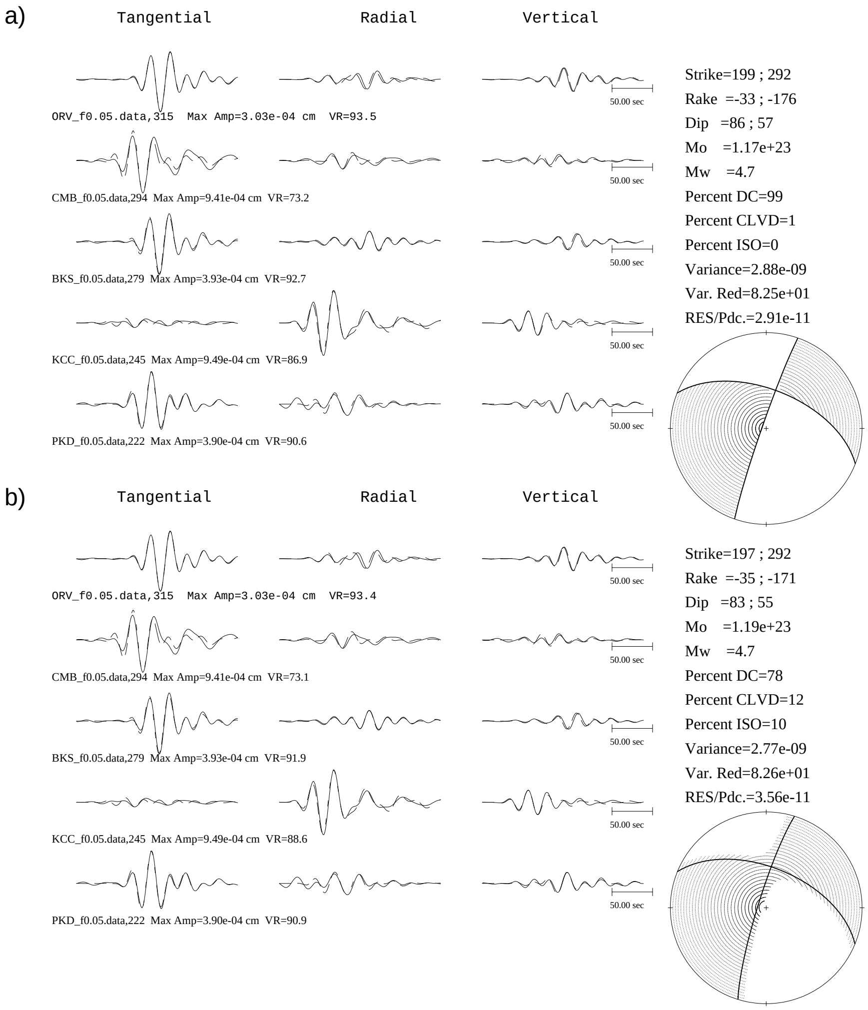

Figure 1.3. The same as in Figure 1.2 is compared for EVT6 in (a) and (b). The station azimuth and maximum trace amplitude for EVT6 are (315^o, 3.03×10^-4 cm), (294^o, 9.41×10^-4 cm), (279^o, 3.93×10^-4 cm), (245^o, 9.49×10^-4 cm), and (222^o, 3.90×10^-4 cm) for ORV, CMB, BKS, KCC and PKD, respectively.

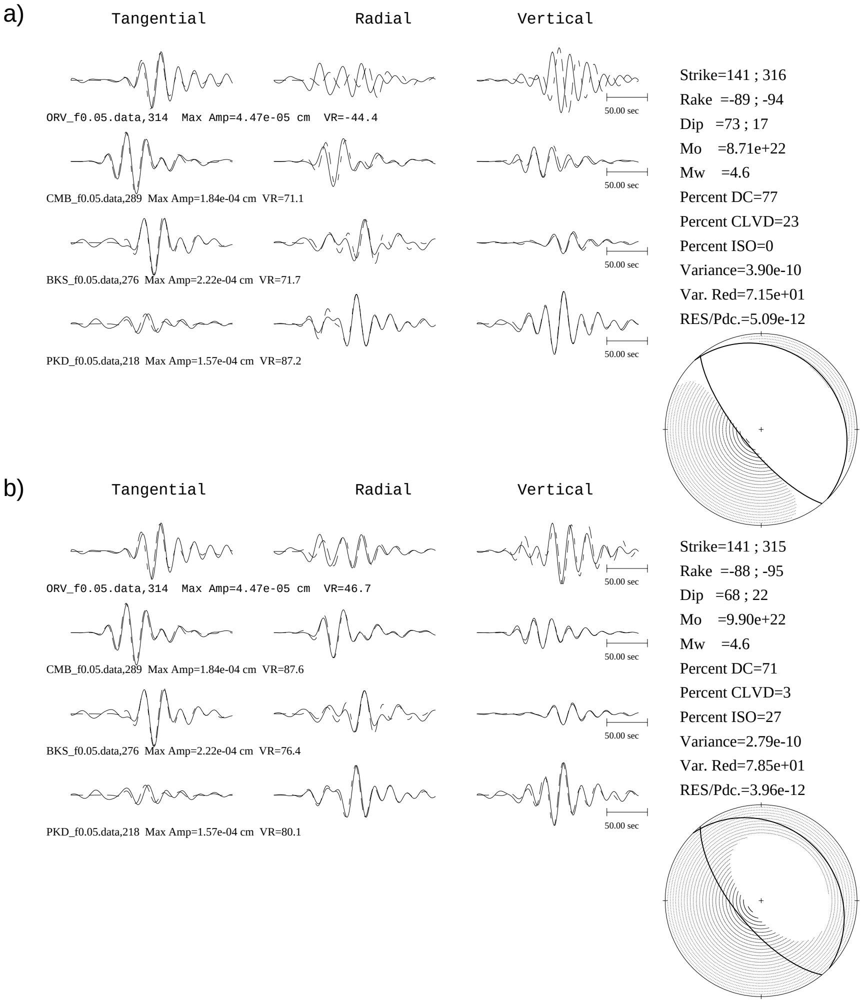

Figure 1.4. The deviatoric (a) and full moment tensor (b) inverse results are compared for EVT1. For explanation of the parameters, see the caption of Figure 1.2

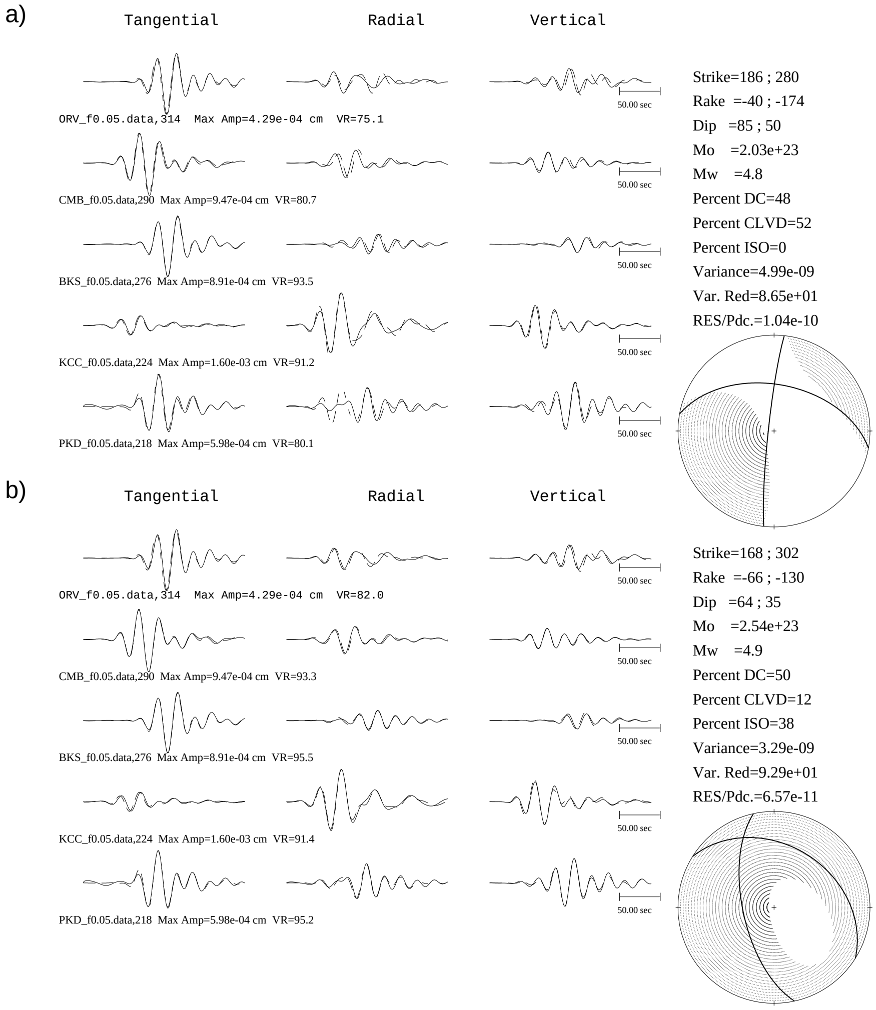

Figure 1.5. The deviatoric (a) and full moment tensor (b) inverse results are compared for EVT2. For explanation of the parameters, see the caption of Figure 1.2

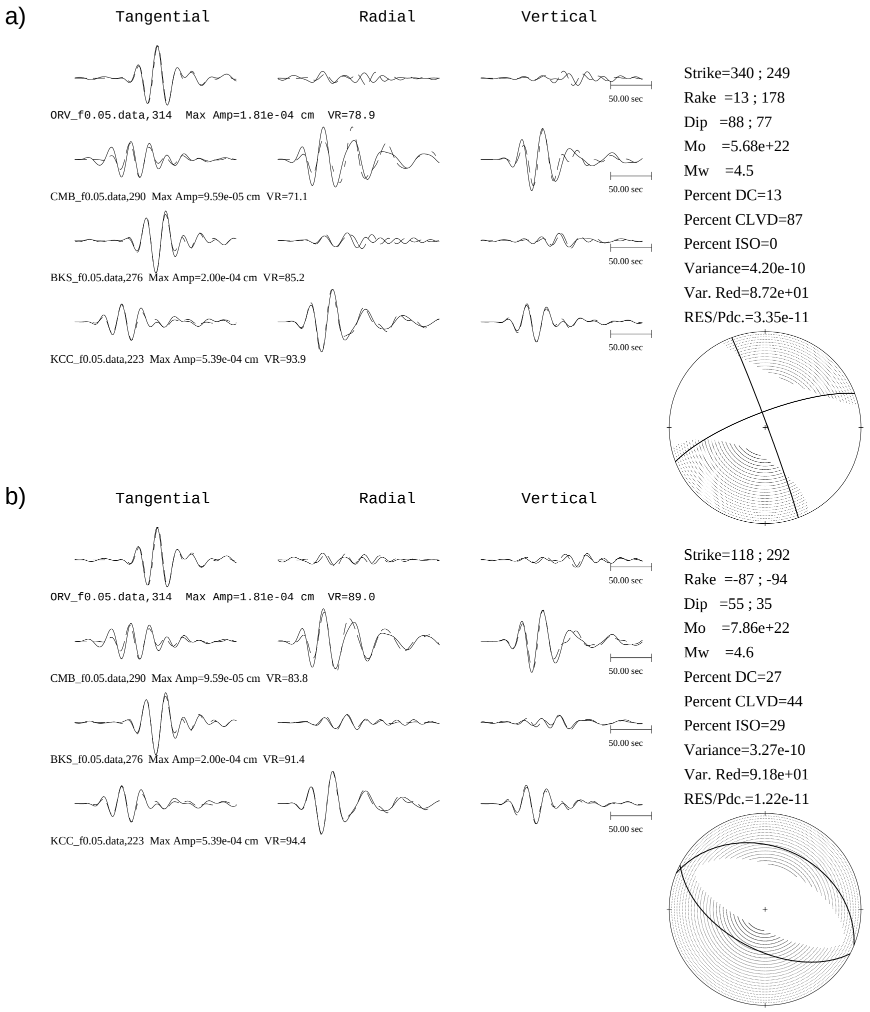

Figure 1.6. The deviatoric (a) and full moment tensor (b) inverse results are compared for EVT3. For explanation of the parameters, see the caption of Figure 1.2

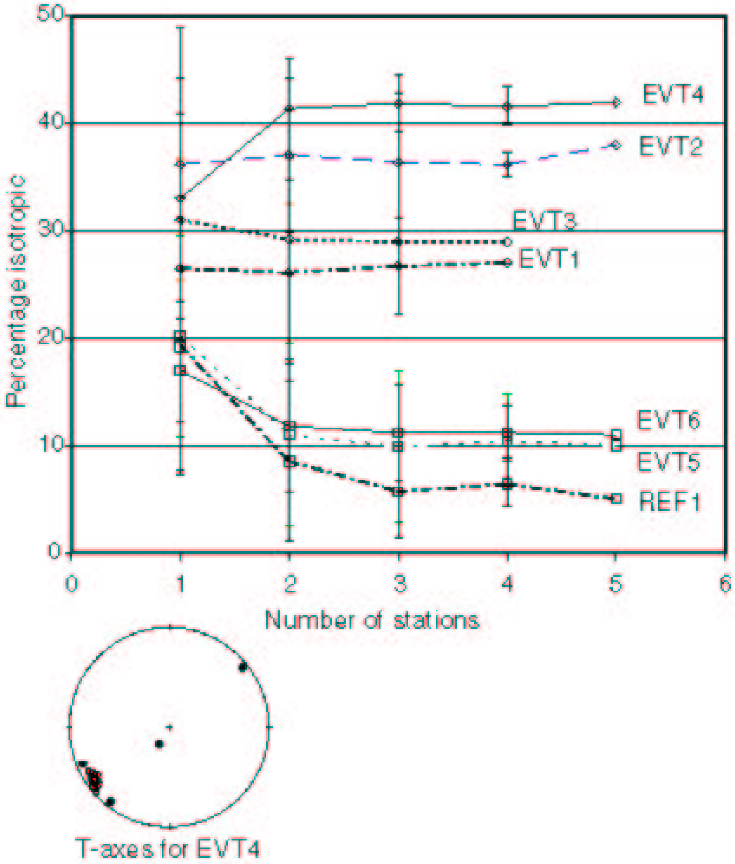

Figure 1.7. Jackknife test illustrating the stability of the isotropic component for the three anomalous events (diamonds) compared to that for the double-couple events (squares) as a function of the numbers of stations used in the inversion. The symbols show the mean percent ISO with one standard deviation error bars. The sign of the volumetric component is dilation for EVT1-4 and EVT5-6, and compression for REF1. The orientation of the T-axes for all of the station permutations for EVT4 are quite stable (inset), however several of the single station inversions deviate from the main cluster of T-axes.

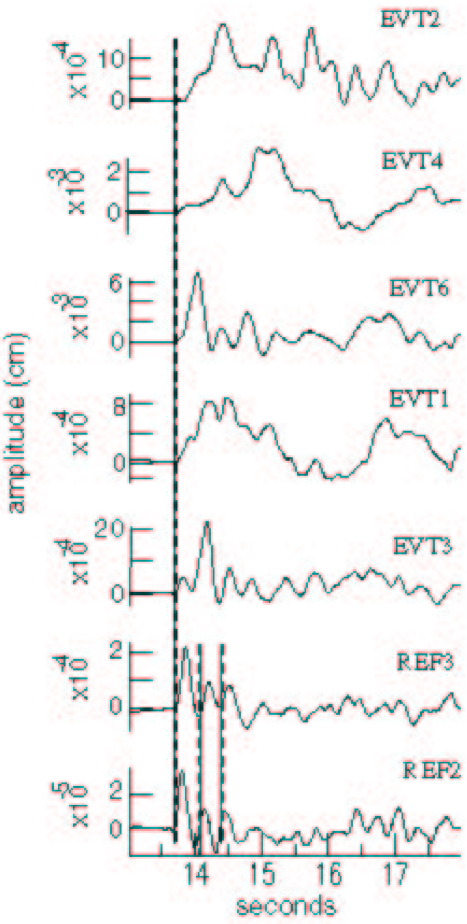

Figure 1.8. Vertical component P-waveforms recorded at the closest station, KCC. The displacement data has been bandpass filtered between 0.10 and 8.0 Hz, and is organized in increasing seismic moment order from bottom to top. The long dashed lines mark the direct arrival, and the short dashed lines show arrivals that are interpreted to be due to earth structure effects.

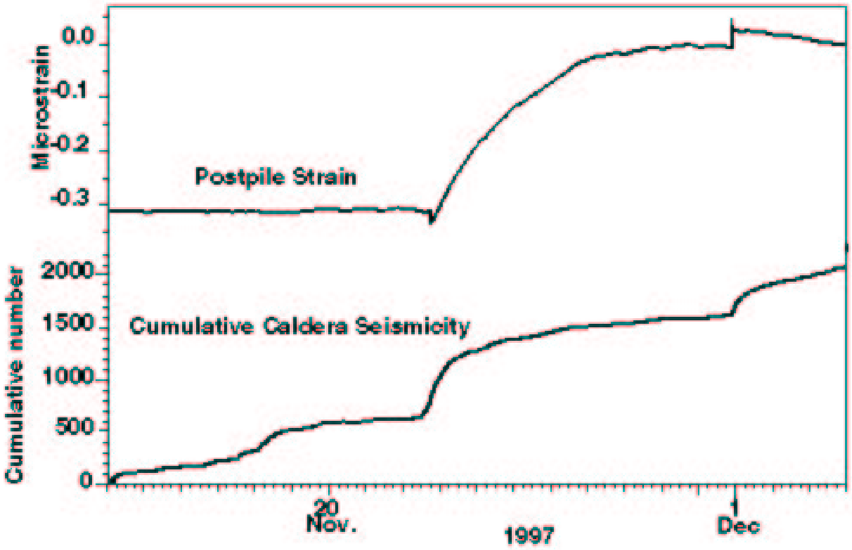

Figure 1.9. Dilatational strain observed at Devil's Postpile (POPA; Fig. 1) is compared to cumulative $M > 1.5$ seismicity in the south moat of LVC. Three steps in cumulative seismicity are observed. The step in seismicity on 22 November is seen to correlate well with a compressional strain transient.

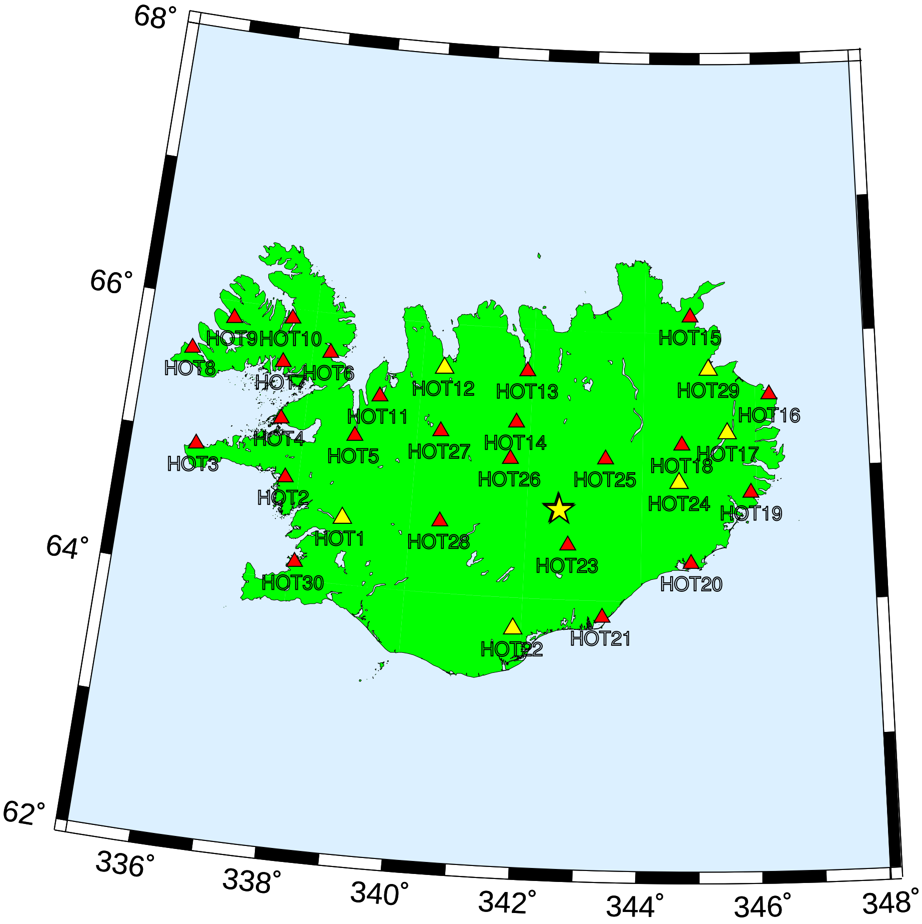

Figure 1.10. Location map showing Iceland, the event we investigated (yellow star) (September 29, 1996, UTC 10:48:25.5), and Iceland Hotspot *PASSCAL* experiment stations used in calculating Green's functions and data processing. The stations used in the inversion are indicated by yellow color.

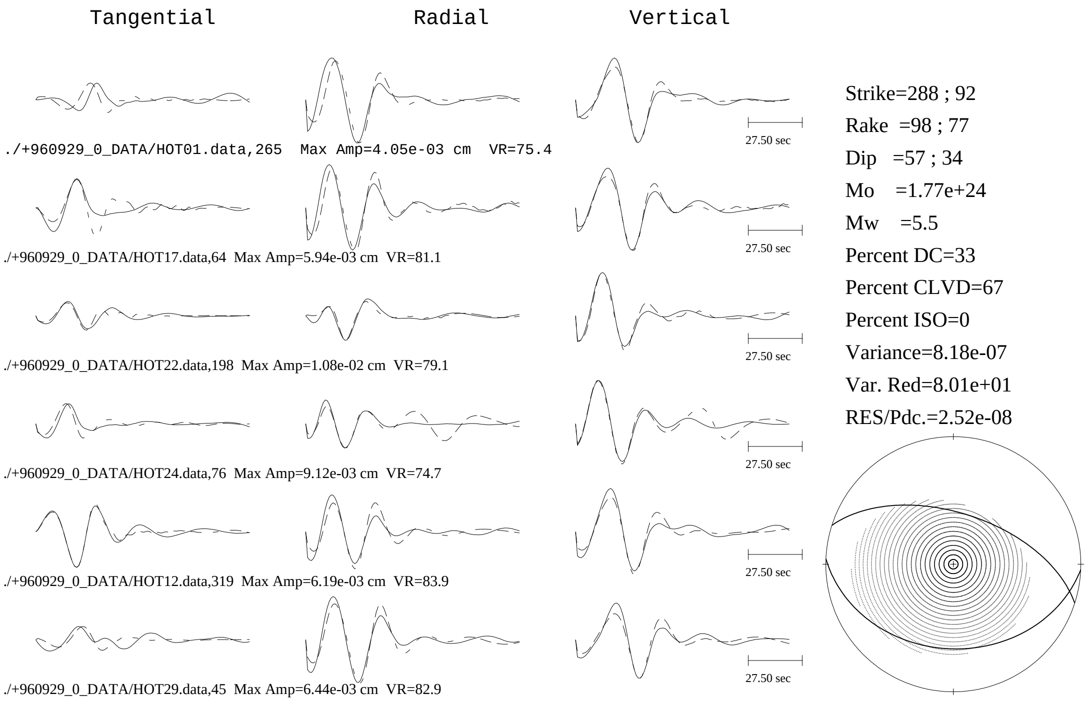

Figure 1.11. The deviatoric moment tensor inverse result for Bárdarbunga event. Three-component (transverse, radial and vertical from left to right) displacement data (solid) is compared to synthetic seismograms (dashed). The station azimuth and maximum trace amplitudes are indicated below the records. The strike, rake and dip of the two nodal planes of the best double couple, the scalar seismic moment, the percent double couple (DC), percent compensated linear vector dipole (CLVD), percent isotropic (ISO), the variance of the data to the model, and lower hemisphere projection of the P-wave radiation pattern are provided.

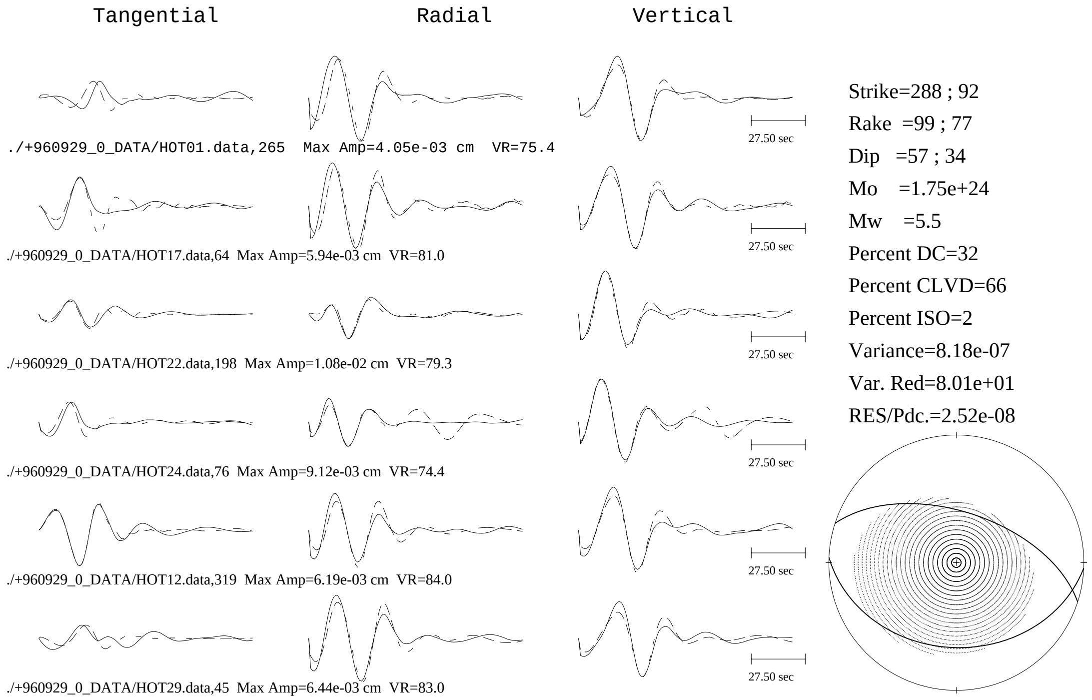

Figure 1.12. The full moment tensor inverse result for Bárdarbunga event. For the explanation of the parameters, see Figure 1.11.

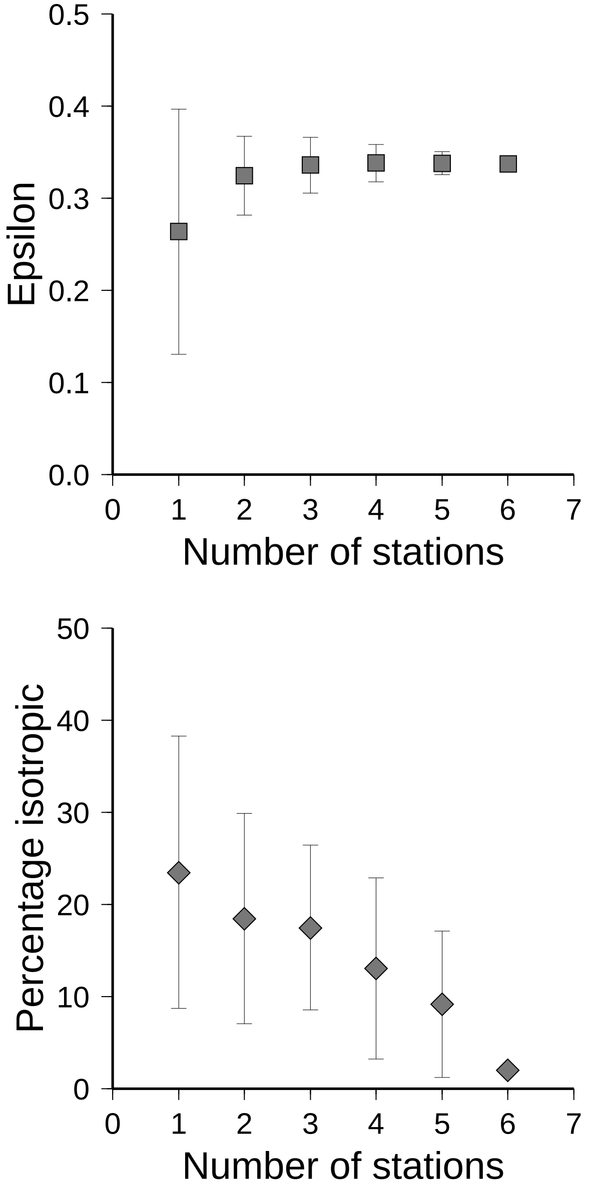

Figure 1.13. Sensitivity test illustrating the stability of: **(top)** the CLVD (presented by the value of ϵ) and **(bottom)** isotropic components as a function of the number of stations used in the inversions. The symbols show the mean ϵ and percent ISO with one standard deviation error bars.

Event ID	Date (dd/mm/yy)	Origin time (UTC)	Latitude (deg. N)	Longitude (deg. W)	Depth (CNSS)	Depth (MT inversion)	Magnitude
REF1	02/11/1997	08:51:53.9	37.846	-118.215	6.4	8	5.3
EVT1	22/11/1997	12:06:56.0	37.635	-118.917	8.4	8	4.6
REF2	22/11/1997	16:09:08.7	37.632	-118.916	8.0	-	2.9
EVT2	22/11/1997	17:20:35.1	37.636	-118.936	7.7	5	4.9
EVT3	22/11/1997	18:10:59.4	37.634	-118.951	8.2	8	4.6
REF3	23/11/1997	02:19:50.4	37.640	-118.952	7.4	-	3.7
EVT4	30/11/1997	21:17:05.4	37.634	-118.946	7.1	5	4.9
EVT5	15/07/1998	04:53:19.3	37.564	-118.806	6.2	5	5.0
EVT6	15/05/1999	17:54:08.8	37.509	-118.831	7.3	8	4.7

Table 1.1. Earthquake data reported in the Council of the National Seismic System (CNSS) catalog. All magnitudes are moment magnitudes except those for REF2 and REF3 events.

Table 1.2. Comparing the deviatoric and full moment tensor inversion results. The percentages of DC, CLVD an ISO (6) to the left are for the deviatoric inversions and to the right for the full moment tensor inversions. The deviatoric M_0 for the full moment tensor inversion is given. $F_{NDC} = \sigma^2_{DC}/\sigma^2_{NDC}$, $F_{Full} = \sigma^2_{DC}/\sigma^2_{Full}$, $F = \sigma^2_{NDC}/\sigma^2_{Full}$ are the F statistics comparing the double-couple to deviatoric, the double-couple to full, and deviatoric to full moment tensor solutions, respectively. Maximum critical values of F to exceed are 1.24, 1.36 and 1.55 for confidence levels of 90%, 95%, and 99% respectively.

Event ID	DC (%)	CLVD (%)	ISO (%)	Deviatoric Mo (10e16 Nm)	F(NDC)	F(Full)	F	ΔV(km^3)	L(km)	Un (cm)
REF1	100/93	0/2	0/5	9.88	-	1.00	-	-	-	-
EVT1	77/71	23/3	0/27	0.90	1.42	1.96	1.31	7.2 x 10e-05	1.48	3.3
EVT2	59/34	41/32	0/33	2.49	1.22	2.06	1.70	2.4 x 10e-04	1.59	9.5
EVT3	13/27	87/44	0/29	0.78	2.35	3.59	1.53	6.4 x 10e-05	1.02	6.1
EVT4	33/24	67/35	0/42	2.41	1.48	2.33	1.57	3.4 x 10e-04	1.79	10.6
EVT5	98/80	2/9	0/11	3.11	-	1.01		-	-	-
EVT6	99/78	1/12	0/10	1.19	-	1.07		-	-	-

Chapter 2

PKP Waves

2.1 PKP waves

In the last several decades, there have been a large number of studies of the inner and the outer core using travel times of core sensitive seismic waves. Compressional seismic waves passing through the Earth's core, that are extensively used throughout this study, are called PKP waves, mainly for historical reasons. Their ray paths consist of three legs (that can be seen in Figure 2.1), two of which are in the mantle (one on the source and one on the receiver side), and are labeled P as the first letter of the word *"primary"*, since compressional waves propagate through the Earth faster and arrive at stations on the Earth's surface earlier than S (*shear or secondary*) waves. The middle leg of PKP is positioned inside the core and is labeled by letter K, which comes from the first letter of the German word for core (*"kern"*).

Figure 2.1 shows a cross-section through the Earth, with its major layers, discontinuities, D" layer, and PKP paths. The dashed line above the core mantle boundary delineates the thickness of D", which is taken to be 300 km hereafter in this work, even though existence and depth of a discontinuity that separates D" from the rest of the mantle is not found from seismology to be a global feature, like major upper mantle dicontinuities.

As can be seen from Figure 2.1, there are three types of PKP waves that traverse the core. PKP(DF) or PKIKP waves traversing the inner core, PKP(BC) waves bottoming in the lowermost part of the outer core, and PKP(AB) waves bottoming in the middle section of the outer core. PKP(DF) and PKP(BC) waves stay much closer to each other throughout the mantle and the core, while PKP(AB) waves remain close to them only in the source and the receiver regions. Furthermore, while PKP(DF) and PKP(BC) steeply penetrate through D" layer, PKP(AB) waves graze through it, which turns out to be very important in the context of this study.

Figure 2.2 shows PKP traveltime curves, estimated from ak135, a spherically symmetric model of the Earth [*Kennett et al.*, 1995], assuming that the depth of the earthquakes is zero. It can be seen from the same figure that PKP(DF) waves are observed from 110^o to 180^o epicentral distance. PKP(BC) and PKP(AB) branches are limited to epicentral distance ranges starting at about 143^o, and ending at about 157^o and 180^o, respectively, although their diffracted portions along inner core and core mantle boundary can be seen even at larger epicentral distances. PKP(CD) (also called PKiKP) branch corresponds to reflections from the inner core boundary, and is not used in this study.

2.2 Inner core anisotropy

The inner core-sensitive free oscillations of the Earth are split much more than expected from the Earth's rotation, inhomogeneity and ellipticity [*Masters and Gilbert*, 1981]. In addition, it was observed that PKP(DF) waves traversing the inner core along trajectories nearly parallel to the Earth's spin axis, arrive at the surface several seconds sooner than waves traveling in nearly equatorial planes [*Poupinet et al.*, 1983]. An example of seismograms corresponding to the equatorial and the polar PKP(DF) paths is shown in Figures 2.3 and 2.4, respectively. Figure 2.3 shows the seismograms corresponding to Tonga-Fiji region earthquakes with equatorial PKP(DF) legs through the inner core, recorded at the Geoscope station TAM in Algeria. The vertical dashed line corresponds to PKP(DF) traveltime predictions from ak135 model. Clearly, there is nothing unusual with the way the PKP(DF) travel time observations match with predictions. To emphasize an opposite situation, in which PKP(DF) observed arrivals exhibit a mismatch with respect to ak135 predictions, in Figure 2.4, we plot the southern hemisphere earthquakes recorded at GSN station NRIL in Russia. These paths are quasi-parallel to the spin axis of the Earth, and as it can be seen, PKP(DF) waves arrive 5 or more seconds earlier than predicted by ak135 model.

Early explanations for both PKP(DF) travel times and normal modes observations, included a model of a prolate inner core with an ellipticity of 200 km [*Poupinet et al.*, 1983], and a model of an aspherical seismic-velocity structure in the outer core [*Ritzwoller et al.*, 1986], both of which were physically difficult to sustain. The concept of inner-core anisotropy (in addition to the general isotropic heterogeneity) as an explanation for both travel-time and normal-mode observations was first proposed by [*Morelli et al.*, 1986] and [*Woodhouse et al.*, 1986]. The inner core is thought to consist of iron in its hexagonal closely packed phase, which has compressional wave-speed anisotropy; i.e. a dependency of wave-speed on the direction of propagation. Two mechanisms for aligning the iron crystals with fast P axes parallel to the spin axis of the Earth early proposed, were convection of the inner core (e.g. [*Jeanloz and Wenk*, 1988; *Weber and Machetel*, 1992; *Romanowicz et al.*, 1996]), and preferred alignment of anisotropic crystals as the inner core freezes (e.g. [*Karato*, 1993a]).

2.3 Data and measurements

Absolute PKP travel time measurements, as mentioned above, led to the observations of anomalous early arrivals of polar PKP(DF) waves. However, using differential travel time data, like PKP(AB-DF), reduces biases of mislocation in space and time, as well as unwanted effects caused by source and receiver structure, due to proximity of paths of the two rays in the crust and the upper mantle (e.g. [*Cormier and Choy*, 1986; *Creager*, 1992]) (Figure 2.1). Any of these unwanted effects should have similar influence on both rays, and thus can be significantly reduced.

Our PKP(AB-DF) dataset comprises differential travel times measured on vertical component seismograms primarily from broadband digital stations, complemented by about 20 measurements from short-period records. Our dataset represents an augmented version of the one considered in [*Bréger et al.*, 2000] and referred to in [*Garnero*, 2000]. Measurements are done by hand, by applying standard techniques, such as Hilbert transform (Figure 2.5) followed by cross-correlation or interactive overlapping of PKP(DF) and PKP(AB) phases (Figure 2.6) in order to measure the precise time-shift between these two arrivals. In our experience, the best data come from large ($Mb > 6$) deep focus earthquakes. However, we were able to make use of many shallow events with good signal to noise ratio, for which we were able to distinguish PKP(DF) and PKP(AB) phases from depth phases such as pPKP(DF), sPKP(DF), pPKP(BC) etc. This involved identifying depth phases and comparing waveforms from several stations for the same event. We tried to process raw data without filtering whenever possible, and only in several instances, we bandpass-filtered the broadband waveforms between 0.5 and 2.0 Hz, using a 4-pole butterworth acausal filter. Some very large events (Mw > 7.0) were omitted in this analysis due to their complex source time function. The uncertainty in measurements is on the order of 0.1 to 0.2 seconds in most cases. However, difficulties in measurement sometimes arise when the shape of the Hilbert-transformed PKP(AB) phase does not match that of PKP(DF) very well, or when the first cycle of the PKP(DF) waveform is unusually broad, which is probably associated with high attenuation in the inner core (e.g. [*Souriau and Romanowicz*, 1996]). In such cases, uncertainty in measurements is about 0.5 seconds or larger, and such data were rejected following our low tolerance approach.

In Figure 2.7, we plot the map of earthquake and station locations used to construct PKP(AB-DF) dataset in this study. As it can be seen, most earthquakes are associated with plate boundaries, and the stations used are most densely distributed across the continents, leaving a large gap in coverage under the oceans.

We computed travel time residuals with respect to the standard ak135 model accounting for Earth's ellipticity *(Kennett and Engdahl*, written communication), and after relocation according to [*Engdahl et al.*, 1998]. The travel time residuals considered are displayed in Figure 2.8 as a function of the angle with respect to the Earth's rotation axis (ξ). Figure 2.8 shows that for the angles less than about 35^o, residuals are shifted toward higher values on average, although a large scatter at $\xi \approx 30^o$ is evident. The majority of the most anomalous data correspond to the measurements obtained from the short period Alaskan network for the earthquakes originating from South Sandwich Islands region and mid Atlantic ridge, as well as measurements recorded at station COL in Alaska and stations SEY, NRIL and BILL in northeast Asia. More details about this and other PKP(AB-DF) datasets used, are given in the following chapter.

2.4 Forward modeling of the lowermost mantle

If inner core anisotropy affects PKP(DF) waves in such a way that the travel times associated to quasi-polar paths are advanced, then positive differential travel time residuals for those paths are expected, as seen in Figure 2.8. These variations are generally interpreted in terms of simple models of anisotropy in the inner core. However, there exist quasi-polar paths that are not anomalous. This is partially explained by a model, according to which, only one, quasi-western hemisphere of the inner core is anisotropic [*Tanaka and Hamaguchi*, 1997], as shown in Chapter 3. However, there are paths sampling the quasi-western hemisphere of the inner core, such as those recorded at SPA station, that are not anomalous. In addition, the scatter present in residuals associated with quasi-equatorial paths is quite large, and it cannot be explained with simple models of constant anisotropy in the inner core (e.g. [*Creager*, 1992; *Tromp*, 1995]).

Furthermore, distinct trends associated with subsets of PKP(AB-DF) data according to their geographical sampling, are observed when plotted with respect to the angle ξ. This is shown in Figure 2.9. Triangles correspond to paths from South Sandwich Island region to Alaska and northeast Asia. The residuals associated with these paths exhibit a large increase for angles ξ between $\approx 40^o$ and $\approx 20^o$. Similar, but smaller in amplitude increase of residuals is seen for the paths from South America to southeast Asia, between $\approx 70^o$ and $\approx 50^o$ (solid squares in Figure 2.9). This trend cannot be predicted by a simple constant model of inner core anisotropy, and it would require much more complex model of anisotropy in the inner core, for instance, an anisotropy with a more inclined fast velocity axis, with respect to the Earth's spin axis. The third distinct trend is observed in residuals for Tonga-Fiji Island events recorded at stations in Europe and Africa. This is shown by white diamonds in Figure 2.9. A V-shaped trend is observed between $\approx 80^o$ and $\approx 45^o$. In addition, from Figure 2.10, it is clear that PKP(AB-DF) residuals associated with Tonga-Fiji Island events recorded in Europe, can be fit by a linearly decreasing trend with respect to azimuth of stations.

On their way through the Earth's interior, PKP waves can be significantly affected by the influence of various length-scale heterogeneities in the mantle. In particular, PKP(AB) legs spend more time in D" than PKP(DF), and can accumulate more advances or delays in their travel times, by interacting with 3D structure. To illustrate this, a cross-section through the Earth, along with the profile from South Sandwich Islands to NRIL station, is shown in Figure 2.11, using $SAW24B16$ model [*Mégnin and Romanowicz*, 2000] in the background. While PKP(DF) on the source side misses the African plume, a significant portion of PKP(AB) path passes through it. As a consequence, the observed differential PKP(AB-DF) travel times along these paths are more positive than predicted from reference models, resulting in larger residuals.

Using a forward modeling approach, we showed that realistic modifications to existing lowermost mantle tomographic models could successfully explain most of the trends in the observed PKP(AB-DF) travel time data, including variations with angle of the PKP(DF) ray-paths in the inner core [*Bréger et al.*, 2000]. In particular, in the [*Grand et al.*, 1997] model scaled to a P model using a constant scaling factor 0.55, we increased the amplitude of all negative anomalies in the lowermost 400 km of the mantle that were exceeding -0.3%, to the value of -2%. Using such a model, called MMM (modified mantle model), we explained much of the variance in PKP(AB-DF) travel time residuals. Our results for the Tonga-Fiji Islands events subset for which PKP(AB-DF) residuals exhibit a distinct V-shaped trend when plotted with respect to the angle ξ (as shown in Figure 2.8), are summarized in Figure 2.12. Residuals plotted as a function of azimuth and angle ξ by diamonds, are shown on the left and on the right side of Figure 2.12, respectively. By 1D ray tracing of the paths from our PKP(AB-DF) dataset through [*Grand et al.*, 1997] model, we calculate contributions from lateral heterogeneities and plot them by triangles in Figure 2.12 (a, b). As can be seen, they don't match observed the residuals in neither the trend nor amplitude. In Figure 2.12 (c, d), we also show predictions from the constant inner core anisotropy model by [*Creager*, 1992]. It is not surprising that such a model does not predict observed variations in residuals, as the inner core anisotropy effect becomes significant only for smaller angles ξ. Finally, the predictions for MMM are shown by triangles in Figure 2.12 (e, f), and clearly, they match the PKP(AB-DF) residuals much better.

2.5 Conclusions

The inner core anisotropy was proposed 15 years ago, to explain two classes of seismological observations: anomalously split inner-core sensitive free oscillations, and advanced arrivals of PKP(DF) paths that traverse the inner core nearly parallel to Earth's spin axis.

However, we observed distinct trends in PKP(AB-DF) residuals when the latter are plotted as a function of angle ξ, by distinguishing between several different geographical samplings of the corresponding paths in the mantle.

We showed that most of the trend observed in PKP(AB-DF) residuals, stem from heterogeneities in the lowermost mantle. In particular, our forward modeling of PKP(AB-DF) travel time residuals, suggest that they are significantly affected by the strong heterogeneity present in the deep mantle beneath Africa and Pacific.

The most anomalous PKP(AB-DF) residuals, mainly associated with the paths from South Sandwich Islands region to Alaska and north Asia, remain unexplained, even after modifications introduced through MMM model.

The effects of complex structure in the deep mantle and D" on PKP differential travel times should be accurately estimated in order to reach reliable conclusions about the physical and chemical properties of the Earth's inner and outer core.

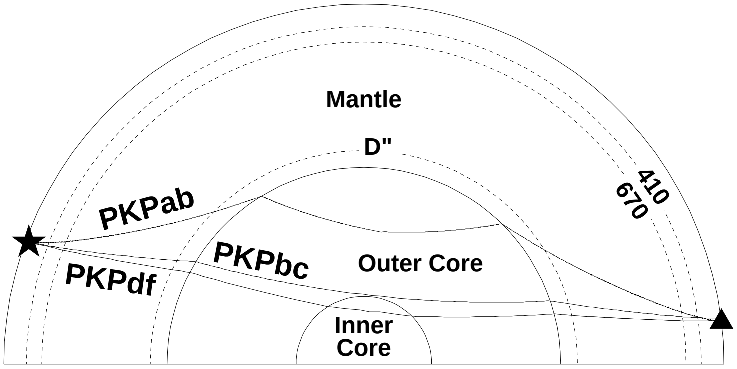

Figure 2.1. Cross-section of Earth showing the paths of P, PcP, PKPdf, PKPbc and PKPab body waves.

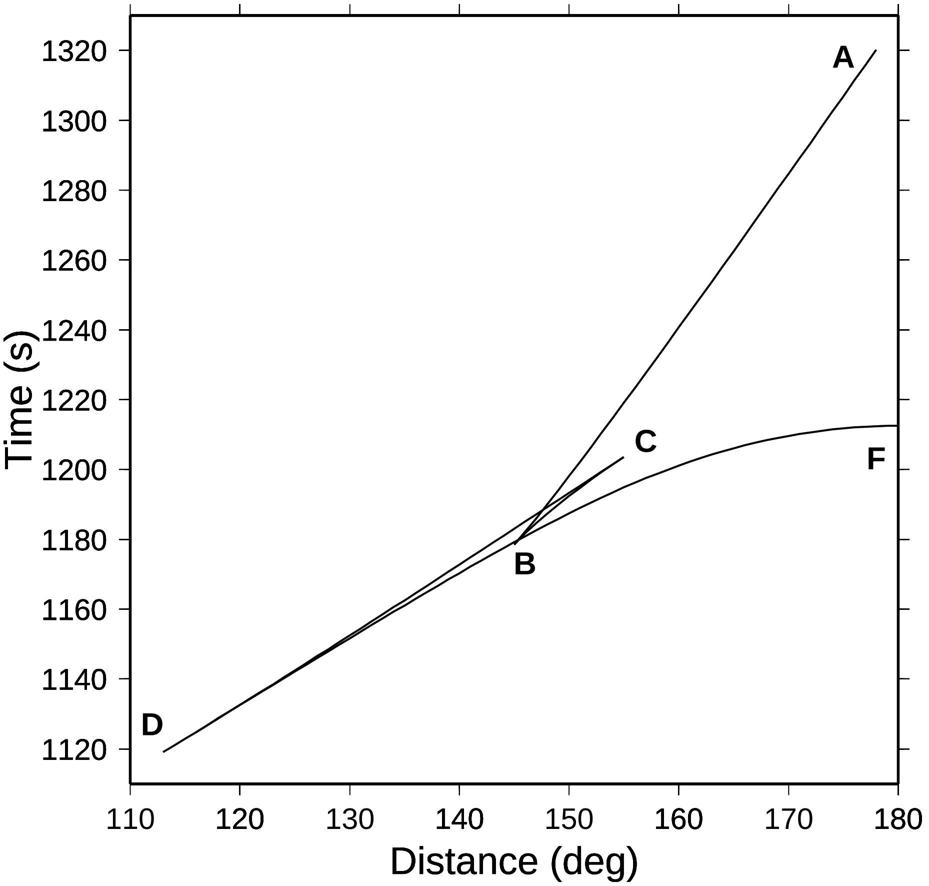

Figure 2.2. Theoretical travel-time curves for PKP branches for ak135 reference model

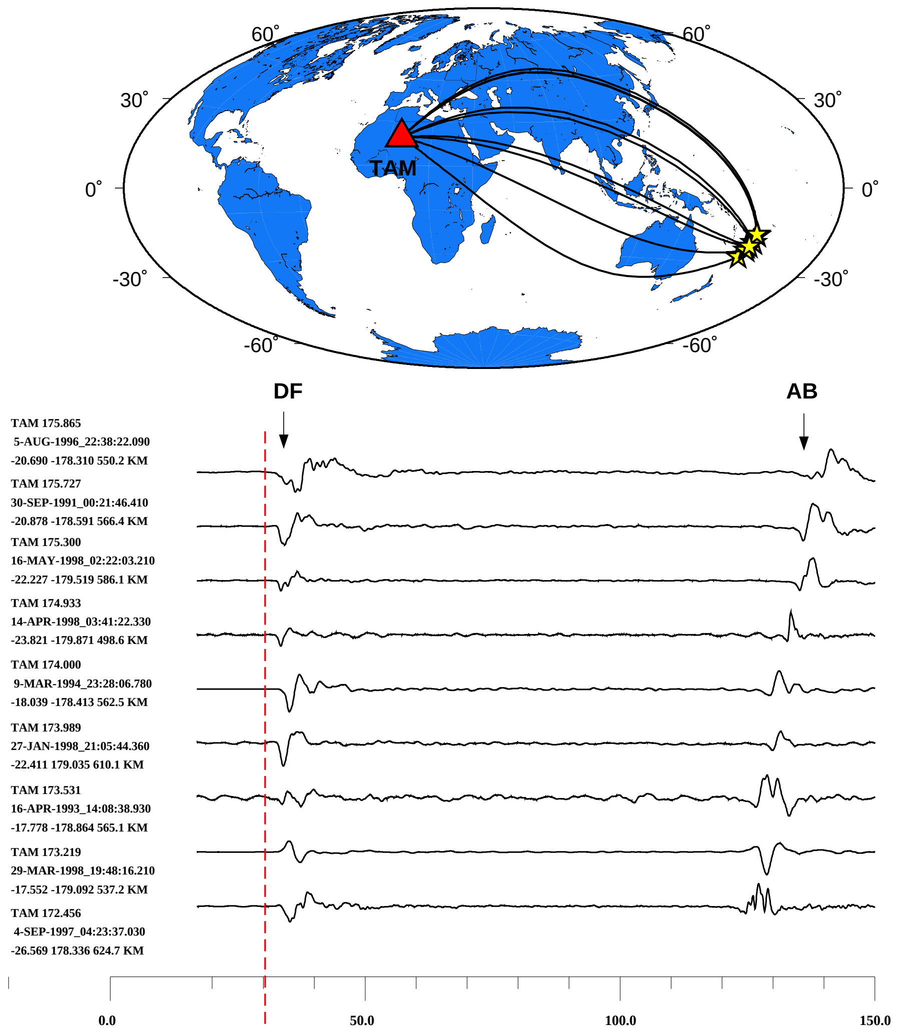

Figure 2.3. Top: Projections of the raypaths for the Fiji Islands events (yellow stars) recorded at the Geoscope station TAM. Bottom: Seismograms corresponding to the paths shown above. PKP(DF) and PKP(AB) arrivals are indicated by black arrows. Red dashed line corresponds to ak135 model predictions for PKP(DF) arrival times. The hypocenter information and distance to the station are plotted to the left of each seismogram.

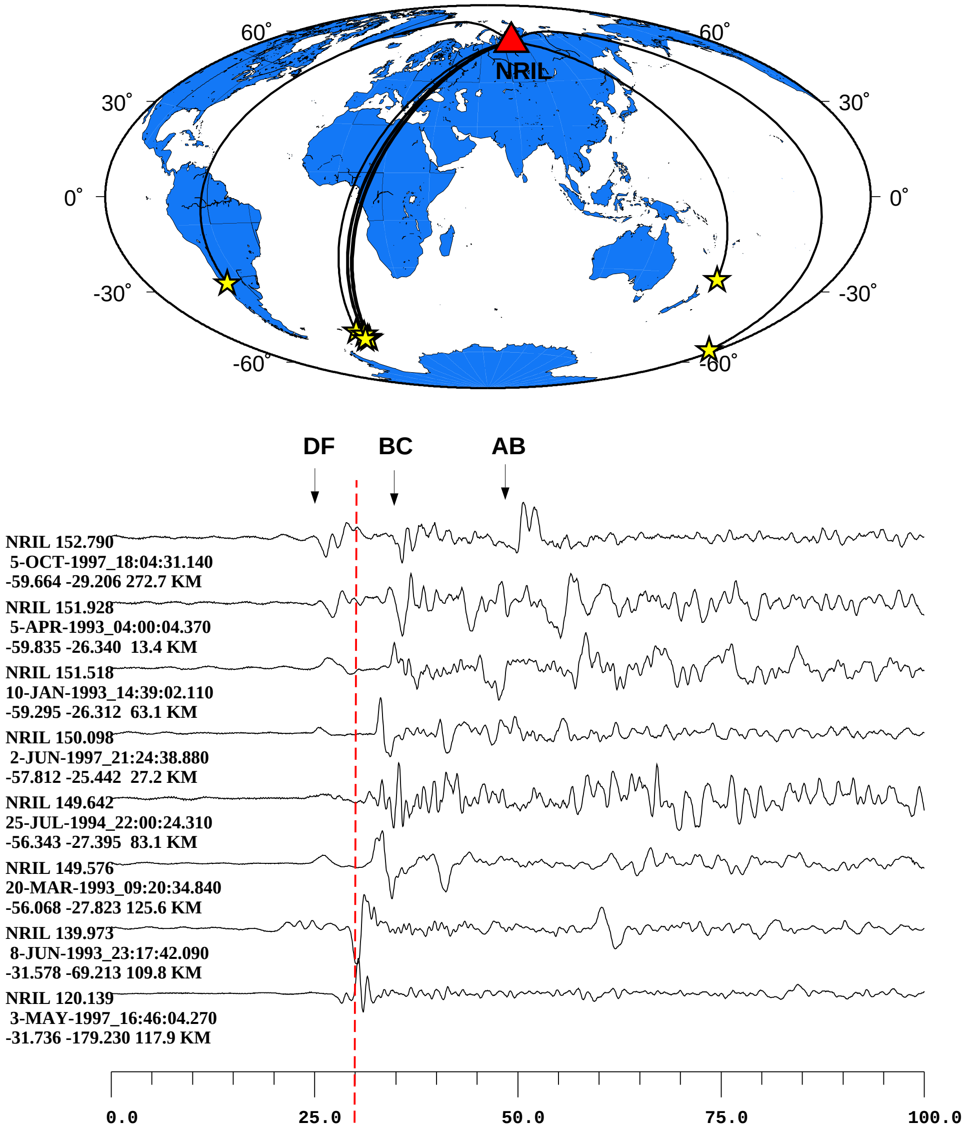

Figure 2.4. Top: Projections of the raypaths for the southern hemisphere events (yellow stars) recorded at the GSN station NRIL. Bottom: Seismograms corresponding to the paths shown above. PKP(DF) and PKP(AB) arrivals are indicated by black arrows. Red dashed line corresponds to ak135 model predictions for PKP(DF) arrival times. The hypocenter information and distance to the station are plotted to the left of each seismogram.

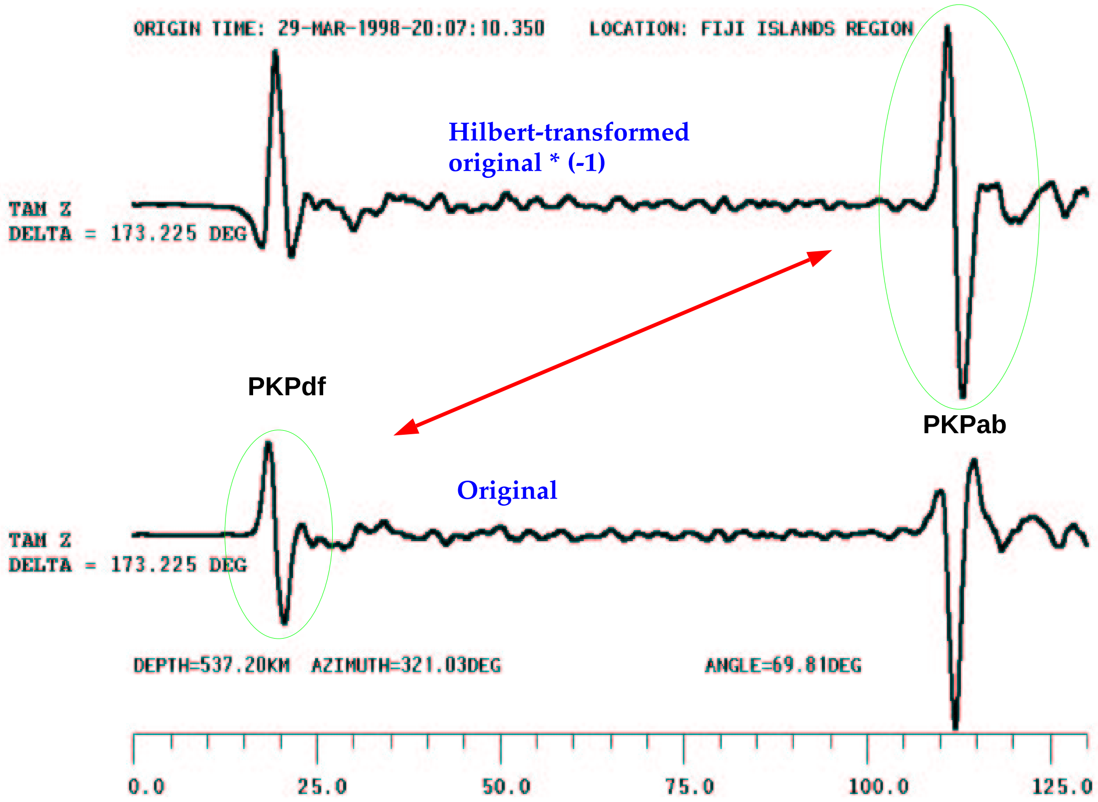

Figure 2.5. Applying Hilbert transform and changing the polarity of PKPab phase produces a waveform similar to PKPdf.

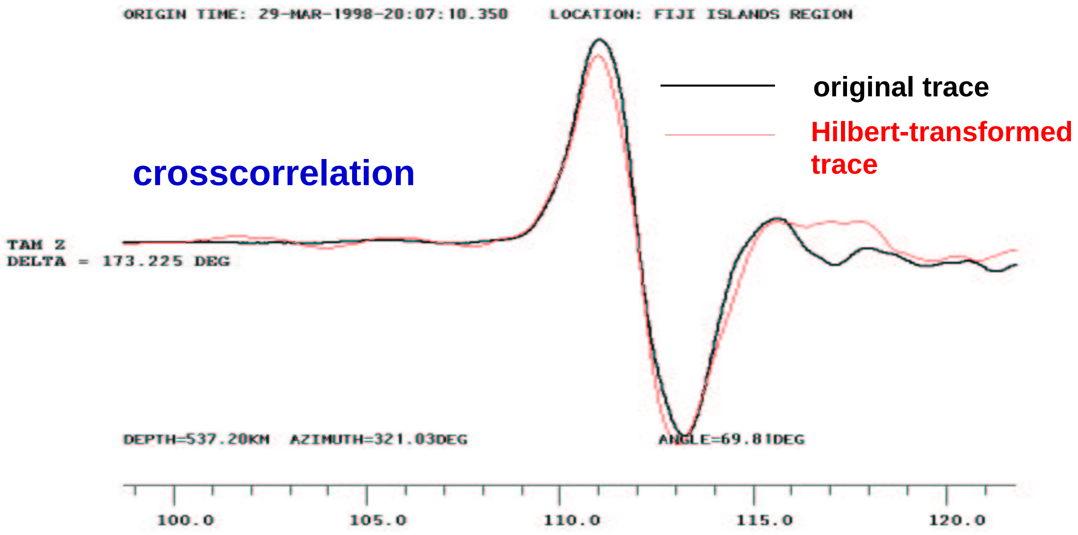

Figure 2.6. Overlapping the PKPdf waveform from the original trace and the PKPab waveform from the Hilbert-transformed trace, allows a measurement of the travel time shift between them, with great accuracy.

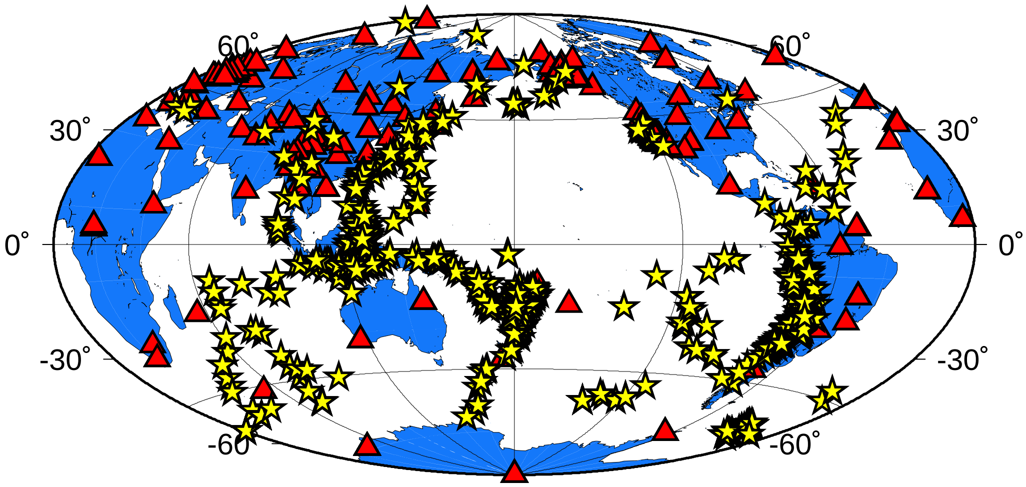

Figure 2.7. Earthquakes (stars) and stations (triangles) used to collect PKP(AB-DF) differential travel time measurements.

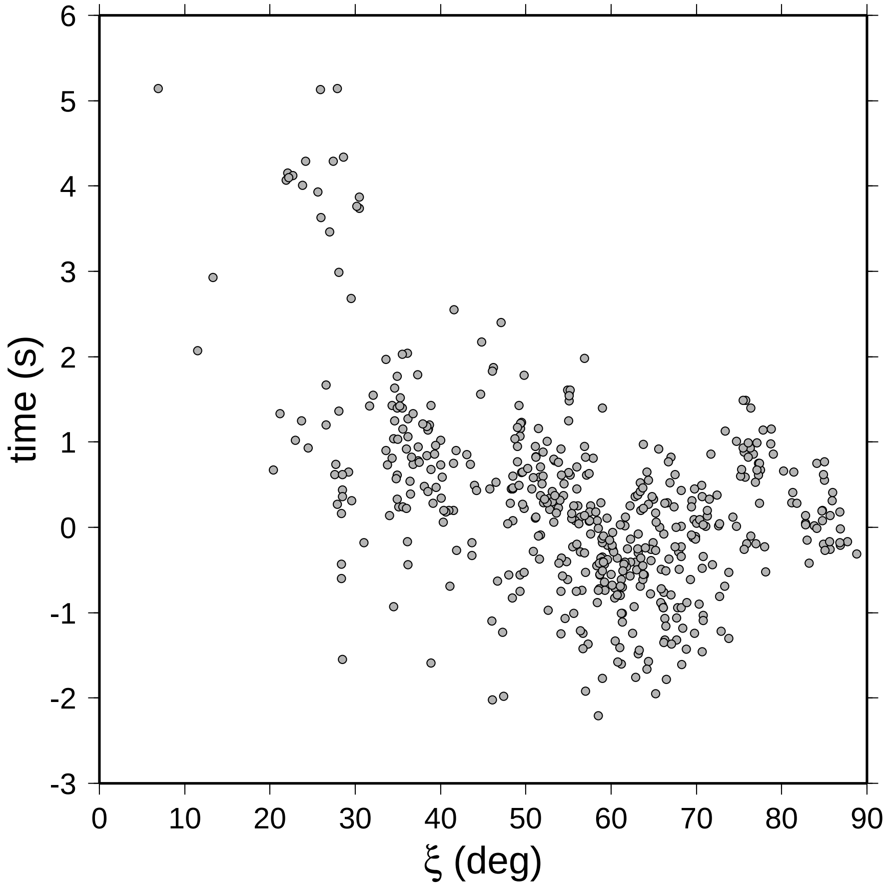

Figure 2.8. The dataset of PKP(AB-DF) differential travel time residuals plotted with respect to the angle ξ between the PKP(DF) leg in the inner core and the rotation axis of Earth. Residuals are calculated with respect to the ak135 model [*Kennett et al.*, 1995]. Standard ellipticity corrections were applied. All earthquake locations and origin times are corrected with respect to the relocation catalog of [*Engdahl et al.*, 1998].

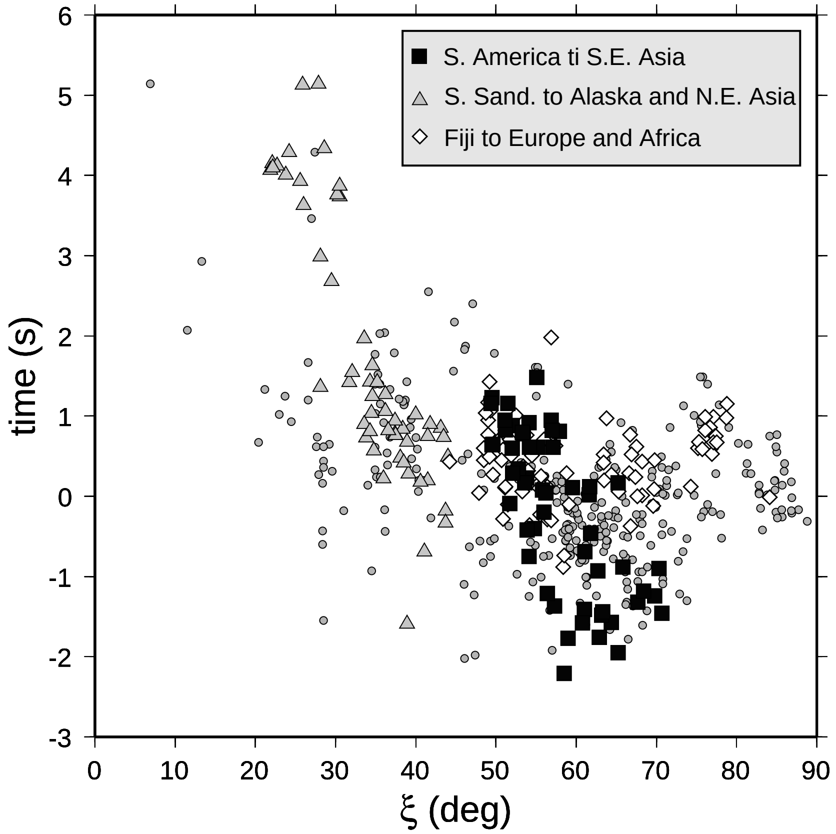

Figure 2.9. Same as Figure 2.8, but the subsets of PKP(AB-DF) data corresponding to specific geographic coverage of their paths are indicated with different symbols. Triangles correspond to the earthquakes from South Sandwich Islands region recorded in Alaska and north Asia. Solid squares correspond to south American earthquakes recorded in Asia. White diamonds correspond to Fiji Island region earthquakes recorded at stations in Africa and Europe.

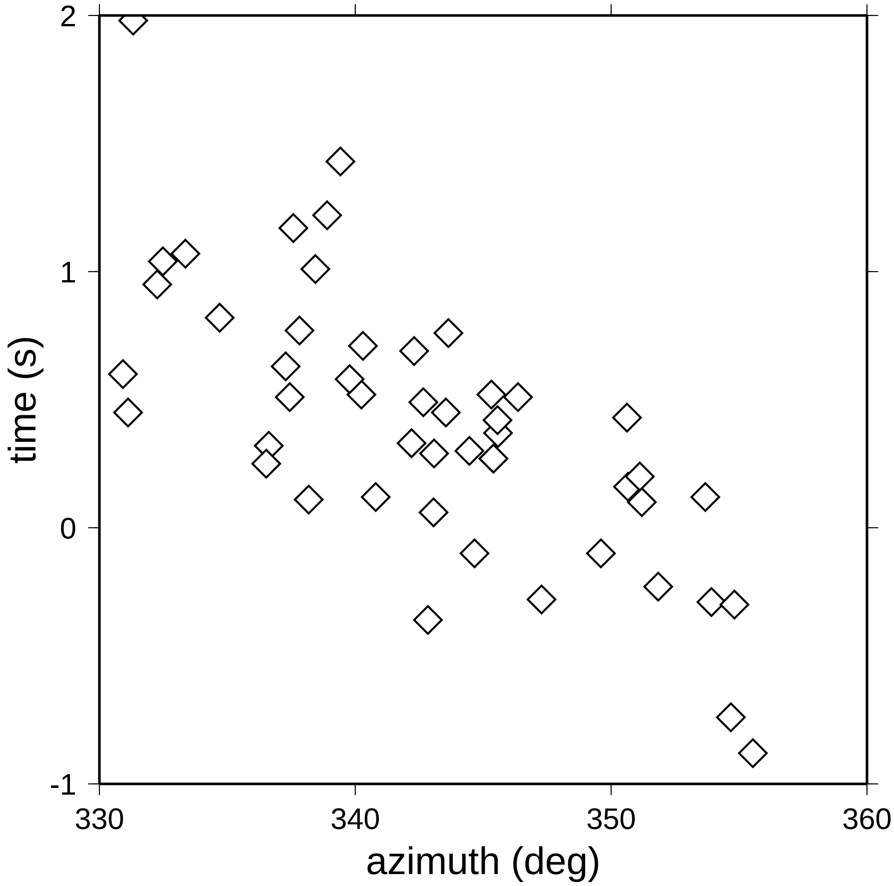

Figure 2.10. The subset of PKP(AB-DF) differential travel time residuals corresponding to the paths from Fiji Island region events recorded in Europe, plotted as a function of station azimuth.

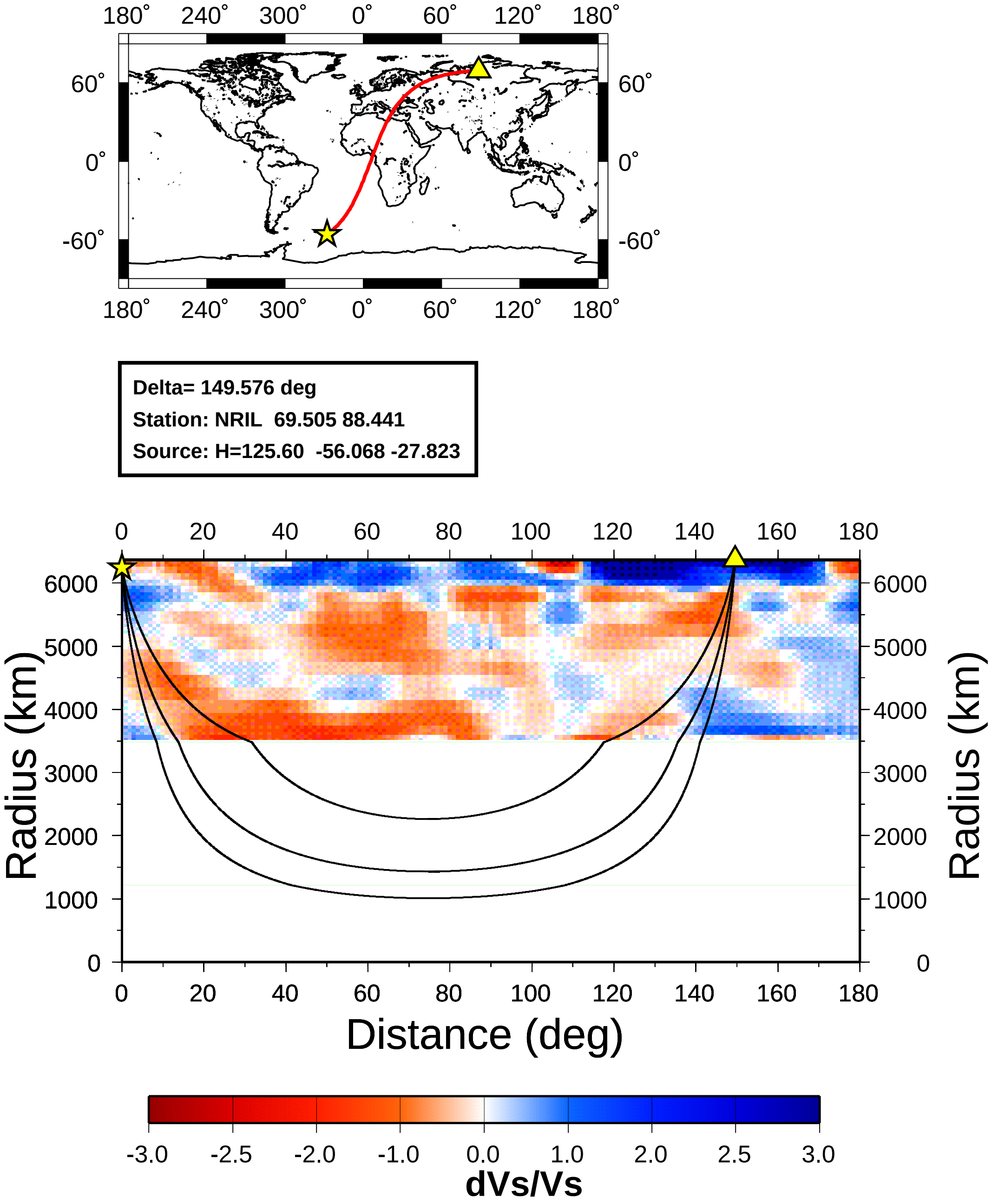

Figure 2.11. Top: PKP path from South Sandwich Islands to NRIL station. Bottom: Cross-section through the Earth, along the profile indicated in the top figure, with [*Mégnin and Romanowicz*, 2000] S velocity model in the background. PKP(AB), PKP(BC) and PKP(DF) rays are shown by black lines.

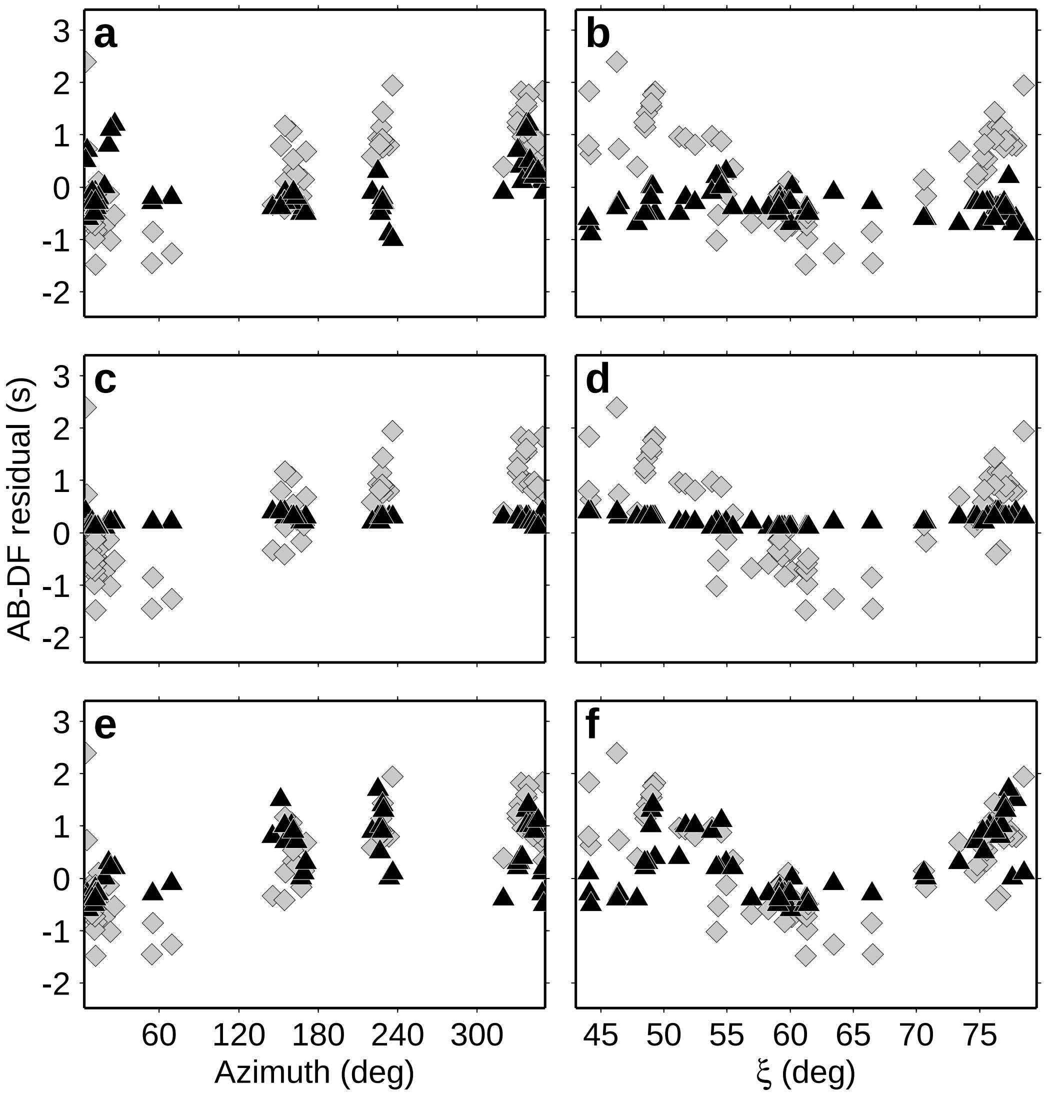

Figure 2.12. Observed AB-DF travel time residuals (gray diamonds) for events located in the Fiji Islands region as a function of azimuth from the source (left) and angle ξ with respect to the earth's rotation axis (right). Predicted anomalies (black triangles) are (a)(b) for the tomographic model by [*Grand et al.*, 1997] converted to P using a constant scaling factor 0.55, (c)(d) for inner core anisotropy model by [*Creager*, 1992], and (e)(f) for the MMM model by [*Bréger et al.*, 2000].

Chapter 3

Constraints on D" structure using PKP(AB-DF), PKP(BC-DF) and PcP-P travel time data from broadband records

This chapter is a slightly modified preprint of a publication currently in press [*Tkalčić et al.*, 2001] in *GJI*.

3.1 Abstract

The effects of complex structure in the deep mantle and D" on PKP differential travel times should be accurately estimated in order to reach reliable conclusions about the physical and chemical properties of the Earth's inner and outer core. In particular, it is important to assess how much of the data can be explained by mantle structure alone. For this purpose, we have assembled global data sets of high quality PKP(AB-DF), PKP(BC-DF) and PcP-P differential travel times measured on mostly broadband records. The PKP(AB-DF) data were inverted alone or jointly with PcP-P data, to retrieve P velocity maps of the lowermost 300 km of the mantle. Corrections for mantle structure above D" were performed prior to inversion using recent tomographic models and the fit to the PKP(BC-DF) dataset

was used to constrain damping in the inversions. We compare models obtained with and without polar PKP paths and find that their inclusion or exclusion does not significantly affect the resulting D" model except under North America, where coverage is poor without polar paths. Our preferred model, obtained using PKP(AB-DF) and PcP-P data combined, explains over 80% of the variance in PKP(AB-DF), almost 60% of the variance in PcP-P and 27% of the variance in PKP(BC-DF), a significant accomplishment considering that the PKP(BC-DF) dataset was not used in the inversion. Our models are characterized by prominent fast features under middle America and east Asia, a fast belt across Pacific, a slow region under the southwestern Pacific and southern Africa, as well as sharp transitions from fast to slow, for instance under Alaska and the south Atlantic. The anomalous South Sandwich to Alaska data cannot be fully explained by D" structure alone, unless very short wavelength lateral variations are introduced. Models that allow for a modest level of constant transverse anisotropy in the inner core, compatible with normal mode splitting data, perform somewhat better, but still fail to explain 2 sec in PKP(BC-DF) residuals, on these anomalous paths.

3.2 Introduction

In the last fifteen years, numerous studies have documented the existence of lateral heterogeneity in D" at many different scales. Global S wave tomographic models indicate a significant increase in the rms velocity perturbations in the last 500 km of the mantle (e.g. [*Su et al.*, 1994; *Masters et al.*, 1996; *Li and Romanowicz*, 1996]) and a change in the spectrum of heterogeneity, with a shift to low degrees. This is manifested by the now well known pattern of large low velocity "plumes" in the central Pacific and under Africa, surrounded by a "ring" of high velocities. While there is clear evidence from these studies for the existence of a simple, long wavelength pattern of heterogeneity in D", short-period studies of precursors to core phases indicate the presence of small scale heterogeneity, as well (e.g. [*Haddon and Cleary*, 1974; *Husebye et al.*, 1976; *Doornbos*, 1974; *Bataille and Flatte*, 1988]). More recent studies, based on observations of diffracted waves, have documented the existence of heterogeneity at intermediate scales (e.g. [*Wysession et al.*, 1992; *Wysession et al.*, 1995; *Wysession*, 1996; *Kuo*, 1999; *Souriau and Poupinet*, 1994]). Also, the amplitude of the lateral velocity variations has been shown to be larger by a factor of 2 to 3 than found from tomographic studies ([*Bréger et al.*, 2000; *Ritsema et al.*, 1998]), with strong lateral gradients over distances of a few hundred km [*Bréger and Romanowicz*, 1998; *Ni and Helmberger*, 2001]. There is also evidence for the presence of extreme structures, such as ultra-low P velocity zones [*Garnero and Helmberger*, 1995; *Garnero and Helmberger*, 1996; *Sylvander et al.*, 1997], which may require partial melting (e.g. [*Williams and Garnero*, 1996]).

While most studies of D" use body waves turning in the mantle, the core phase PKP(AB), which interacts with D" at grazing incidence (Figure 3.1), can also be used to investigate lateral heterogeneity at the base of the mantle. Attempts at such studies were pioneered by [*Sacks et al.*, 1979; *Snocke and Sacks*, 1986], who interpreted amplitude ratios of PKP(AB) and PKP(DF) in terms of heterogeneity in D". [*Sylvander and Souriau*, 1996b] used PKP(AB-BC) differential travel times to retrieve P-velocity structure in the lowermost 300 km of the mantle. More recently, [*Bréger et al.*, 2000] showed, in a forward modeling experiment, that realistic modifications to existing lowermost mantle tomographic models could explain most of the trends in the observed PKP(AB-DF) travel time data, including variations with angle of the DF ray-path, as measured at its bottoming point, with respect to the axis of rotation of the earth. These variations are generally interpreted in terms of simple models of anisotropy in the inner core, as first proposed by [*Morelli et al.*, 1986]. [*Bréger et al.*, 2000] proposed that the observed trends were largely due to the interaction of unevenly distributed PKP paths with the strong gradients of structure at the border of the African plume. There have also been attempts to retrieve core-mantle topography using PKP phases, with little agreement in the results, most likely due to trade-offs between CMB topography and heterogeneity in D" combined with the noisy character of the ISC dataset used (i.e. [*Creager and Jordan*, 1986; *Morelli et al.*, 1986; *Rodgers and Wahr*, 1993; *Garcia and Souriau*, 2000]).

There are two problems with the use of core phases to study D". First, the sampling of D" achieved with the existing global dataset is sparse, and makes it difficult to resolve the ambiguity on the location of the heterogeneity on the source or the station leg of PKP(AB) in D". This can be remedied, to some extent, by using PKP data as a complement to other mantle sensitive data, such as P travel times, as has been done recently by [*Kárason* *and Hilst*, 2001]. The second problem is that, by using PKP(DF) as a reference phase, we introduce potential biases due to inner core anisotropy or heterogeneity. To avoid issues related to trade-offs between inner core anisotropy and mantle structure, PKP data corresponding only to quasi-equatorial paths (waves traveling at large angles with respect to the earth's rotation axis) are generally considered for the study of D" structure.

In the present study, we analyze a global dataset of carefully measured PKP(AB-DF) travel-times in an attempt to retrieve structure in the last 300 km of the mantle. We correct data for mantle structure using various existing P and S tomographic models, choosing the model which provides the best fits to our datasets. We complement the PKP(AB-DF) dataset with a global dataset of hand-picked PcP-P differential travel times to help resolve ambiguity on the location of heterogeneity on source or receiver sides. We also have collected a dataset of hand-picked PKP(BC-DF) travel times, which we use as constraints on the overall damping in our inversions. We compare models obtained using subsets of PKP(AB-DF) travel time data, in particular removing or including polar paths or the anomalous paths corresponding to sources in the South Sandwich Islands and stations in Alaska, in order to assess what portion of the dataset requires structure in the core. Finally, we also consider models in which we first correct the data for transverse isotropy in the inner core, at a level compatible with core mode splitting data.

3.3 Datasets and data selection

We use hand-picked PKP(AB-DF), PKP(BC-DF) and PcP-P datasets of the highest quality, from a variety of sources. Using differential travel time data reduces biases of mislocation in space and time, as well as unwanted effects imposed by source and receiver structure, due to proximity of paths of the two rays in the crust and the upper mantle (e.g. [*Cormier and Choy*, 1986; *Creager*, 1992]) (Figure 3.1). Any of these unwanted effects should have similar influence on both rays, and thus can be significantly reduced.

PKP(DF) is taken as the reference phase in this study, because the coverage of D" available using PKP(AB-BC) is much more limited due to the narrow epicentral distance range at which PKP(BC) is present. We therefore need to carefully consider possible effects of the inner core. On the other hand, it allows us to experiment regarding trade-offs between mantle and core structure.

3.3.1 PKP(AB-DF) dataset

Our own dataset (subset 1) comprises differential travel times measured on vertical component seismograms primarily from broadband digital stations, complemented by about 20 measurements from short-period records. Our dataset represents an augmented version of the one considered in [*Bréger et al.*, 2000] and referred to in [*Garnero*, 2000]. Measurements are done by applying techniques described in the previous chapter, and examples are shown in Figures 2.5 and 2.6.

In addition to measurement errors, we need to consider errors due to source mislocation, even though we used relocated event parameters according to [*Engdahl et al.*, 1998]. For instance, in PKP(AB-DF) differential travel times, at epicentral distances of 150 and 175^o, a 10 km error in the hypocentral location yields a differential time error of about 0.2 and 0.4 seconds, respectively. Similarly, at epicentral distances of 25 and 75^o, a 10 km error in the hypocentral location would yield an error in PcP-P differential travel times of about 0.7 and 0.1 seconds, respectively. In summary, the total error in the differential residuals is estimated to be on the order of 0.5 to 1 sec.

In order to obtain optimal sampling of D", we complemented our dataset with 3 other existing subsets of hand-picked PKP data, from which all measurements qualified as "poor" or worse were disregarded. Subset 2 comprises high quality measurements from short period instruments [*McSweeney et al.*, 1997; *Creager*, 1999]. Subset 3 contains mostly data from broadband instruments of the GEOSCOPE network (*Souriau*, personal communication). Finally, subset 4 comprises data derived from seismograms of a broadband PASSCAL experiment in India (*Wysession*, personal communication). To avoid redundancy of measurements, we had to set some selective criteria. We used our own complete dataset as a starting point, and added the largest one of the three remaining datasets (subset 2), removing the repetitive measurements from it. Then, we added subset 3 and finally subset 4, repeating the procedure of removing the repetitive measurements. This procedure only slightly reduced the total number of measurements, since the four datasets are mutually complementary. The closer analysis of multiple measurements showed a great level of consistency among different seismogram-readers, which is not surprising, since we limited ourselves to only the highest quality data. We found in these cases when data overlaps that the measurement error is on the order of 0.5 seconds or less. Furthermore, suspicious anomalous data were detected and rejected on the basis of cross checking trends for individual stations and individual earthquake source regions.

Furthermore, in order to avoid too much emphasis on specific paths, we used the summary ray approach to reduce the number of data on oversampled paths. In particular, two events, one from the southern mid-Atlantic ridge (90/04/30) and one located south of Africa (93/03/29), were well recorded at the short period Alaskan network and at short period networks in California, respectively [*McSweeney et al.*, 1997]. An unusually good signal to noise ratio resulted in a couple of hundreds of picks, which we reduced to only about 20, by creating summary rays with respect to epicentral distance and azimuth. However, these measurements, along with others in Alaska, are of great importance in investigating the short scale deep mantle heterogeneity as shown in [*Romanowicz et al.*, 2001].

The final dataset comprises a total of 1329 high-quality PKP(AB-DF) differential travel times. We computed travel time residuals with respect to the standard ak135 model [*Kennett et al.*, 1995] accounting for Earth's ellipticity *(Kennett and Engdahl*, personal communication), and after relocation according to [*Engdahl et al.*, 1998]. The travel time residuals from the different subsets considered (after declustering as mentioned above) are displayed in Figure 3.2 (a, b) as a function of angle with respect to the earth's rotation axis (this angle is hereafter called ξ). Figure 3.2 (a) shows that there could be two trends in the residuals. Previous studies fit a single curve to the data. However, the residuals shown in Figure 3.2 (a) suggest that it may be appropriate to consider different trends for the data corresponding to ξ smaller and larger than 35^o degrees. For angles smaller than 35^o, residuals are shifted toward higher values on average, although a large scatter at $\xi \approx 30^o$ is evident. All 5 residuals available for $\xi < 20^o$ are positive and larger than about 1.5 s. Taking a closer look at the traces from this group reveals that large residuals are mostly due to advanced PKP(DF) arrivals with respect to the ak135 model that we use as reference. Some specific paths are indicated on the same figure. The majority of the most anomalous data correspond to measurements obtained from the short period Alaskan network from a single event on the south Atlantic mid-ocean ridge (04/30/1990, 54.28S/1.27E), and measurements originating from South Sandwich Islands' events recorded on station COL in Alaska and stations SEY, NRIL and BILL in northeast Asia. In addition, there is one very anomalous measurement corresponding to PKP arrivals from the northern hemisphere (Svalbard region), recorded at station SPA (South Pole).

It is clear that models of constant anisotropy throughout the inner core cannot explain such scatter of data, in particular the range of over 5 seconds at ξ about 30^o. Between about 30 and 45^o, residuals span over 7 seconds (from about +5 to -2 seconds). Adopting the definition of quasi-eastern (longitude from $+43^o$E to $+177^o$E) and quasi-western hemisphere of [*Tanaka and Hamaguchi*, 1997] yields results that are in agreement with these authors' work (Figure 3.2 (b)). Most of the largest residuals correspond to PKP(DF) turning in the quasi-western hemisphere. For the equatorial paths, the scatter is smaller for the quasi-eastern hemisphere, which is, on average, faster (e.g. [*Creager*, 1999]). Furthermore, in the western hemisphere, excepting the cluster of very anomalous paths around $\xi = 30^o$, very few data points are available to indicate the characteristic trend of progressively increasing anomaly for polar paths. In fact, all but one very polar path ($\xi < 20^o$, station SPA) have smaller residuals than the paths corresponding to slightly larger ξ.

3.3.2 PKP(BC-DF) dataset

We have also assembled a high quality PKP(BC-DF) dataset, following the same selective criteria as in collecting PKP(AB-DF) data. This dataset will not be used directly in the inversion, but rather to test how well the D" model derived from PKP(AB-DF) and PcP data can explain the PKP(BC-DF) travel time residuals. The advantage of PKP(BC-DF) is that the ray paths for the two branches are close together throughout the mantle, so that corrections for mantle structure (outside of D") are less critical than for PKP(AB-DF). However, the sampling of D" is rather poor for BC-DF. Also, the separation of the two phases is less than 400km in D", so that BC-DF is best suited to study short scale heterogeneity at a regional scale, which is beyond the scope of of our study. Testing the fit to PKP(BC-DF) of the D" model obtained using PKP(AB-DF) and PcP-P can provide information on the scale of lateral heterogeneity in D", and on how much structure might be required in the core.

The PKP(BC-DF) dataset used in this study also consists of four independent subsets. We used our own dataset as a base, and added the largest one of the three remaining datasets [*McSweeney et al.*, 1997; *Creager*, 1999], removing the repetitive measurements from it. Then, we added subset 3 [*Tanaka and Hamaguchi*, 1997] and subset 4 *(Souriau*, personal communication), repeating the procedure of reducing the repetitive measurements. The total number of data after declustering is 901. Travel time residuals were calculated with respect to model ak135 and corrected for ellipticity, using relocated event coordinates from [*Engdahl et al.*, 1998]. In addition, we declustered the PKP(BC-DF) dataset, following the same summary ray approach as described in the previous section on PKP(AB-DF) data. PKP(BC-DF) residuals from all four subsets are plotted in Figure 3.3 (a) as a function of ξ. Comparing with Figure 3.2 (a), it is clear that the scatter in equatorial PKP(BC-DF) data is less pronounced than in PKP(AB-DF) residuals. Residuals span roughly from 4.6 to -1.2 seconds and equatorial data are largely confined between ± 1 s (compared to ± 2 s for AB-DF). This is generally interpreted as being due to the fact that the paths of BC and DF are much closer than those of AB and DF in the mantle, particularly so in D".

In Figure 3.3 (b), we plotted the PKP(BC-DF) dataset with respect to ξ, distinguishing the two quasi-hemispheres, as defined above. The results confirm those of [*Tanaka and Hamaguchi*, 1997] (their figure 11) and [*Creager*, 1999] (his figure 2b, although his definition of hemispheres is somewhat different): the quasi-eastern hemisphere is faster on average, and does not show a strong trend of increasing residuals with decreasing angle ξ, in contrast to the quasi-western hemisphere. There are, however, other important observations: first, some very polar paths ($10^o < \xi < 20^o$) have smaller residuals than paths corresponding to larger ξ, just as was the case for PKP(AB-DF). Second, for ξ between $\approx 20^o$ and 30^o, the data can be fit rather well with a steep linear trend, spanning almost 5 seconds in travel time anomaly (from +4.6 to -0.3 seconds).

Just as for PKP(AB-DF), in order to fit the data in the western hemisphere with a constant transverse anisotropy model of the inner core as proposed by [*Creager*, 1992], one needs to exclude the South Sandwich/South Atlantic to Alaska paths. Since DF is the common phase in both datasets, the simplest explanation, as proposed by [*Creager*, 1999], is that the anomalous observations corresponding to these paths originate in the inner core. A recent analysis of Alaskan data indicates that this anomaly is sensed by both PKP(DF) and PKP(BC) and therefore must originate outside of the inner core [*Romanowicz et al.*, 2001].

3.3.3 PcP-P dataset

To complement the PKP(AB-DF) dataset with independent data that can help resolve the source/station side ambiguity, we measured 1219 PcP-P differential travel times . The compatibility of the datasets can be tested by comparing the models obtained using PKP(AB-DF) data alone, versus using the joint dataset.

In selecting our PcP-P dataset, we had to take into account the specific difficulties encountered with PcP measurements. PcP arrivals are very often buried in microseismic noise, especially for stations closer to the oceans. At epicentral distances larger than about 70 degrees (depending on focal depth), they are buried in the P wave coda. The PcP-P measurements are also made more difficult by the interference of surface phases with PcP arrivals for shallow earthquakes. Again, we selected only high quality vertical component data from broadband stations worldwide, assembling a unique global dataset of hand-picked PcP-P travel time residuals in the distance range from about 25^o to 75^o.

The measurements are performed using the same waveform correlation methodology as described earlier for PKP. The residuals are computed with respect to the theoretical travel times from ak135 model [*Kennett et al.*, 1995], using relocated event coordinates [*Engdahl et al.*, 1998], and corrected for ellipticity. Such calculated residuals vary in amplitude between -3 and 3 seconds. The residuals and coverage are shown in map form in Figure 3.4.

While the global coverage obtained with PcP-P is far from complete, in areas where there is good coverage we note a high level of spatial coherency in the data. An area of particular interest is middle America, where the alternation of positive and negative residuals indicates sharp lateral gradients on scale lengths of several hundred km in the deep mantle, in agreement with recent results based on ScS-S data [*Wysession et al.*, 2001].

3.4 Corrections for mantle structure

Since we only invert for structure in the last 300 km of the mantle, to which the PKP(AB-DF) dataset is most sensitive, we need to take into account the possible contribution of overlying mantle heterogeneity. For this, we correct the observed residuals using predictions from available global tomographic mantle models. We select the model that provides the best variance reduction for our dataset by systematically testing five P mantle tomographic models. We introduce a scaling factor h, to allow for the uncertainty in the amplitudes of lateral variations inherent to tomographic inversions. Scaling factor h is defined as $V_p(new) = h * V_p(orig)$, where $V_p(orig)$ is the input tomographic model and $V_p(new)$ is a virtual (scaled) model. A "good" original P model should yield $h \approx 1$. If $h > 1$, the input model is overdamped, and if $h < 1$, it is either underdamped or, if combined with a small variance reduction, the distribution of heterogeneity may not be compatible with the PKP dataset everywhere, so that the fitting procedure tends to minimize the contributions of the tomographic model.

For the purpose of the present study, we have calculated PKP(AB-DF) traveltime corrections for: a) the whole mantle and b) for the whole mantle without the lowermost 300 km thick layer. Paths from the same source region (sphere of radius $r = 100$km) sampling the same block ($5x5^o$) at CMB were grouped and weighted prior to calculating the variance reduction, according to criteria of similar sampling in the mantle. For instance, for the PKP(AB-DF) quasi-equatorial subset, out of 1239 PKP(AB-DF) ray pairs, we formed 610 bins with single rays, 126 bins with 2 rays, and 82 bins with 3 or more rays.

Figure 3.5 (a) shows the variance reduction in the equatorial subset of PKP(AB-DF) data ($\xi > 35^o$), plotted as a function of h, for five different global P velocity mantle models [*Boschi and Dziewonski*, 2000; *van der Hilst et al.*, 1997; *Kárason and Hilst*, 2001; *Obayashi and Fukao*, 1997; *Vasco and Johnson*, 1998]. The model that gives the best variance reduction is that of [*Kárason and Hilst*, 2001], hereafter called KH2001 for the whole mantle, and KH2001m for the mantle stripped of the lowermost 300 km. For this model (as for others too), the best-fitting h is less than 1. It is closest to 1 when the bottom layer of the mantle is excluded, although in that case, the variance reduction is smaller. We infer tentatively that the detailed distribution of heterogeneity predicted by the tomographic P models is not perfectly compatible with the PKP data, particularly in D", or that, possibly, all the P models are underdamped.

We repeated the same experiment for the PcP-P dataset, which is not affected by structure in the core, and furthermore, none of these data have been used in the construction of the tomographic models being tested. Interestingly, the KH2001 model also gives the best variance reduction in this case, and with a similar amplitude (Figure 3.5 (b)). This indicates that the choice of the KH2001 model does not reflect a circular argument, as one might assume, given that some of the PKP(AB-DF) data (measured by T. McSweeney and K. Creager) were used in the construction of KH2001. The experiment with PcP-P gives somewhat larger scaling coefficients than for PKP(AB-DF), close to 1 for the model stripped of the last 300km of the mantle (KH2001m), indicating that overdamping is not the main factor leading to scaling factors smaller than 1, when PKP(AB-DF) data are used. Rather, there is indeed some distribution of heterogeneity sampled by the PKP(AB-DF) dataset that is not present in KH2001. Thus, although the best-fitting model for PKP(AB-DF) is for $h < 1$, we prefer to use the original model ($h = 1$) to correct residuals for mantle structure.

Relatively low percentages of variance reduction in both datasets open the question of how well modeled the lowermost mantle layer is, in tomographic models. Our analysis shows that it is reasonable to assume that present mantle models can account for about $20 - 25\%$ of the variance in equatorial PKP(AB-DF) differential travel time data. The P velocity model KH2001m is our preferred model for correcting both PKP(AB-DF) and (PcP-P) travel times due to larger variance reduction in comparison with other P models. Various S models [*Gu and Dziewonski*, 2001; *Masters et al.*, 1999; *Mégnin and Romanowicz*, 2000; *Grand et al.*, 1997] have also been tested with depth dependent scaling factors [*Tkalčić and Romanowicz*, 2001], however they yield a smaller variance reduction in both PKP and PcP datasets, possibly indicating a lack of systematic correlation between P and S velocity heterogeneity in D" (e.g. [*Wysession et al.*, 1992]).

Recently, [*Bréger et al.*, 2000], showed by forward modeling that the trend in PKP(AB-DF) residuals with respect to the angle ξ can be explained to a large extent by structure in D". According to another study [*Creager*, 1999], polar PKP(AB-DF) data show no correlation with the predictions from mantle models, concluding that there appears to be no significant contamination of the anisotropy signal by mantle structure. By using the model KH2001, we calculated correlation coefficients between mantle predictions and the PKP(AB-DF) residuals, for the case of the complete dataset and for the case of equatorial and polar subsets only (by using an arbitrary angle $\xi = 35^o$ to separate the two subsets of data). The results are shown in Table 3.1.

Correlation coefficients between observations and predictions are relatively high for both PKP and PcP data, especially for the polar subset. This is expected for PKP, since KH2001 is constructed by including some manually picked PKP data, although previously corrected for inner core anisotropy. Furthermore, variance reductions are best for the polar PKP dataset which could indicate a contribution of mantle structure to the trends seen in the polar paths. When we exclude the lowermost 300 km of the mantle, variance reduction for polar PKP subset drops significantly, while it increases in the case of the equatorial subset.

Since PcP-P may be more sensitive to mantle structure above D" than PKP(AB-DF), we have investigated whether it makes sense to attribute the observed variations in PcP-P travel times to structure in D". Figure 3.6 shows the average relative velocity anomaly in D" required to explain PcP-P residuals, as a function of the length of the PcP path in the lowermost 300km of the mantle. The data have been corrected for the mantle above D" using the KH2001m model. The length of path in D" increases with epicentral distance, while the phases PcP and P have increasingly similar paths in the mantle. The range 700-1600 km corresponds to the epicentral distance range 30^o- 75^o.

If the tomographic model used to correct for the effects of the rest of the mantle is sufficiently accurate, Figure 3.6 shows that, because of the decrease of residuals with distance, to first order, the scale length of heterogeneity that contributes to the observed residuals must be less than about 1000 km, which is in agreement with the lateral variations seen in Figure 3.4. Because the residuals are organized symmetrically around the mean, we also infer that there are as many domains of faster than average velocities and of slower than average velocities. Thus, if there are domains of ultra-low velocity zones (e.g. [*Garnero et al.*, 1998], there must also be zones of very high velocity, in agreement with a recent suggestion based on observations of ScP waveforms [*Castle and van der Hilst*, 2000]. On the other hand, if model KH2001m does not adequately account for structure above D", the trends observed in Figure 3.6 could be at least partly explained by the decreasing separation between the two phases as distance increases.

3.5 Global Sampling and Parametrization

Figure 3.7 shows the distribution of surface projections of PKP(AB) and PKP(DF) legs sampling the lowermost 300 km of the mantle. It is clear from this figure, that the D" region is sampled well locally by PKP(AB) paths associated with earthquakes in the circum-pacific belt. The global coverage is limited not only by uneven global distribution of earthquakes, but also by the fact that differential travel-time measurements can be done only for stations that are located between about 150^o and 180^o in epicentral distance. In particular, regions beneath the mid-Pacific and Africa are not very well sampled. If the D" region is parametrized by equiangular 5^ox5^o block cells, it can be seen from Figure 3.8 (a) that the best sampled regions are located beneath South America, Caribbean Sea, southwestern Atlantic, Asia, southwestern Pacific and Australia. The number of hits per block in some areas, e.g. South Sandwich Islands, exceeds one hundred. Better sampling in certain regions does not proportionally increase the reliability of inversion results in the same regions, as it is very important to have crossing paths coming from different azimuths, in particular because of the problem of trade-off between source and receiver side of D". An example of such a potential resolution problem is for the numerous paths stretching from South Sandwich Island region to North America for which there aren't many crossing paths in north America. Comparison of Figure 3.7 and Figure 3.4 shows that inclusion of PcP-P data helps improve sampling in Asia, mid-America and Africa, and should help resolve source-receiver ambiguity in PKP on the paths between south Atlantic and Asia.

Although somewhat arbitrary, we use 300 km as a thickness for the D" layer, keeping in mind that fixed thickness trades off with the size of heterogeneity. We use two types of cell parametrization in this layer. In the first case, the layer is divided into a regular equiangle block grid with blocks of size 5^ox5^o (Figure 3.8 (a)). At the CMB depth at the equator, this is about 300x300 km^2 which is comparable to the layer thickness. In the second case, the layer is divided into a variable-size block grid (Figure 3.8 (b)). We devised a scheme to define the variable-size blocks based on sampling. Each block should have at least 3 hits and we increase the size of the block by coalescing neighboring blocks until the minimum hit count is reached. The largest cell size is set to be 10^ox10^o. If a cell shape with a number of counts ≥ 3 cannot be found, then that region is rejected and excluded from inversion (white areas in Figure 3.8 (b)). Our algorithm produces more uniform geographical distribution of counts and the "allowed" shapes are chosen in such a way that the final grid doesn't consist of excessively elongated shapes, but rather ones with aspect ratio close to 1 (in contrast to [*Bijwaard et al.*, 1998]. This technique allows us to preserve relatively small-sized blocks in regions with good coverage, while at the same time increasing the size in unsampled regions (compare Figures 3.8 (a) and (b).

Linear inversion is done by using LU (lower triangular-upper triangular) decomposition algorithm (*Press et al.,* 1988), and by adding various damping factors to diagonal elements. We didn't use any smoothness criteria, as several studies have documented strong lateral gradients of structure in D" and we wish to preserve those. The blocks that are not sampled are omitted, thus reducing the number of columns in the matrix. The variable size block approach ensures that the models obtained will not be strongly contaminated by the effects of undersampling.

In Figure 3.9, we show an example of a resolution test. We constructed a synthetic model with a checkerboard pattern in D" (a single layer), with the same size of heterogeneities as the size of the grid used in parametrization of our models (Figure 3.9 (a)), and no structure in the core. The output model for the optimal damping (as discussed below) and the entire PKP(AB-DF) and PcP-P dataset is shown in Figure 3.9 (b). The comparison with Figure 3.7 confirms that the best results are obtained in well covered regions (note that the projection in Figure 3.7 is centered on Africa in order to emphasize the polar paths from south Atlantic to Alaska, while the projection in Figure 3.9 is centered on Pacific). Non-sampled blocks are shown as white, non-gridded areas.

3.6 Discussion of resulting models

We have derived a series of models of P velocity anomalies in D" using different subsets of data, in order to investigate the effect of including or excluding polar/anomalous paths in the inversion, the constraints provided by the PcP-P dataset, and the effects of accounting for simple inner core anisotropy structure. The resulting models are labeled according to a scheme described in Table 3.2 for the models without and with inner core anisotropy, respectively. In both cases, we have considered inversions with 3 different subsets of PKP data : 1) the entire dataset 2) excluding quasi-polar data (angles $\xi < 40^o$) 3) excluding anomalous paths between the south-Atlantic and Alaska, but including other quasi-polar paths. Prior to inversion, we corrected PKP(AB-DF) and PcP-P data for mantle structure above D", using model KH2001m. In the series of inversions "with" inner core anisotropy, we also corrected the PKP(AB-DF) residuals for the particular inner core anisotropy model considered. We tried several recent models such as [*Creager*, 1992; *Durek and Romanowicz*, 1999; *Tromp*, 1993; *Tromp*, 1995].

In order to constrain the choice of damping in the inversions, we compute the fit to the PKP(BC-DF) dataset and keep the model that provides the best fit to this dataset. This will be discussed more extensively below.

The models derived using only PKP(AB-DF) data are not shown, for the sake of space. They are quite compatible with the models obtained using both PKP(AB-DF) and PcP-P, as can be assessed from the correlation coefficients shown in Table 3.3, except under southeastern Asia, where structure could not be well resolved with PKP(AB-DF) data alone (due to source-station ambiguity, which is resolved by the inclusion of PcP-P data). Since the joint PKP/PcP inversions correspond to better sampling of D", we concentrate on discussing those.

The models obtained using the complete PKP(AB-DF) dataset are shown in Figure 3.10. Prior to plotting the models, we smoothed them by using 3x3 blocks moving average scheme, and removed the mean. For the models with inner core anisotropy, the best fit to PKP(BC-DF) is obtained when correcting for the radially dependent model of inner core anisotropy derived to fit both normal mode and travel time data [*Tromp*, 1995]. We further refer to this model as TR95. The resulting D" model, labeled as TRH_KCa, is shown in Figure 3.10 (b).

The correlation coefficient between models TRH_KCa and TRH_KC (Figure 3.10, Table 3.3) is 0.71. Although amplitudes of P velocity anomalies in TRH_KCa are weaker (note the change in color palette), the distributions of anomalies in D" are very similar. Both models show prominent fast features in eastern Asia, Arabian Sea, south Atlantic, Carribean Sea and Alaska, as well as slow features in the southwest Pacific and under southern Africa. There is a horizontal band of fast velocities across the north Pacific, which is in agreement with some P models derived from ISC data (e.g. [*Boschi and Dziewonski*, 2000; *Obayashi and Fukao*, 1997; *Vasco and Johnson*, 1998]. Slow anomalies are observed under north America (somewhat stronger in model TRH_KC) which is not consistent with most P models derived from ISC data (e.g. [*Boschi and Dziewonski*, 2000; *Kárason and Hilst*, 2001; *Obayashi and Fukao*, 1997; *Vasco and Johnson*, 1998], but is consistent with the results of [*Sylvander and Souriau*, 1996b] and S velocity model by [*Masters et al.*, 1999].

In general, TRH_KCa doesn't differ much from TRH_KC, except south of Africa where TRH_KC has negative and TRH_KCa positive anomalies. Sharp transitions from fast to slow in the southern Atlantic, as well as in central America are present in both models. We will discuss the fits to the PKP(BC-DF) data extensively below.

In Figure 3.11, we further consider the influence of anomalous/polar paths on the inversions in which we do not correct data for inner core anisotropy. The models are here shown in a different, polar, projection, emphasizing the regions that might be most affected by the inclusion or exclusion of polar paths. Model TRH_KC, which includes all data, is shown again in Figure 3.11 (a), while Figures 3.11 (b) and 3.11 (c) show models TRH_KCeq (no equatorial paths) and TRH_KCnsa (no south atlantic to Alaska paths) respectively, as defined in Table 3.2.

All three models show generally good agreement, as can also be assessed from Table 3.3, which shows that correlation coefficients are between 0.76 and 0.93 for these models. When polar paths, which might be significantly affected by inner core anisotropy, are excluded (model TRH_KCeq, Figure 3.11 (b)), the coverage of D" decreases significantly under north America and the Atlantic Ocean. However, faster regions in south Atlantic and mid America remain stable after removal of the polar paths. The only prominent difference between this and the TRH_KC model (Figure 3.11 (a)) is the slow region beneath north America, which is not sampled by equatorial paths only. However, we saw in Figure 3.10, that this region remains mostly slow even when anisotropy is accounted for.

Although the number of hits per block under some parts of north America exceeds 10, there is not a substantial number of mutually crossing paths (Figure 3.7). The reason for this is that there are numerous stations, but fewer useful earthquakes in that region.

Most of the data that account for coverage under north America come from sources in south Atlantic, in particular from South Sandwich Islands region, and they are recorded by the Alaskan network. Hence, we could be mapping anomalies from the source side onto the receiver side of D". This could be addressed with some PcP data in north America. Unfortunately at this moment, there are not enough such data, mainly due to lack of earthquakes, that would produce PcP waves that sample the D" under north America. We considered this problem by removing all PKP paths from south Atlantic to Alaska (90 paths total after declustering) and performed the inversion for the remaining dataset (including polar paths). The model we obtain this way (TRH_KCnsa, Figure 3.11 (c)) is very similar to model TRH_KC, with the only difference in the amplitude of the low velocity region under north America. However, the fast anomaly under South Sandwich Island region still remains after the exclusion of these specific paths.

Note that the low velocities obtained southeast of south America and adjacent to high velocities in the southernmost Atlantic, are consistently present in Figures 3.11 (a, c), and in good agreement with the PcP-P residuals map in Figure 3.4. They do not depend on the inclusion of the very anomalous south Atlantic to Alaska paths. In Figure 3.11 (b), on the other hand, the same pattern is still visible, but with somewhat weaker amplitude. Only the low velocities under the Canadian Shield are clearly dependent on the inclusion of South Atlantic to Alaska paths. Figure 3.4 does seem to indicate, however, that PcP-P senses some low velocities, where there is coverage.

Using our irregular-size cell algorithm, we inverted the PKP(AB-DF) dataset without the polar paths, with and without including PcP-P data and obtained very similar models as in the regular block size inversion (coefficients of correlation = 0.94, 0.94, respectively).

3.6.1 Fits to the data

Figure 3.12 (a) shows variance reduction in PKP(AB-DF) data as a function of varying damping factors, by combining KH2001m with various D" models as defined in Table 3.2. There is a direct trade-off between variance reduction and the level of P velocity heterogeneity in D". As the damping factor grows, the percentage of blocks with P velocity perturbation exceeding ±1% drops, as illustrated in Figure 3.12 (b). It can been seen that

TRH_KC model at optimal damping has ≈ 15% of blocks exceeding ±1%. The value of the maximum amplitude of anomalies for optimal damping in TRH_KC model is ±2.2%. Without other geophysical constraints on the strength of heterogeneity in the lowermost mantle, it is very difficult to estimate the appropriate damping to be applied from these curves. However, we can use our PKP(BC-DF) dataset, not used in the inversion process, to constrain damping, by estimating which value of damping provides the model which best fits this dataset.

In Figure 3.13, we show variance reductions, as a function of the damping parameter chosen, for the complete PKP(BC-DF) dataset, calculated by combining predictions from D" models (Table 3.2) with KH2001m. Figure 3.13 shows that the best fits to the complete PKP(BC-DF) dataset are achieved for the models constructed using the complete PKP(AB-DF) dataset, and that an optimum damping parameter around $2.5x10^5$ to $5x10^5$ is clearly defined. This damping parameter is chosen for the final model TRH_KC shown in Figure 3.10 (a) and Figure 3.11 (a). Models TRH_K and TRH_KC provide the best fit and explain about 27% of the variance in PKP(BC-DF). Given how close the BC and DF legs are in D", for any given path, it is remarkable that such a large portion of the variance in PKP(BC-DF) can be explained by our relatively coarsely parametrized models.

Next, we examine observed and predicted residuals for models obtained using PKP(AB-DF) and PcP-P data, and the respective optimal damping parameters. We show a comparison of the observed and predicted residuals as a function of angle ξ for TRH_KC, TRH_KCeq and TRH_KCnsa in Figure 3.14 (a), (b) and (c) respectively. The cluster of very large observed residuals that is not completely explained by our models corresponds to very specific paths from south Atlantic to Alaska and south Atlantic to northern Asia (mostly for the event in south Atlantic mentioned earlier). However, between $\xi = 20^o$ and $\xi = 45^o$, model TRH_KC is able to explain a range of 6 seconds. It also successfully explains the larger scatter of "equatorial" data as opposed to "polar" data. Figure 3.14 (d) shows the predictions of model TRH_KCa combined with the corresponding inner core anisotropy model and with KH2001a. Figure 3.14 (e) shows, for reference the predictions of the inner core anisotropy model alone. The variance reduction in the PKP(AB-DF) dataset is only 17.6% when only inner core anisotropy is considered, and the distribution of the predictions does not match that of the data. Combining inner core anisotropy with TRH_KCa and

KH2001m, we obtain a variance reduction of 82.4%, a value which is slightly less than for model TRH_KC (with KH2001m, Figure 3.14 (a)). However, some polar data at angles $\xi < 30^o$ are explained slightly better.

Figures 3.15 (a), (b), and (c) show the predictions for PcP-P residuals, obtained by using model KH2001m, combined with models TRH_KC, TRH_KCeq and TRH_KCnsa, respectively. More than 50% of the variance in PcP-P can be explained by any of the models, which indicates that 1) a significant portion of the variance in PcP-P is attributable to D", as previously inferred from Figure 3.6 and 2) the inclusion of polar paths is not incompatible with the constraints from PcP-P.

Finally, we analyze the fits to the PKP(BC-DF) dataset obtained for the different models. Figure 3.16 (a) shows the PKP(BC-DF) observed and predicted residuals as a function of ξ for model TRH_KC (with KH2001m). The scatter in equatorial paths is well explained, however, this model does not explain the large residuals for polar paths. Figure 3.16 (b) shows the predictions of the inner core anisotropy model alone. This model does not explain the scatter in the equatorial data, but it explaining the larger residuals on polar paths better, resulting in an overall variance reduction of 44.2%, compared to only 27% for model TRH_KC. The combination of inner core anisotropy model, corresponding D" model TRH_KCa and KH2001m results in a slight improvement in variance reduction (54.5%, Figure 3.16 (c)). Adding the D" model helps explain more of the scatter on equatorial paths. Still, a large portion, at least 2 second differential travel time of the most anomalous data near $\xi = 30^o$ remains unexplained.

3.7 Discussion and conclusions

We inverted a large dataset of hand-picked PKP(AB-DF) and PcP-P travel time data to retrieve the P velocity structure of the lowermost 300 km of the mantle, after correcting for overlying mantle structure, using the tomographic P model , stripped of the last 300 km of the mantle, that provides the best fit to both datasets (KH2001m). We demonstrated that the exclusion or inclusion of polar paths doesn't change the derived P velocity model of D" significantly, except in areas where coverage is provided only when polar paths are included (mostly north America).

Our results demonstrate that, with a significant number of high quality PKP differential travel time data, we are able to retrieve D" maps that are compatible with maps obtained using independent body wave datasets. The combination of our preferred D" model and KH2001m can explain over 80% of the variance in PKP(AB-DF) and over 50% of the variance in PcP-P, as well as a significant portion of the variance (close to 30%) which was in our PKP(BC-DF) dataset, not used in the inversion.

We showed that accounting for a radial model of inner core anisotropy, compatible with normal mode splitting data, prior to inversion, produces a model of D" that is very similar to the models for which inner core anisotropy is not included, although with smaller amplitudes of lateral variations. Such a model, combined with KH2001m, results in better predictions of PKP(BC-DF), but slightly degrades predictions of PKP(AB-DF) residuals. There remains a significant portion of the PKP(BC-DF) residuals on anomalous paths between the south Atlantic and Alaska, that this type of model, combining simple, axisymmetric anisotropy in the inner core and D" heterogeneity at intermediate wavelengths, cannot explain.

In areas of good coverage, our models TRH_KC and TRH_KCa provide stable and reliable maps of lateral variations of velocity in D" at the scale length of several hundred km. The next step is, on the one hand, to improve the coverage by incorporating other independent data such as Pdiff-PKP at appropriate distance ranges, and, on the other, to examine short scale variations in D" structure as can be addressed using dense arrays such as that in Alaska. This will be addressed in forthcoming contributions.

In the present study, we also have ignored possible contributions from core-mantle boundary topography, which could possibly further improve the fits to our datasets (e.g. [*Creager and Jordan*, 1986; *Rodgers and Wahr*, 1993; *Obayashi and Fukao*, 1997]).

Although measuring differential travel time data has a lot of advantages, as their usage minimizes uncertainties in the source and receiver effects, absolute travel time measurements are also a very useful source of information due to limited data coverage. In a related study [*Romanowicz et al.*, 2001], we analyzed short period data recorded at Alaskan stations, and found that there exist similar trends in absolute travel times in both PKP(DF) and PKP(BC), so that at least one part of the signal must come from the mantle, and thus not originate from the inner core as previously suggested.

3.8 Acknowledgements

We thank two anonymous reviewers who helped us to improve the manuscript. We are grateful to Ludovic Bréger for his helpful comments, and numerous colleagues at UC Berkeley for their suggestions. We thank Ken Creager, Tom McSweeney, Annie Souriau, Satoru Tanaka and Michael Wysession, for generously providing their data, and also to Roger Hansen, Kent Lindquist, Doug Christensen and personel of UAF Geophysical Institute, Bill Shannon, Sylvia Lehman and Luc Saumure from CNSN, and Fumiko Tajima from UCB. Many thanks to IRIS, Geoscope, GRSN, Mednet and BDSN teams. Figures were made with the General Mapping Tools (P. Wessel and W. H. F. Smith, *EOS Trans. AGU* **76**, 329, (1995)). This work was supported by NSF grant no. EAR-9902777 and IGPP/LLNL grant no. 00-GS-010. It is BSL contribution 01-05.

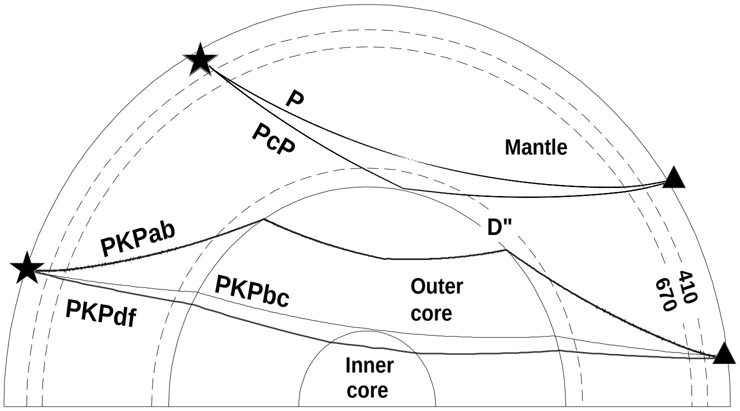

Figure 3.1. Cross-section of Earth showing the paths of P, PcP, PKPdf, PKPbc and PKPab body waves.

Figure 3.2. **(a)** The declustered subsets of PKP(AB-DF) differential travel time residuals used in this study. Different symbols, corresponding to data from different analysts are explained in the legend. Residuals are calculated with respect to the ak135 model and plotted with respect to the angle ξ between the PKP(DF) leg in the inner core and the rotation axis of Earth. Standard ellipticity corrections were applied. All earthquake locations and origin times are corrected with respect to the relocation catalog of [*Engdahl et al.*, 1998]. Some specific polar paths are indicated by numbers as follows: 1) Svalbard Sea to SPA; 2) 63N,143W to SPA; 3) 79N,124E to SPA; 4) 67N,173W to SPA; 5) 60N,153W to SPA; 6) mid-Atlantic ridge to Alaska; 7) South Sandwich Islands to COL; 8) South Sandwich Islands to BILL; 9) South Sandwich Islands to SEY; 10) southeast Pacific to NRIL; 11) South Sandwich Islands to COL and NRIL; 12) mid-Atlantic ridge to Alaska; 13) south of New Zealand to FRB; 14) Bouvet Islands to COLA and INK; 15) Aleutian Islands to SYO; 16) Sea of Okhotsk to SYO; 17) south of New Zealand to KBS; 18) various locations to SYO; 19) and 20) Aleutian Islands to SYO. **(b)** Same as (a), where circles and pluses correspond to paths for which PKP(DF) bottoms in the quasi-western and quasi-eastern hemisphere, respectively, as defined by [*Tanaka and Hamaguchi*, 1997].

a)

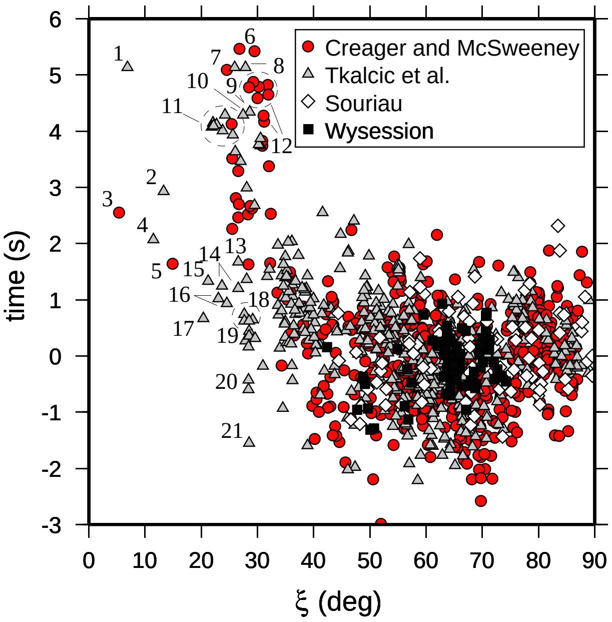
Creager and McSweeney
Tkalcic et al.
Souriau
Wysession
time (s)
ξ (deg)
6
5
4
3
2
1
0
-1
-2
-3
0
10
20
30
40
50
60
70
80
90
1
2
3
4
5
6
7
8
9
10
11
12
13
14
15
16
17
18
19
20
21

b)

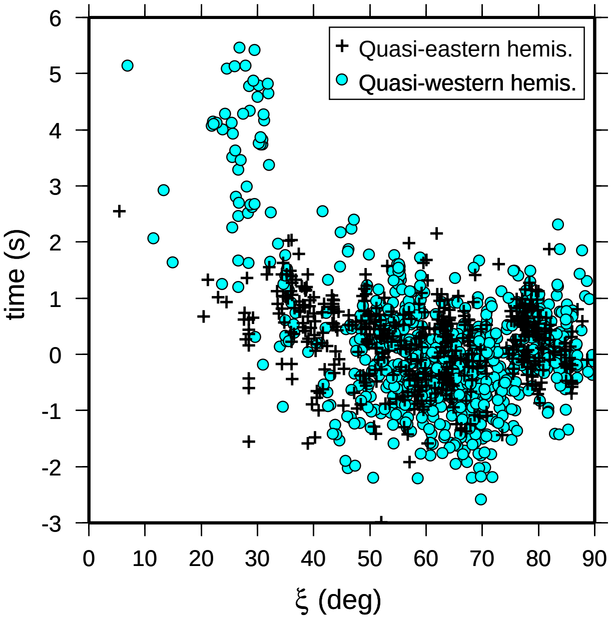
Quasi-eastern hemis.
Quasi-western hemis.
time (s)
ξ (deg)
6
5
4
3
2
1
0
-1
-2
-3
0
10
20
30
40
50
60
70
80
90

Figure 3.3. **(a)** The declustered subsets of PKP(BC-DF) differential travel time residuals used in this study. Different symbols, corresponding to data from different analysts are explained in the legend. Some specific polar paths are indicated by numbers as follows: 1) Novaya Zemlya to SNA; 2) Alaska to SPA; 3) South Sandwich Islands to MBC; 4) Alaska and north Canada to SPA; 5) South Sandwich Islands to northeast Asia and Alaska; 6) 52S,140E to NOR; 7) Siber to SBA; 8) 53S,160E to NOR; 9) 62N,154E, 64N,125E and 60N,169E to SPA; 10) 60N,153W to SPA; 11) various locations to SYO; 12) south of Australia to NOR. **(b)** Same as (a), where now circles and pluses correspond to paths with PKP(DF) bottoming in the quasi-western and quasi-eastern hemisphere, respectively.

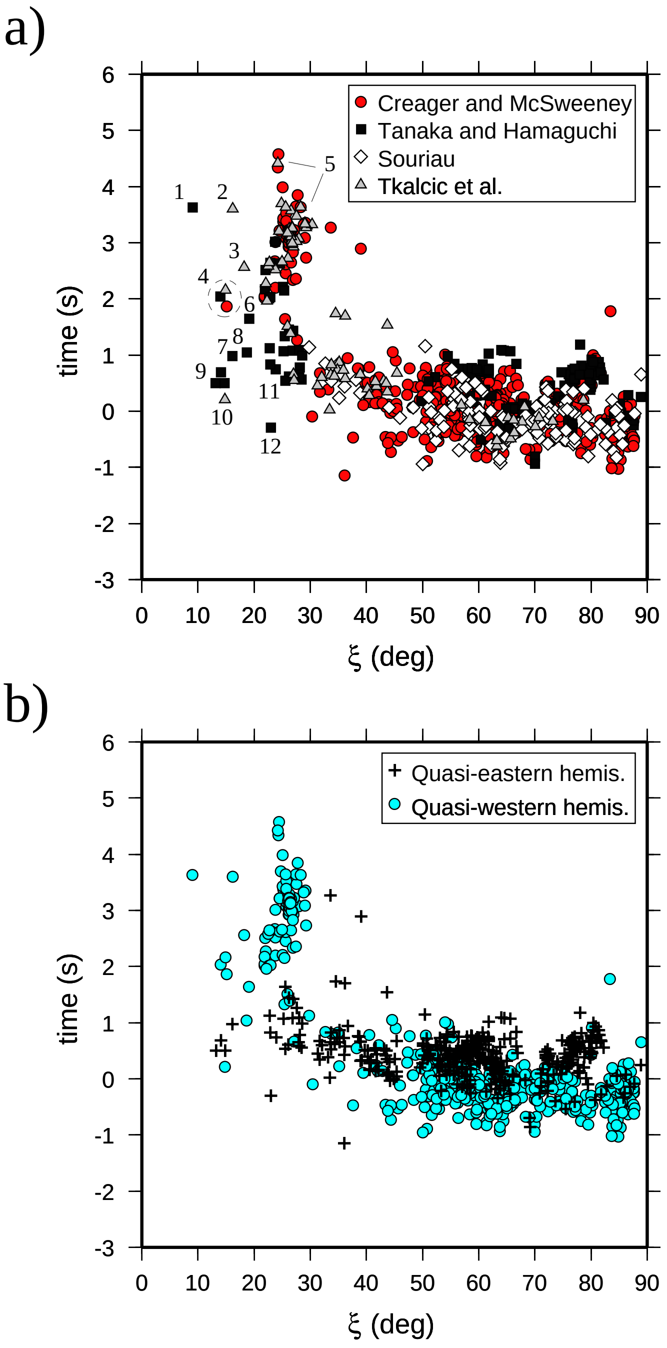
a)
Creager and McSweeney
Tanaka and Hamaguchi
Souriau
Tkalcic et al.
1
2
3
4
5
6
7
8
9
10
11
12
time (s)
ξ (deg)
6
5
4
3
2
1
0
-1
-2
-3
0
10
20
30
40
50
60
70
80
90
b)
Quasi-eastern hemis.
Quasi-western hemis.
time (s)
ξ (deg)

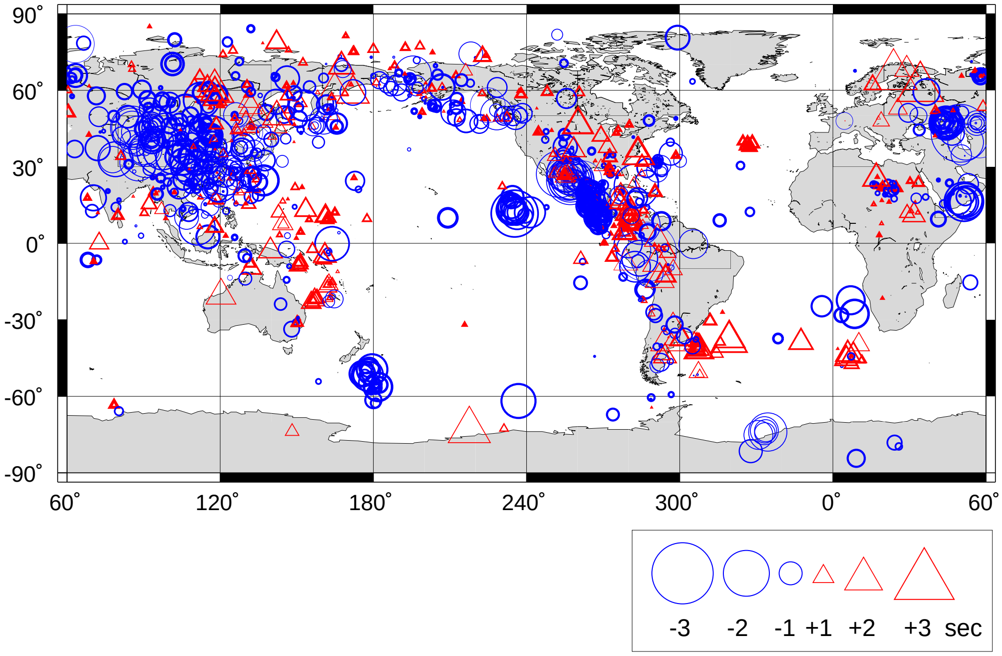

Figure 3.4. PcP-P travel time residuals plotted at the surface projections of PcP bouncing points. Triangles and circles indicate positive and negative residuals, respectively. The size of the symbol represents the value of the residual, the thickness of symbol lines scales with epicentral distance of the measurement: the thicker the line, the larger the epicentral distance. The largest symbols represent a travel-time anomaly of 2.8 seconds.

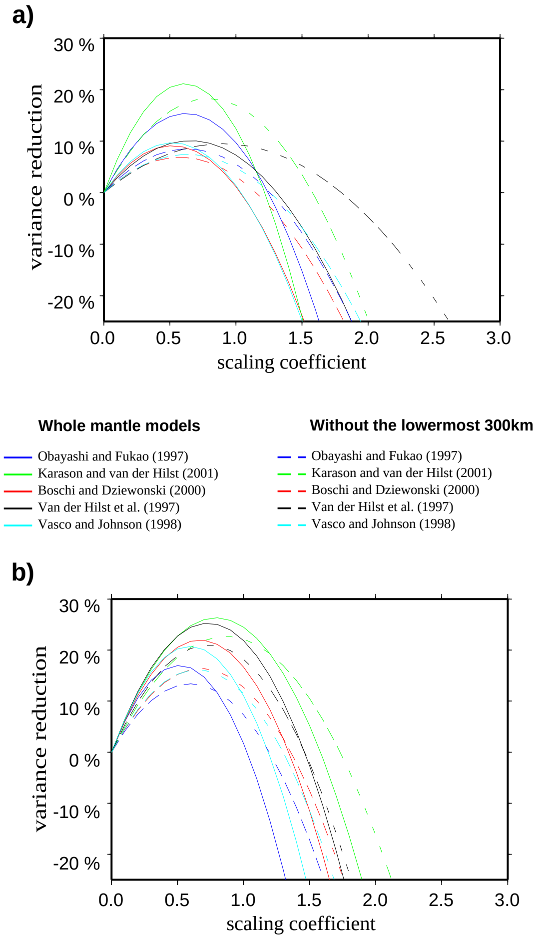

Figure 3.5. **(a)** Variance reduction in PKP(AB-DF) data as a function of scaling coefficient h, as defined in text, for various P models, for the whole mantle (solid lines) and for the whole mantle stripped of D"(dashed lines); **(b)** Same as (a), for the PcP-P dataset.

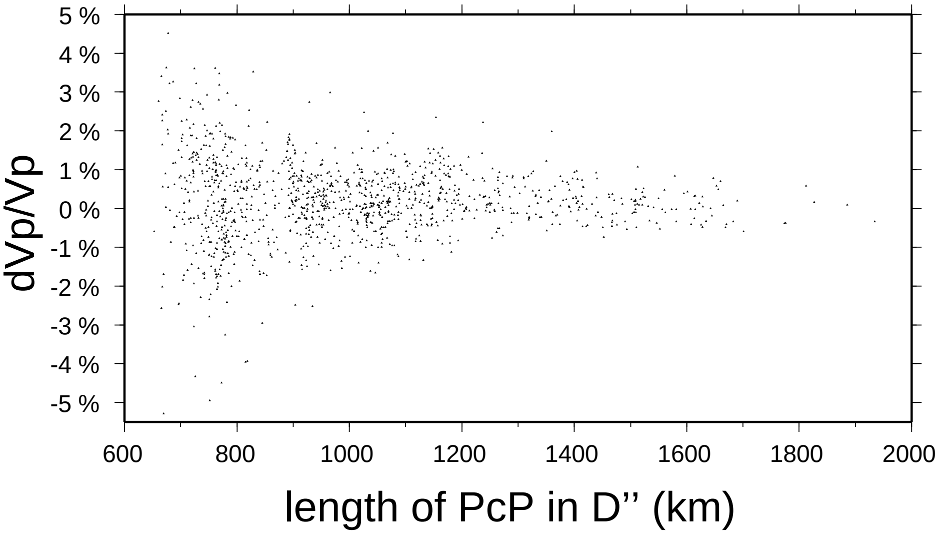

Figure 3.6. Average relative velocity variations in the lowermost 300 km of the mantle needed to explain PcP-P residuals, as a function of the length of PcP leg in the same layer. Mantle corrections are taken into account (from [*Kárason and Hilst*, 2001].

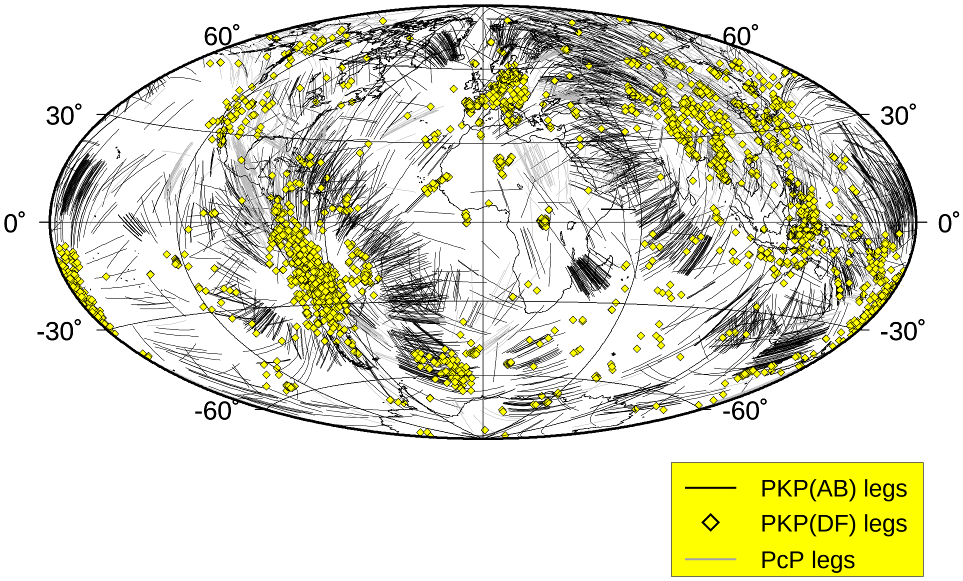

Figure 3.7. Surface projections of PKP(AB) and PcP legs sampling the lowermost 300 km of the mantle. Diamonds represent penetration points of PKP(DF) into the core (their legs sampling the lowermost 300 km of the mantle would projects as points since they traverse that layer at almost vertical incidence).

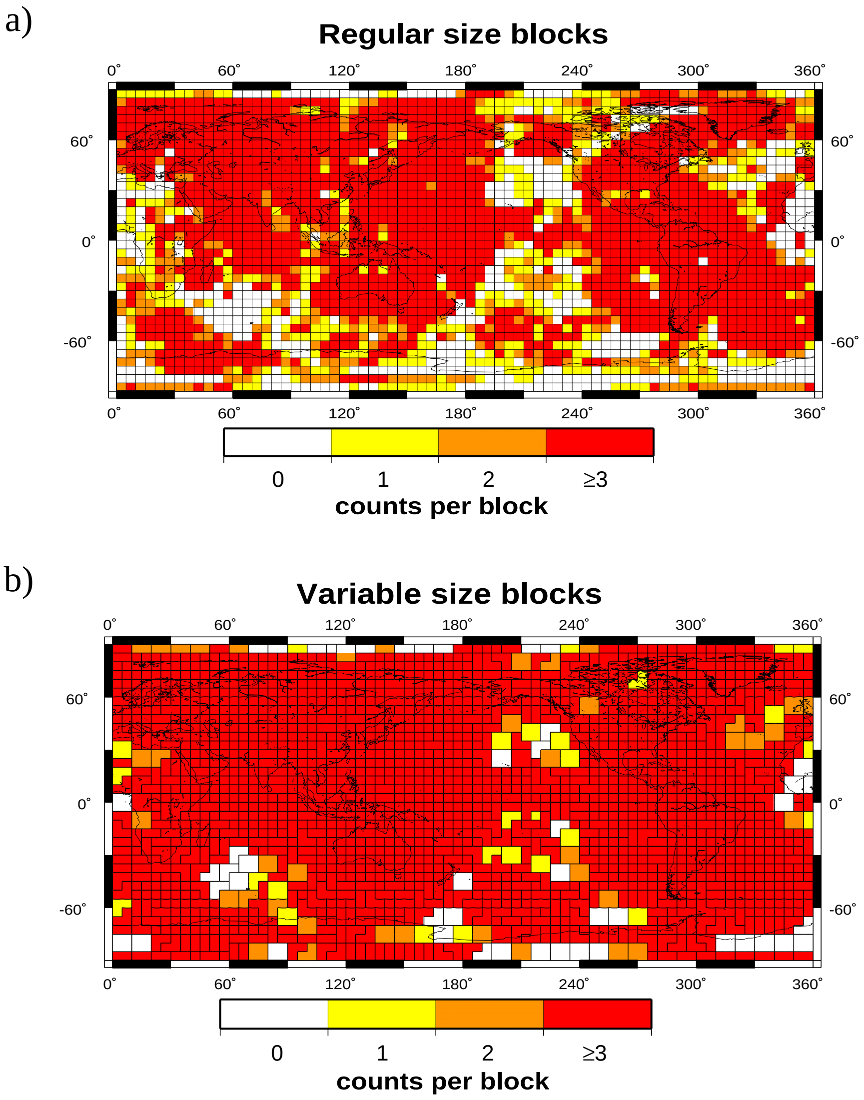

Figure 3.8. The sampling of D" in terms of number of counts per block (number of rays crossing each particular block: **(a)** before the variable-size block algorithm is applied; **(b)** after the variable-size block algorithm is applied. The critical number of counts per block is set to be 3 in this example. White areas represent blocks that have been rejected because of insufficient sampling. Note that in (b), blocks have changed shape and increased their size in areas of poor sampling and remain small in well-sampled areas.

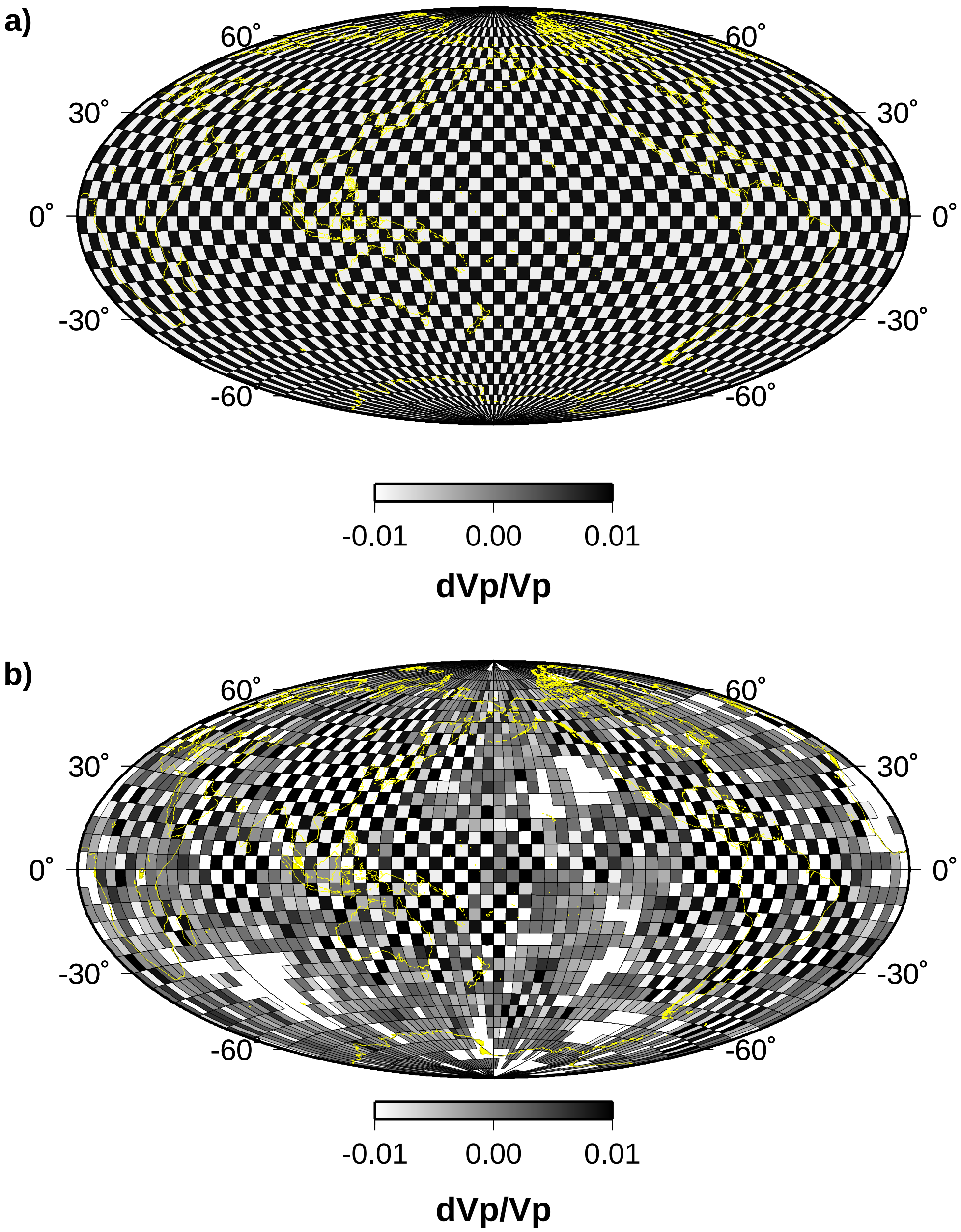

Figure 3.9. **(a)** The synthetic checker-board input model, parametrized in terms of equiangular cells of size 5x5^o (same as in inversion); **(b)** The corresponding output model, for the optimal damping. White non-gridded areas are non-sampled blocks.

Figure 3.10. Models **(a)** TRH_KC and **(b)** TRH_KCa, for the optimal damping. These one layered models represent P velocity perturbations with respect to model ak135 in the bottom 300 km of the mantle. TRH_KC was obtained by inverting PKP(AB-DF) and PcP-P data simultaneously, without inner core anisotropy. For TRH_KCa, the same dataset was inverted, but first corrected for the transverse isotropy model of [*Tromp*, 1995]. Blackened areas represent non-sampled regions.

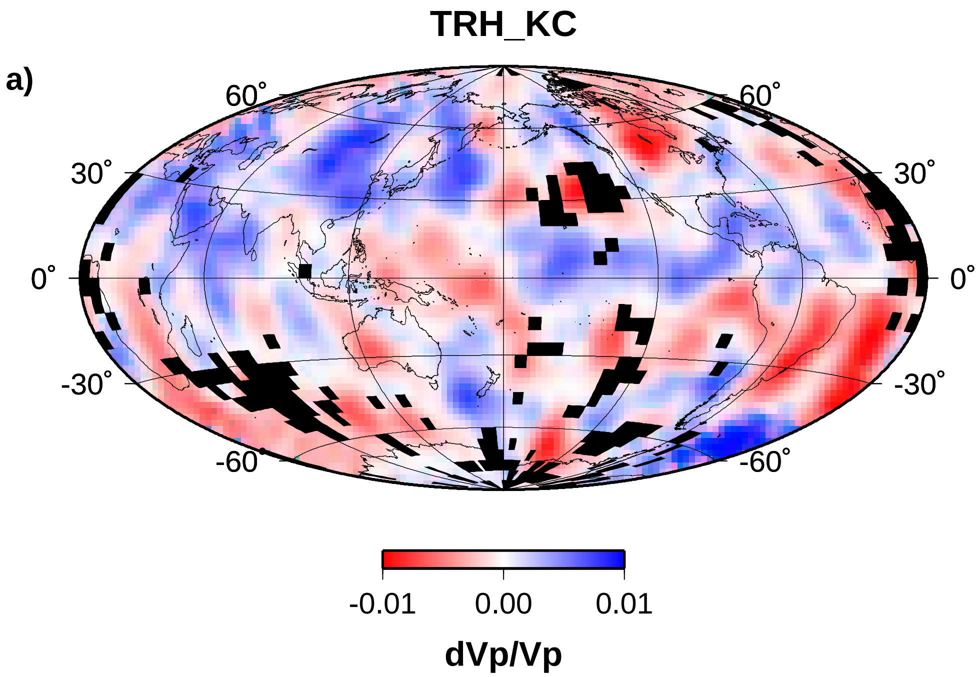
TRH_KC
a)
60°
30°
0°
-30°
-60°
60°
30°
0°
-30°
-60°
-0.01
0.00
0.01
dVp/Vp

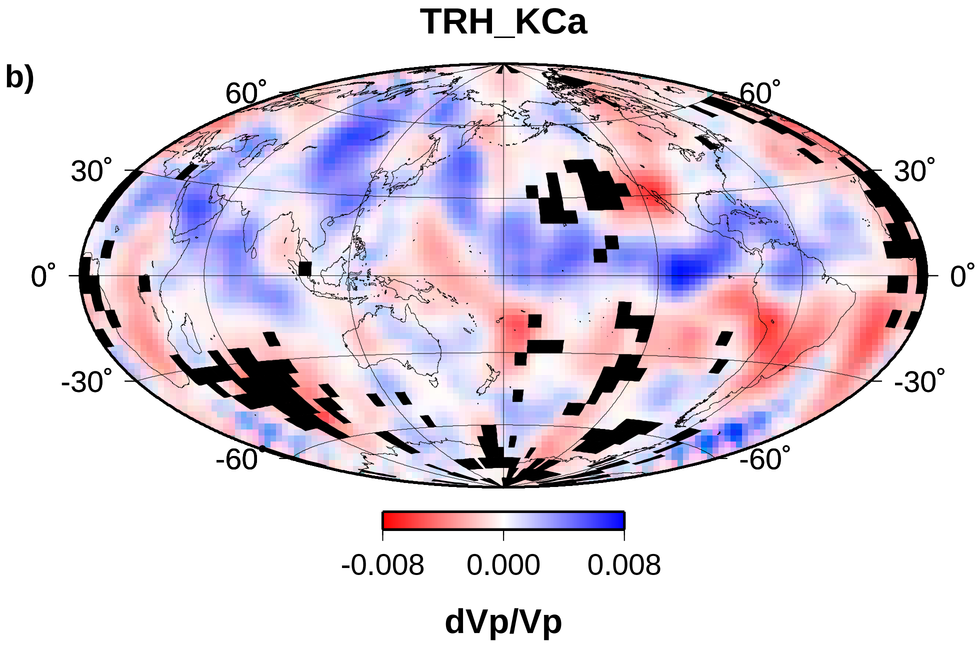
TRH_KCa
b)
60°
30°
0°
-30°
-60°
60°
30°
0°
-30°
-60°
-0.008
0.000
0.008
dVp/Vp

Figure 3.11. One layer models of P-wave velocity perturbations in the lowermost 300 km of the mantle, obtained from different combinations of data, as described in Table 2: **(a)** TRH_KC; **(b)** TRH_KCeq; **(c)** TRH_KCnsa. The models are here shown in polar projections centered on the south pole (left) and north pole (right).

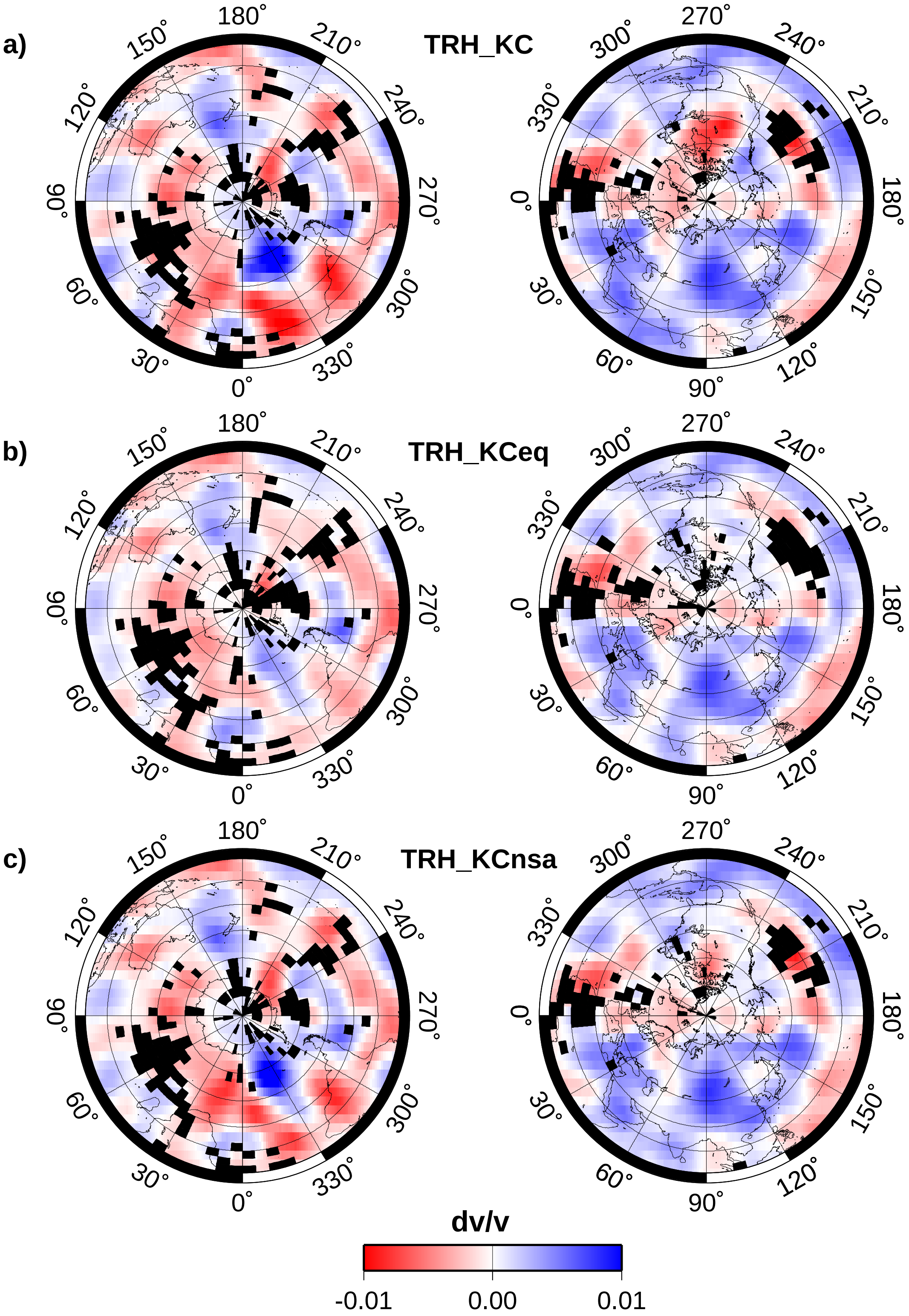
a)
TRH_KC
b)
TRH_KCeq
c)
TRH_KCnsa
180°
210°
240°
270°
300°
330°
0°
30°
60°
90°
120°
150°
dv/v
-0.01
0.00
0.01

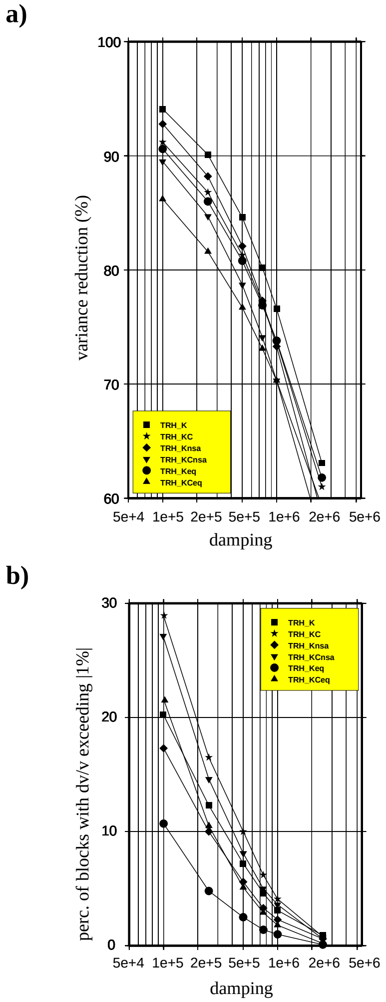

Figure 3.12. **(a)** Variance reduction in various PKP(AB-DF) datasets from Table 2 calculated from corresponding models of the lowermost 300 km of the mantle (indicated by different symbols in figure as explained in the legend), plotted as a function of damping parameter. Residuals are corrected for the KH2001m model above the lowermost 300 km of the mantle. Appropriate weighting is applied for the paths with similar geometry in calculating variance reduction, as explained in the text; **(b)** the percentage of blocks with perturbations exceeding ±1% for the same models as in (a).

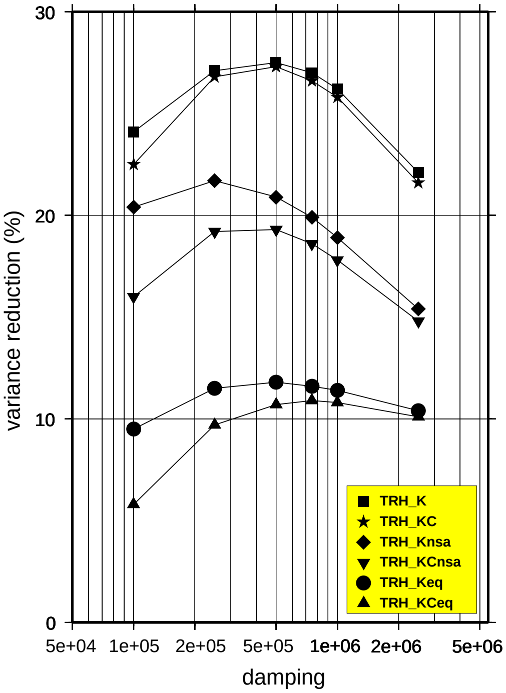

Figure 3.13. Variance reduction in the complete PKP(BC-DF) dataset obtained for models TRH_K and TRH_KC (indicated by different symbols in figure), plotted as a function of damping parameter. Residuals are corrected for the KH2001m model above the lowermost 300 km of the mantle. Appropriate weighting is applied for the paths with similar geometry in calculating variance reduction as explained in the text.

Figure 3.14. Observed versus predicted PKP(AB-DF) residuals, plotted as a function of ξ for: **(a)** TRH_KC; **(b)** TRH_KCeq; **(c)** TRH_KCnsa; **(d)** TRH_KCa; **(e)** The inner core anisotropy model TR95 used in the derivation of TRH_KCa. The predictions include the contribution of KH2001m. In (d), the predictions also include the contribution of TR95 shown in (e).

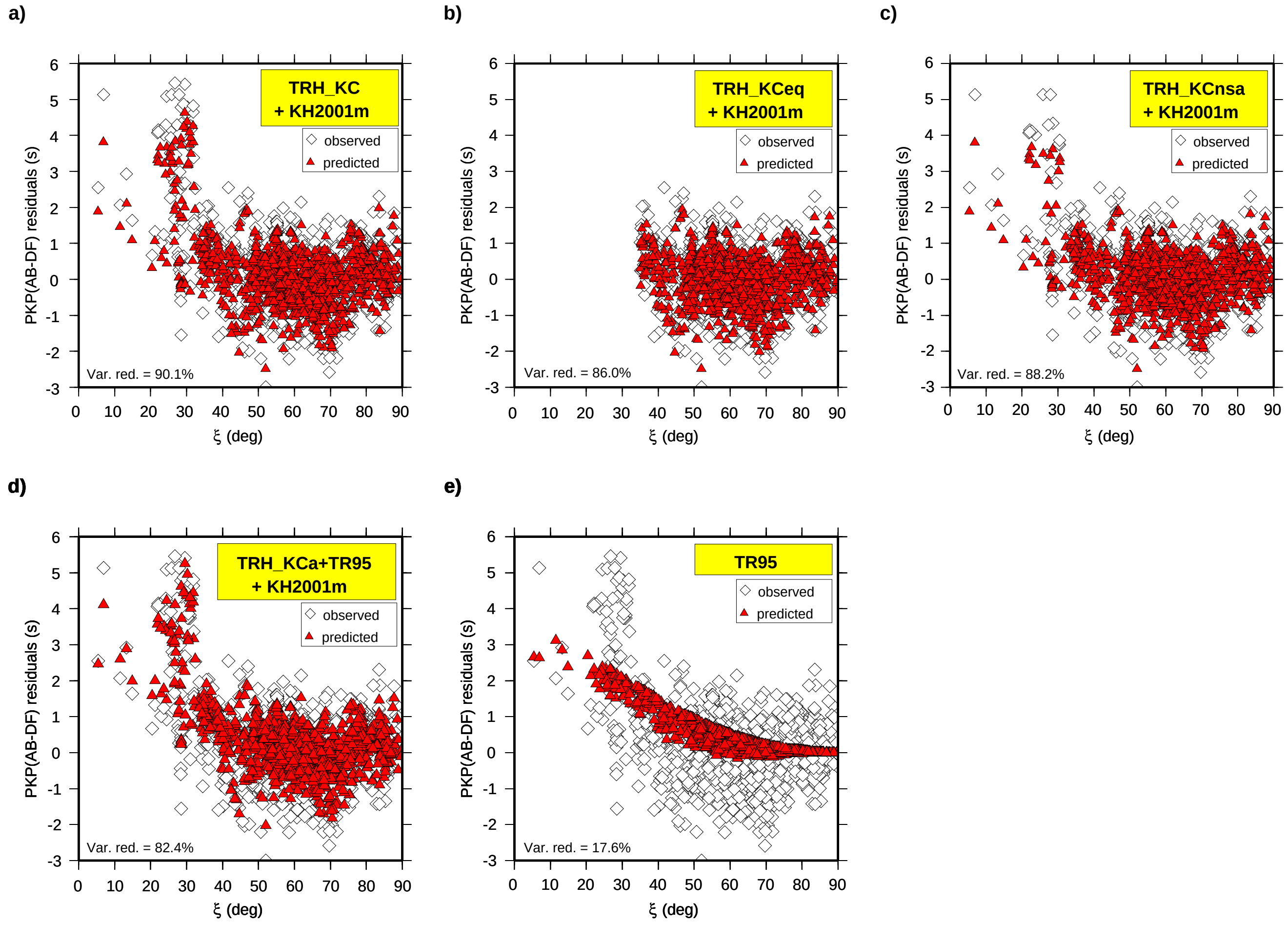
a)
TRH_KC
+ KH2001m
observed
predicted
Var. red. = 90.1%
b)
TRH_KCeq
+ KH2001m
observed
predicted
Var. red. = 86.0%
c)
TRH_KCnsa
+ KH2001m
observed
predicted
Var. red. = 88.2%
d)
TRH_KCa+TR95
+ KH2001m
observed
predicted
Var. red. = 82.4%
e)
TR95
observed
predicted
Var. red. = 17.6%
PKP(AB-DF) residuals (s)
ξ (deg)
6
5
4
3
2
1
0
-1
-2
-3
0
10
20
30
40
50
60
70
80
90

Figure 3.15. Observed versus predicted PcP-P residuals for: **(a)** TRH_KC; **(b)** TRH_KCeq; **(c)** TRH_KCnsa. The predictions include the contribution of KH2001m. Variance reduction and correlation coefficients are indicated. Solid line is the best linear fit.

a)

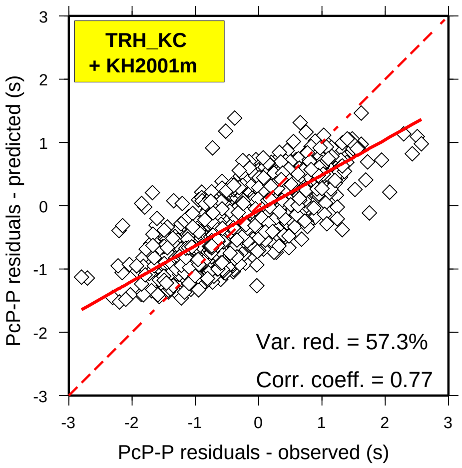
TRH_KC
+ KH2001m
Var. red. = 57.3%
Corr. coeff. = 0.77
PcP-P residuals - predicted (s)
PcP-P residuals - observed (s)
3
2
1
0
-1
-2
-3
-3
-2
-1
0
1
2
3

b)

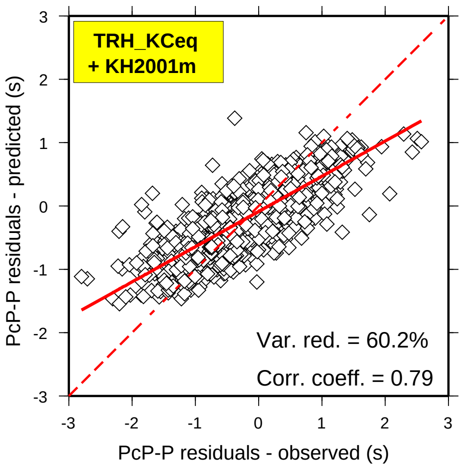
TRH_KCeq
+ KH2001m
Var. red. = 60.2%
Corr. coeff. = 0.79
PcP-P residuals - predicted (s)
PcP-P residuals - observed (s)
3
2
1
0
-1
-2
-3
-3
-2
-1
0
1
2
3

c)

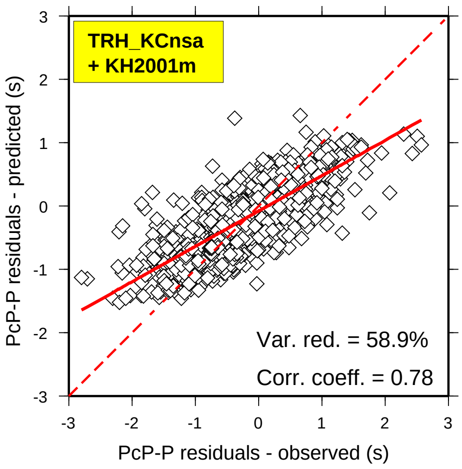
TRH_KCnsa
+ KH2001m
Var. red. = 58.9%
Corr. coeff. = 0.78
PcP-P residuals - predicted (s)
PcP-P residuals - observed (s)
3
2
1
0
-1
-2
-3
-3
-2
-1
0
1
2
3

Figure 3.16. Observed (diamonds) versus predicted (triangles) PKP(BC-DF) residuals as a function of ξ for: **(a)** model TRH_KC combined with KH2001m; **(b)** radial model of inner core anisotropy (TR95); **(c)** model TRH_KCa, combined with KH2001m and TR95.

a)

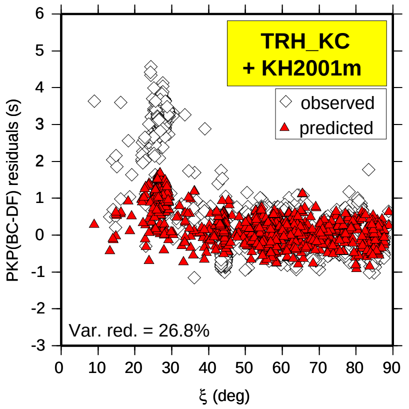
TRH_KC
+ KH2001m
observed
predicted
Var. red. = 26.8%
PKP(BC-DF) residuals (s)
6
5
4
3
2
1
0
-1
-2
-3
0
10
20
30
40
50
60
70
80
90
ξ (deg)

b)

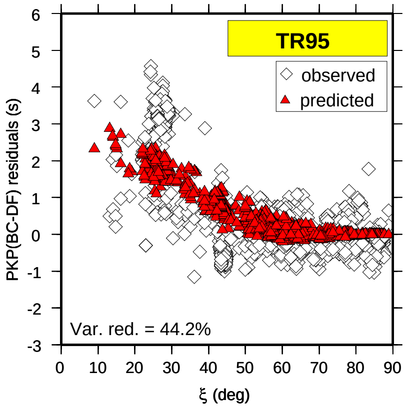
TR95
observed
predicted
Var. red. = 44.2%
PKP(BC-DF) residuals (s)
6
5
4
3
2
1
0
-1
-2
-3
0
10
20
30
40
50
60
70
80
90
ξ (deg)

c)

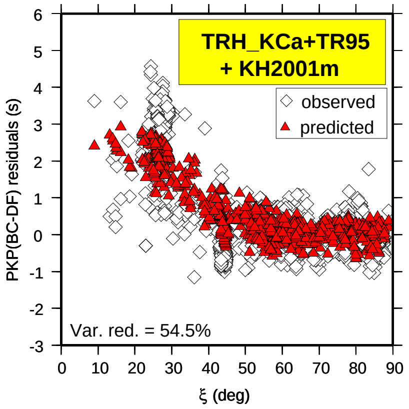
TRH_KCa+TR95
+ KH2001m
observed
predicted
Var. red. = 54.5%
PKP(BC-DF) residuals (s)
6
5
4
3
2
1
0
-1
-2
-3
0
10
20
30
40
50
60
70
80
90
ξ (deg)

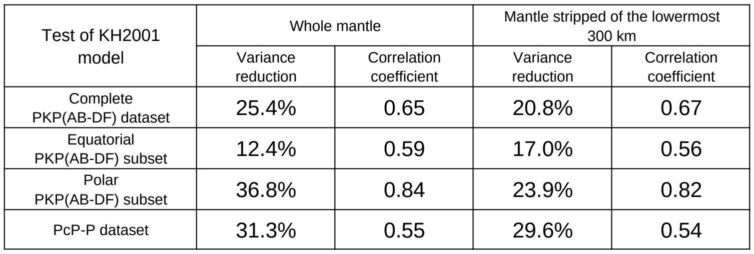

Test of KH2001 model	Whole mantle		Mantle stripped of the lowermost 300 km	
	Variance reduction	Correlation coefficient	Variance reduction	Correlation coefficient
Complete PKP(AB-DF) dataset	25.4%	0.65	20.8%	0.67
Equatorial PKP(AB-DF) subset	12.4%	0.59	17.0%	0.56
Polar PKP(AB-DF) subset	36.8%	0.84	23.9%	0.82
PcP-P dataset	31.3%	0.55	29.6%	0.54

Table 3.1. Variance reductions and correlation coefficients between observed and predicted subsets of data used in this study (after weighting was applied on the paths with similar geometry through the mantle). First and second columns refer to the whole mantle model by *Kárason and van der Hilst* (2001), referred as KH2001 in the text, while third and fourth columns refer to the same model stripped of the lowermost 300 km (KH2001m).

Model	Data description
TRH_K	Data: complete PKP(AB-DF) dataset Corrected for: KH2001m before inversion
TRH_Keq	Data: "Equatorial" subset of PKP(AB-DF) (paths with ξ > 35°) Corrected for: KH2001m before inversion
TRH_Knsa	Data: PKP(AB-DF) without subset of paths from south Atlantic to Alaska Corrected for: KH2001m before inversion
TRH_KC	Data: complete PKP(AB-DF) dataset.+ PcP-P dataset Corrected for: KH2001m before inversion
TRH_KCeq	Data: "Equatorial" subset of PKP(AB-DF) (paths with ξ > 35˚) + PcP-P dataset Corrected for: KH2001m before inversion
TRH_KCnsa	Data: PKP(AB-DF) without subset of paths from south Atlantic to Alaska + PcP-P dataset Corrected for: KH2001m before inversion
TRH_KCa	Data: complete PKP(AB-DF) dataset.+ PcP-P dataset Corrected for: KH2001m and TR95 before inversion

Table 3.2. Description of models and datasets used in their construction. It is also indicated which corrections are applied to data before the inversion.

Correlation coefficient	TRH_K	TRH_Keq	TRH_Knsa	TRH_KC	TRH_KCeq	TRH_KCnsa	TRH_KCa
TRH_K	1.00	0.65	0.89	0.83	0.47	0.71	0.58
TRH_Keq	0.65	1.00	0.76	0.52	0.68	0.57	0.50
TRH_Knsa	0.89	0.76	1.00	0.77	0.56	0.81	0.55
TRH_KC	0.83	0.52	0.77	1.00	0.76	0.93	0.71
TRH_KCeq	0.47	0.68	0.56	0.76	1.00	0.83	0.68
TRH_KCnsa	0.71	0.57	0.81	0.93	0.83	1.00	0.68
TRH_KCa	0.58	0.50	0.55	0.71	0.68	0.68	1.00

Table 3.3. Correlation coefficient between various combinations of one-layered models of D” obtained in this study.

Chapter 4

Short scale heterogeneity in the lowermost mantle: insights from PcP-P and ScS-S data

This chapter is a modified version of a submitted manuscript to *EPSL*, [*Tkalčić and Romanowicz*, 2001].

4.1 Abstract

We compare lateral variations at the base of the mantle as inferred from a global dataset of PcP-P travel time residuals, measured on broadband records, and existing P and S tomographic velocity models, as well as ScS-S travel time data in some selected regions. In many regions, the PcP-P dataset implies short scale lateral variations that are not resolved by global tomographic models, except under eastern Eurasia, where data and models describe a broad region of fast velocity anomalies across which variations appear to be of thermal origin. In other regions, such as central America and southeastern Africa, correlated short scale (several hundred kilometers) lateral variations are observed in PcP and ScS, implying large but not excessive values for the ratio $R = \partial lnV_s/\partial lnV_p$ ($\sim$ 2.5). On the other hand, in at least two instances, in the heart of the African Plume and on the edge of the Pacific Plume, variations in P and S velocities appear to be incompatible,

implying strong lateral gradients across compositionally different domains, possibly also involving topography on the core-mantle boundary. One should be cautious in estimating R at the base of the mantle from global datasets, as different smoothing and sampling of P and S datasets may result in strong biases and meaningless results.

4.2 Introduction and Motivation

An important question in global geodynamics is whether the 3D seismic velocity anomalies, as seen in tomographic models of the mantle, are of a thermal or a compositional nature, or a combination of both. Traditionally, the parameter $R = \partial lnV_s/\partial lnV_p$ has been used to describe the relation between compressional and shear velocity anomalies in the mantle. However, there has been a discrepancy between the results of mineral physics and seismology.

[*Dziewonski et al.*, 1986] pointed out that P and S velocity perturbations in the lower mantle are correlated with the factor of proportionality $R = 2.0 - 2.5$. [*Bokelmann and Silver*, 1991] estimated R increasing from the values of 1.7 in the upper mantle to values greater than 2 in the lower mantle under Carribean. [*Robertson and Woodhouse*, 1996], after a joint inversion of P and S waves data, reported that P and S velocity models are highly correlated to depths of 2000 km in the mantle, and that R increases from 1.7 in the top of the lower mantle to 2.6 at the depth about 2000 km. They also pointed out the importance of simultaneous inversion of P and S data, measured at the similar periods and with the similar coverage, as heterogeneities within the Earth may be frequency dependent. Their result indicated that the contribution from the bulk modulus in the lower mantle is not very large; as the variation in compressional velocity is a combination of the variation in shear and bulk sound velocities. This motivated a new suite of studies, with the focus on simultaneous inversion for shear and bulk sound velocity anomalies (e.g. [*Su and Dziewonski*, 1997; *Kennett et al.*, 1998; *Ishii and Tromp*, 1999; *Masters et al.*, 1999]). Such studies are very insightful, because bulk sound velocity anomalies can be easily compared with the high pressure and temperature laboratory experiments' results. Above mentioned studies are all in agreement that there is an anti-correlation between shear and acoustic velocity perturbations throughout the lower mantle; and that P and S velocity anomalies are generally well correlated throughout the mantle, although with some differences. For instance, [*Kennett et al.*, 1998] found a disjunction between acoustic and shear velocity anomalies below 2000 km and ascribed it to the presence of compositional heterogeneities. They also found a constant value of $R \approx 2.1$ in the lower mantle. [*Su and Dziewonski*, 1997] and [*Masters et al.*, 1999] found anti-correlated acoustic and shear wave velocity anomalies all the way down to CMB, but they reported R increasing to above 3.0 and to about 2.5 at CMB, for the two studies, respectively. Considering long wavelengths, [*Romanowicz*, 2001] found that R in general increases above the value of 3.0 in the lower mantle, but decreases again near CMB.

On the other hand, in a mineral physics study, [*Karato*, 1993b] estimated, using the data for olivine, that R values would reach 1.8 for $Q_\mu = 50$ throughout the mantle. He pointed out that the effect of anelasticity is important in the Earth's mantle, particularly for shear waves. [*Agnon and Bukowinski*, 1990] and [*Isaak et al.*, 1976] showed that the value of 2.0-2.5 for R at the lower mantle pressures can be derived assuming thermal effects only, without necessity for invoking partial melt. However, such values are still too low to cause acoustic and shear wave velocity anomalies to be anti-correlated. [*Berryman*, 2000] obtained a theoretical value of $R \sim 3.0$ for regions of partial melt. With the constrain from surface geophysical data, [*Forte and Mitrovica*, 2001] predicted compositional and thermal heterogeneities in the lower mantle, which is consistent with the anti-correlation of shear and acoustic wave velocity anomalies, as acoustic velocity anomalies are correlated with lateral changes in composition, while shear velocity anomalies are strongly anti-correlated with thermal changes. Recently, [*Saltzer et al.*, 2001] found acoustic and shear velocity anomalies anti-correlated throughout the entire mantle. However, while R increases down to about 2200 km of depth, it decreases below this depth, which is inconsistent with other studies (e.g. [*Bolton*, 1996; *Su and Dziewonski*, 1997; *Masters et al.*, 1999; *Ritsema and van der Heijst*, 2001]). They found a systematic difference in R at lower mantle depths, between the regions that had undergone subduction and those that did not, which is in accord with the work of [*Bolton*, 1996] who found the largest R in the middle of Pacific, although for the lowermost mantle. In particular, R they obtained is larger in the areas that are thought to be active upwellings (e.g. [*Forte and Mitrovica*, 2001]), far from the ring around Pacific.

While global tomographic S models consistently show the predominance of long wavelength structure at the base of the mantle, and in particular two large slow domains in the central Pacific and under Africa referred to as "superplumes" (e.g. [*Grand et al.*, 1997; *Ritsema et al.*, 1999; *Mégnin and Romanowicz*, 2000; *Masters et al.*, 1999; *Gu and Dziewonski*, 2001]), seismic evidence for shorter scale heterogeneity at these depths is growing. The existence of strong heterogeneity in the vicinity of the two superplumes has been documented through forward modeling of seismic travel times and waveforms (e.g. [*Bréger and Romanowicz*, 1998; *Ritsema et al.*, 1998; *Ni and Helmberger*, 2001; *Wen*, 2001]). Recent studies have also found evidence for locally rapid variations in other areas such as middle America (e.g. [*Wysession et al.*, 2001]). Furthermore, while there is evidence for zones of strongly reduced P velocity at the base of the mantle [*Garnero and Helmberger*, 1995], there is no evidence that these are accompanied with a comparable drop in S velocity (e.g. [*Castle and van der Hilst*, 2000]).

Through an inversion of PcP-P and PKP(AB-DF) data, we recently obtained maps of D" with lateral P velocity variations that show much shorter wavelength features than seen in S tomographic models [*Tkalčić et al.*, 2001]. Here, we consider PcP-P and ScS-S travel time residuals, and analyze their spatial relationship in several regions which are sampled both by PcP and ScS, in comparison to tomographic maps. We discuss implications of our results for the relative variations in P and S velocities in the lowermost mantle, in particular from the stand-point of $\partial lnV_s/\partial lnV_p$ ratios and their interpretation.

4.3 Data

In this study, we use two types of data: 1) PcP-P and 2) ScS-S differential travel time measurements. Our PcP-P dataset was obtained from measurements on vertical components of mainly broadband, and some short period records. In addition to the initial global PcP-P dataset considered in [*Tkalčić et al.*, 2001], we measured PcP-P data for specific paths bottoming under Africa. Event parameters from the relocated EHB catalog are used (*Engdahl et al.*, 1998). All measurements are done by aligning P and PcP waveforms. All data with poor signal to noise ratio or with different dominant frequencies of P and PcP are discarded, resulting in a measurement precision of $\sim 0.2 - 0.5$ seconds. The differential travel time residuals are then computed with respect to the spherically symmetric reference model *ak*135 [*Kennett et al.*, 1995] and corrected for Earth's ellipticity.

ScS-S differential travel times are measured in the same way as PcP-P, on transverse components of broadband records, to minimize the contribution from SKS phases. The uncertainty in these measurements is between 0.5 and 1.0 seconds. The paths corresponding to these data complement PcP coverage of the D" region (hereafter defined as a 300 km thick layer at the base of the mantle) in some regions we studied. We also use ScS-S data from the MOMA array (Missouri to Massachusetts Temporary Broadband Seismic Array) measured and used previously by [*Wysession et al.*, 2001]. ScS-S residuals are calculated with respect to the *PREM* model [*Dziewonski and Anderson*, 1981], and also corrected for Earth's ellipticity.

4.4 Results

4.4.1 Comparison of PcP-P residuals with tomographic models

Figure 4.1 (a,b) shows the global distribution of PcP-P travel time residuals, plotted at the surface projection of PcP reflection points on the core-mantle boundary (CMB) with an S and a P tomographic models in the background [*Mégnin and Romanowicz*, 2000] and [*Obayashi and Fukao*, 1997], respectively. We selected only data corresponding to epicentral distances $\geq 55^o$, for which paths of P and PcP are similar, except in the lowermost mantle, so that the travel time residuals should be most sensitive to the structure in the lowermost mantle. The complete dataset has previously been shown in [*Tkalčić et al.*, 2001]. The spatial coverage of PcP in the lowermost mantle is limited by the available source-receiver geometry. Interestingly, the residuals exhibit a relatively high level of spatial coherency. For instance, a broad area under eastern Asia is well sampled, and there is a consistency in the sign of residuals. Assuming that PcP-P residuals are most sensitive to the structure in the lowermost mantle, their negative sign under eastern Asia is in agreement with a fast anomaly in the lowermost mantle, as seen in shown P and S tomographic models in Figure 4.1 (a,b), as well as in most P and S wave velocity tomographic models in this region.

On the global scale, most PcP reflection points correspond to fast regions at the bottom of the mantle in the tomographic models. However, not all of them have negative PcP-P residuals, and there are regions with smaller scale lateral variations than indicated by tomographic maps, which deserve more detailed investigation, as will be discussed below.

4.4.2 Eastern Asia

The apparent consistency of PcP-P residuals and S velocity maps in D" in eastern Asia gives us the opportunity to try and estimate the ratio R using a similar approach as in [*Tkalčić et al.*, 2001], in which we compare observed PcP-P travel time residuals, with those predicted from an existing P tomographic model. Here we do the same, by scaling an existing S tomographic model to P using a given ratio R, allowing for variations in depth of R.

Figure 4.2 illustrates a depth profile of PcP-P anomalies accumulated along the PcP and P paths from our PcP-P dataset, through Berkeley S wave velocity model $SAW24B16$. The model is divided in 18 layers. The maximum, along with the median values of contributions to travel times from $SAW24B16$ model scaled to P, using a constant factor of 0.55, are indicated by large and small circles, respectively, for each layer, and separately for positive and negative anomalies. The numbers indicate how many paths of total PcP-P dataset yielded in negative or positive anomalies in each layer. This figure, similar to an rms depth profile, gives a quantitative sense for how much PcP-P residuals are affected by the heterogeneity in the mantle. The variance reduction in PcP-P data will be most sensitive to varying R values in the lowermost 500 km of the mantle and in the uppermost 300 km of the mantle, and less sensitive to varying R elsewhere. Furthermore, while PcP-P paths sample most of the mantle in an uniform manner regarding positive and negative anomalies, in the lowermost mantle, most PcP-P data are sampling through fast regions seen by S model. This might be a source of bias, if calculating R from the whole PcP-P dataset.

We performed tests which confirmed that the PcP-P dataset (for distances $> 55^o$) is mostly sensitive to R in the bottom part of the mantle. We also take into account previous results indicating an increase with depth of R in the lower mantle (e.g. [*Robertson and Woodhouse*, 1996]). We therefore fix $R = 1.6$ in the upper mantle, allow for a linear increase of R with depth down to the top of a bottom mantle layer, and a constant R in that layer. We perform a two parameter search for the thickness of and the value of R in that layer.

Results for 3 different S models are presented in Figure 4.3 and Figure 4.4. The variance reduction for the best fitting R profile is on the order of $55 - 60\%$, depending on the S model considered, and the range of R obtained at the bottom of the mantle is $1.8 - 2.7$. Variance reduction in PcP-P data is not sensitive to the thickness of the lowermost layer, so we present the results for the best fitting depth profile of R by taking the lowermost layer to extend from the depth of 2000 km to the base of the mantle (shown by shaded area in Figure 4.4). As expected, R is largest (2.7) for the model $SAW24B16$ [*Mégnin and Romanowicz*, 2000], which has stronger velocity rms than other models in the last 500km of the mantle (the best fitting depth profile of R is shown by solid line in Figure 4.4). We obtain $R = 1.8$ at the bottom of the mantle for both $SB4L18$ [*Masters et al.*, 1999] and $S362D1$ [*Gu and Dziewonski*, 2001] models (the best fitting depth profile of R is shown by thick dashed line). The uncertainty on R obtained is relatively large, but the results are compatible with tests we have performed comparing ScS-S and PcP-P residuals in this region. They indicate relatively "mild" values of R under Eurasia, possibly compatible with a thermal origin of anomalies (e.g. [*Agnon and Bukowinski*, 1990; *Karato*, 1993b]). It is interesting to compare this regional result with that obtained by applying the same methodology to the global dataset. Figure 4.4 also shows the best fitting R profile (thin dashed line) obtained when the Berkeley S model is used. In this case, the maximum in variance reduction is much less pronounced, yielding only a lower bound on the value of R in the bottom layer (always higher than 3). Also, the best variance reduction is obtained for $SAW24B16$ model and does not exceed 10%. We believe that, in particular, this reflects the different scales of lateral heterogeneity portrayed by the S models and detected by the PcP-P data, and that the estimate of R is therefore only meaningful, when estimated for well-defined specific regions.

4.4.3 Central America

Let us now consider a region well covered by PcP-P, for which smaller scale variations than given in global tomographic models are apparent. One such region is central America. Tomographic models indicate that positive P and S velocity anomalies prevail in the lowermost mantle in this region. In Figure 4.5, we plot PcP-P residuals at the PcP bouncing points, with model $SAW24B16$ in the background. Mostly negative residuals in the northwest of the region are consistent with the tomographic model. However, PcP-P residuals coherently change from negative to positive and again to mainly negative, when going from the west toward the east. The range in residuals is on the order of 2 seconds. This change happens on a scale of about 10 degrees at the CMB (i.e. $\sim$ 600 km). For a frequency of $\sim 1Hz$, and an epicentral distance of $\sim 70^0$, the width of Fresnel zone at the bottom of the mantle is about 480 km (e.g. [*Nolet*, 1987]), which is smaller than the spatial scale of the observed variations. Including mantle path corrections according to the P model of [*Kárason and Hilst*, 2001] does not explain the large PcP-P residuals, nor does it change the size and the sign of the gradient observed. Similarly, [*Wysession et al.*, 2001] showed that including mantle path corrections for ScS-S residuals does not change the cross-array variations in ScS-S residuals. By additional testing, we found that this also holds for models $SAW24B16$ and $S362D1$. We considered a Chile event recorded at MOMA array, and calculated mantle predictions for ScS-S, and separately for S and ScS ray paths. The results are presented in Figure 4.6.

In order to compare the variations of PcP-P with ScS-S residuals, we also plotted the ScS-S data of [*Wysession et al.*, 2001] in Figure 4.5 (without mantle corrections). With only a few exceptions, the variations in PcP-P residuals are in good agreement with the slow (respectively fast) regions delineated by ScS-S. Thus, while the background model only shows a mild northwest-southeast gradient from fast to normal velocities (other S tomographic models give similar results), the differential travel times indicate strong lateral variations on shorter scales, with P velocity tracking S velocity variations. From the range of variations in S and P residuals observed in this region, we infer that R cannot be much in excess of 2, although the sampling is not sufficient to draw completely robust conclusions.

4.4.4 African plume

The PcP-P coverage under the Atlantic ocean is very sparse (Figure 4.1). However, there is a group of paths from South Sandwich Islands events and a few mid-Atlantic ridge events recorded at various stations in Africa (Figure 4.7 (a)). We assembled a total of 22 PcP-P data from 12 events recorded on vertical broadband (20 data) and short period (2 data) instruments, in the time period from 1980 to 1998. These data sample D" near the edge of the southern part of the African superplume, along southwest-northeast oriented paths, as shown in Figure 4.7 (a). PcP-P residuals range from about +3 to -1.5 seconds along the marked AB profile (Figure 4.7 (a)). Figure 4.7 (b) shows a vertical cross-section through the line AB, showing three PcP and P paths from sources in the South Sandwich Islands and stations in south Africa, with model $SAW24B16$ in the background. This model shows more complexity than other S tomographic models in the vicinity of our PcP reflection points. It is clear that PcP samples the edge of the African superplume. The largest negative residual corresponds to a path from the southern mid-atlantic ridge to station BOSA.

In Figure 4.8 (a), we plot the PcP-P residuals along profile AB as a function of the PcP bottoming point longitude. Travel times are corrected for the mantle contribution above D" using KH2000 model, although this doesn't significantly change the amplitude and the relative variation of residuals (this also holds true using S velocity models (e.g. $SAW24B16$ or $S362D1$), applying a constant scaling factor from S to P of 0.5. Residuals sharply increase between 0^o and 10^oE, and then go back to negative values at 18^oE. Qualitatively, the increase in residuals from west to east out to station LBTB can readily be explained by PcP moving out of the fast velocity region in D" and increasingly sampling the low velocities in the plume. The drop to smaller values, for the longer path to the Tanzania Array could be partly explained if one allows strong low velocities in the plume to persist high above the CMB, so that both P and PcP are affected. However, absolute travel time measurements for this path indicate that P is delayed by about 1 sec and PcP slightly advanced, with respect to $ak135$, so that PcP appears to be detecting fast velocity near the CMB.

[*Ritsema et al.*, 1998] studied ScS-S and S-SKS travel time residuals along the same path, and also found rapid lateral variations. They proposed a model in which the African plume extends up to 1500 km above the CMB. We measured ScS-S residuals for the two South Sandwich Island events recorded on the Tanzania Array during its time of operation (07/25/94 (-56.343, -27.395) and 04/14/95 (-60.843, -20.023)). The first event was already considered in [*Ritsema et al.*, 1998]. The measured residuals are shown as crosses at the ScS reflection points in Figure 4.7 (a) and range from +1 to +12 seconds. In Figure 4.8 (b), we plot these residuals as a function of longitude of the ScS reflection point. Even though the sampling is somewhat complementary to that of PcP-P (Figure 4.7 (a)), both datasets show similar trends, with a strong increase followed by an abrupt decrease between 0^o and $20^o E$ in longitude. The range of variation of P and S residuals is large and occurs on length scales of less than 1000km, if projected on the CMB. In this region, it is not appropriate to estimate R using tomographic models (or the combination of a tomographic S model and PcP-P travel time data, as was done in Eurasia). However, the sampling is favorable to obtain an estimate of R in the bottom 300-500 km of the mantle from the comparison of ScS-S and PcP-P residuals. We obtain an estimate of $R = 2.5 \pm 0.3$, which is not very different from the estimate obtained in Eurasia, although the short scale lateral variations point to the existence of chemical heterogeneity (e.g. [*Wysession et al.*, 2001]).

Finally, in Figure 4.7 (c), we also consider a slightly more northerly path, CD, on which PcP-P residuals are consistently negative ($\sim -1.5sec$). This observation is puzzling, because the area of D" sampled by PcP is deeper inside the plume, as delineated by tomographic models, and on this profile, the plume does not extend as high above the CMB (Figure 4.7 (c)), so that one would expect PcP to be slowed down much more than P. However, we found advanced absolute PcP for these paths. Because these paths correspond to larger epicentral distances ($58 - 72^o$), even if PcP is affected by structure in the upper mantle, P would be affected in a similar way. We therefore infer that the fast PcP anomaly likely originates at the base of the mantle, in a region where S velocities are consistently slow in tomographic models. This could imply a chemical component to heterogeneity in this region. However, one could also invoke a localized "bump" on the core mantle boundary (on the order of 10km), which is dynamically plausible in a region of upwelling. Unfortunately, the lack of ScS-S data in this specific area, prevents us from making more definitive conclusions.

4.4.5 Eastern edge of Pacific superplume

Let us now consider a region of D", located in the Pacific, at the eastern edge of the Pacific superplume (Figure 4.9 (a)). Our PcP-P dataset consists of 24 measurements from the event of 94/02/12 (-10.760, -128.857) measured at California stations. We were also able to measure 11 ScS-S differential travel times for the same event. Some stations had usable records for both PcP-P and ScS-S measurements. In this way, we obtained very similar sampling of D" by PcP and ScS waves. As can be seen from Figure 4.9 (a), the PcP-P residuals are all negative, with a minimum at -2.2 seconds (with respect to $ak135$), in agreement with predictions of several tomographic P velocity models (e.g. [*Boschi and Dziewonski*, 2000; *Obayashi and Fukao*, 1997; *Tkalčić et al.*, 2001]). On the other hand, all ScS-S residuals with ScS bottoming in the same area are strongly positive, ranging from 3 to 9 seconds (with respect to $PREM$). There is no systematic variation of residuals with the location. Mantle corrections using KH2000 stripped of D" shift PcP-P residuals up to 1 second toward zero value, but the corrections for ScS-S from $SAW24B16$ model stripped of D" do not reduce ScS-S residuals by more than 1 second. The region sampled in the lowermost mantle is not far from the area of study of [*Bréger and Romanowicz*, 1998] and [*Bréger et al.*, 2001], who analyzed SKS-Sdiff and ScS-S travel time residuals on paths between Fiji-Tonga and North America. These studies found strong lateral gradients on the eastern border of the Pacific plume, and, in particular, argued for a stronger S velocity contrast (up to +5%) associated with the tongue of fast velocity bordering the plume on the east. The present data sample the eastern side of this "tongue" (See cross section in Figure 4.9 (b)) somewhat further south (Figure 4.9 (a)). While it is tempting to invoke chemical heterogeneity to explain the negative correlation between P and S velocity anomalies inferred from the PcP-P and ScS-S data, we cannot rule out the possibility that the eastern edge of the fast anomaly discussed in [*Bréger and Romanowicz*, 1998] could also be very sharp. The smooth character of tomographic models would miss the precise location of this sharp edge. If this anomaly does not extend very far above the CMB, the difference in ray path and location of the ScS and PcP bounce points could cause ScS to miss this anomaly, while PcP would sense it, and result in an apparent incompatibility. Fresnel zone arguments would tend to dismiss this interpretation, leading us to favor a combination of effects: sharp gradients across compositionally different domains. Interestingly, an anomalously large ratio $R = \partial lnV_s / \partial lnV_p$ was found in a location corresponding to the continuation of this fast P region further toward the west [*Bolton*, 1996]. We suggest that this could be due to a similar situation.

4.5 Conclusions

We have compared the lateral variations observed in a global dataset of PcP-P differential travel times sensitive to structure in the bottom 500-1000 km of the mantle, to the predictions of global tomographic models, on the one hand, and ScS-S differential travel times, on the other.

This comparison has shown that the different datasets are in good agreement in some regions, in particular in eastern Asia, where fast anomalies over a broad domain are inferred both from tomographic P and S models and from the core-reflected phase data, resulting in a value of R compatible with a thermal origin of heterogeneity at the base of the mantle in this region. On the other hand, the PcP-P data indicate shorter scale lateral variations in many other regions. We studied in detail two such localized regions, under central America and south-east Africa, which correspond to downwelling and upwelling regions respectively, as seen in global tomographic models. In central America, lateral variations in P and S velocity appear to track each other, and resulting estimates of the ratio R in the last 500 km of the lower mantle are not particularly high. Under Africa, one profile shows similar results, whereas a neighboring path to the East indicates fast P velocities in the heart of the low S velocity African "plume". A similar situation is found on the eastern edge of the Pacific plume, where the simultaneous availability of PcP-P and ScS-S data allows us to infer the existence of sharp lateral gradients across compositionally different domains.

Strong lateral variations at the base of the mantle on scale lengths of several hundred kilometers have now been proposed in many studies. Our study documents this further, implying the existence of compositional variations in D". We note however that the computation of meaningful estimates of R at the base of the mantle, as an indicator of the nature of heterogeneity, remains a challenge. In order to do it correctly, better spatial sampling in both P and S data is needed, as different smoothing of short scale structures can lead to biased estimates.

In this study, we have not discussed the possible influence of anisotropy at the base of the mantle, which could differentially impact PcP and ScS data, and contribute to their apparent incompatibility, in particular in the Pacific, where such anisotropy has been documented (e.g. [*Vinnik et al.*, 1998; *Russell et al.*, 1998].

Collecting more PcP-P and ScS-S data with a compatible sampling of the lowermost mantle on the one hand, and increasing the resolution and accuracy of tomographic models on the other is necessary to gain further insight regarding the nature of heterogeneity in the lowermost mantle.

4.6 Acknowledgments

Data were obtained from the IRIS Data Management Center. We thank Nicolas Houy, who measured most of the PcP-P travel times used in this study and Michael Wysession for sharing his MOMA S-ScS dataset with us. Figures were made with the General Mapping Tools (P. Wessel and W. H. F. Smith, *EOS Trans. AGU* **76**, 329, 1995).

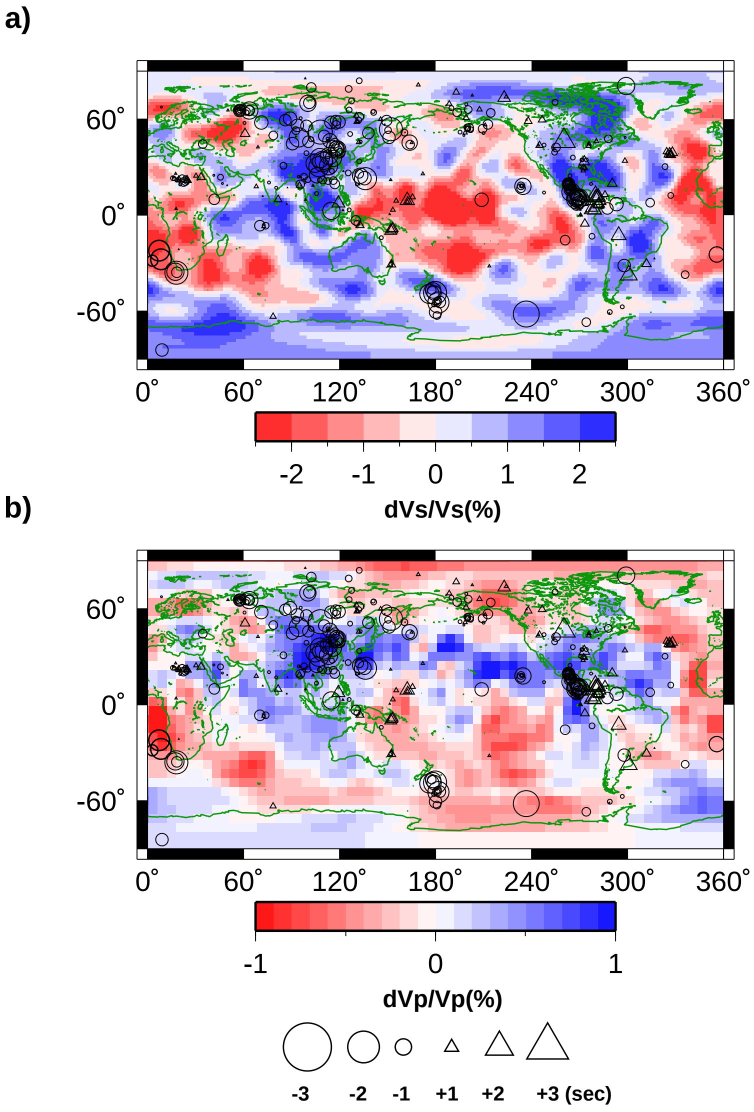

Figure 4.1. PcP-P travel time residuals plotted at the surface projections of PcP bouncing points. Residuals are calculated with respect to $ak135$ model, and corrected for ellipticity. Triangles and circles indicate positive and negative residuals, respectively. The background model is: **(a)** S wave velocity model $SAW24B16$ by [*Mégnin and Romanowicz*, 2000]; **(b)** P wave velocity model by [*Obayashi and Fukao*, 1997]

.

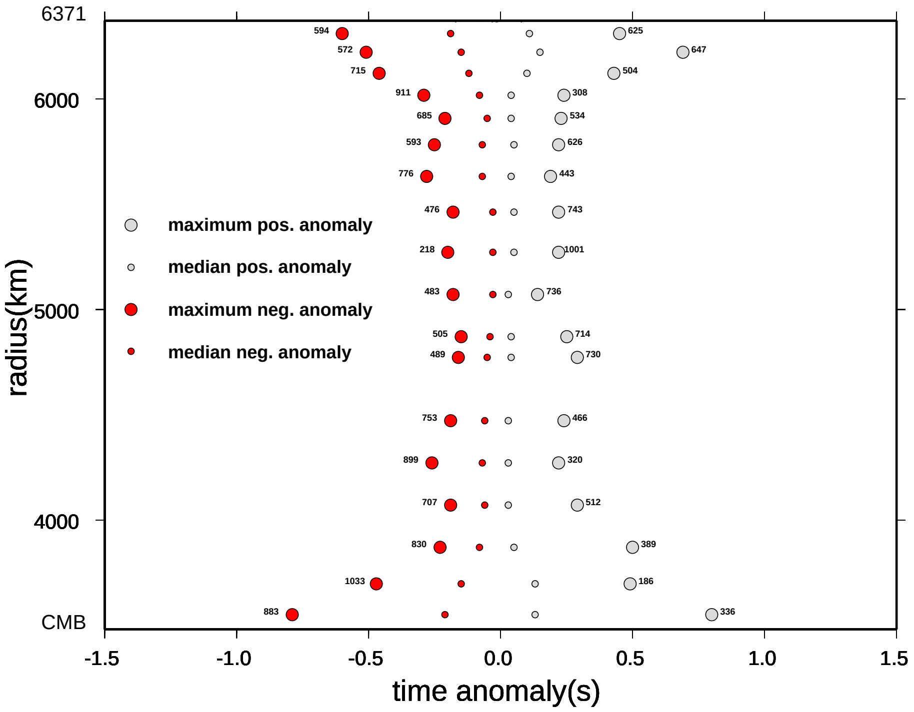

Figure 4.2. Depth profile of PcP-P anomalies accumulated along the PcP and P paths through S wave model $SAW24B16$ scaled to P model using factor 0.55. The model is divided in 18 layers. The maximum, as well as the median value of PcP-P travel time contributions, are indicated in each layer by large and small circles, respectively. Red and gray symbols indicate travel time contributions calculated for positive and negative anomalies separately. The numbers indicate how many paths of total PcP-P dataset yielded in negative or positive anomalies in each layer.

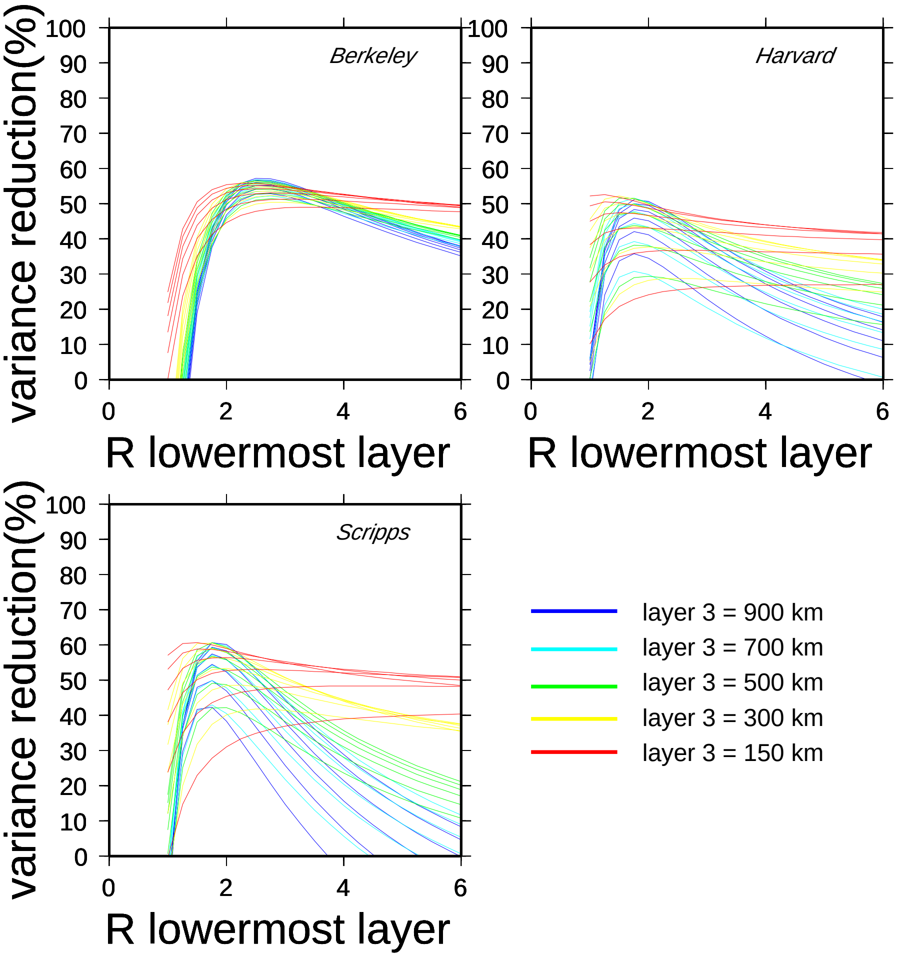

Figure 4.3. Results for variance reduction in a subset of PcP-P residuals with PcP reflection points under Eurasia, obtained comparing PcP-P travel time data to S tomographic velocity models, using a two-parameter search for the thickness of the bottom layer and the value of R inside it. Variance reduction is shown as a function of obtained value of R in the bottom layer. Thickness of the lowermost layer is indicated by colors. For the same thickness, multiple curves from top to bottom represent decreasing value of R in the bottom layer from 3 to 1 by a step of 0.4. The S models used are: **(top left)** $SAW24B16$ by [*Mégnin and Romanowicz*, 2000]; **(top right)** $S362D1$ by [*Gu and Dziewonski*, 2001]; **(bottom)** $SB4L18$ by [*Masters et al.*, 1999]

.

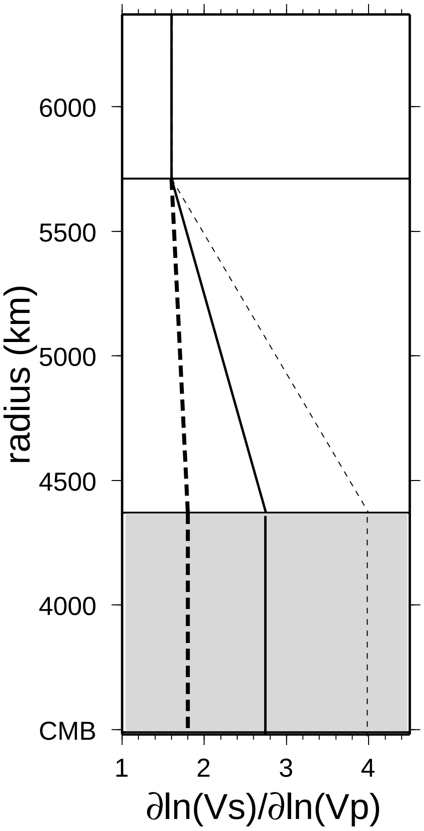

Figure 4.4. Best fitting depth profiles of $R = \partial lnV_s/\partial lnV_p$ obtained by comparing PcP-P travel time data to S tomographic velocity models, using a parameter search for the thickness of the bottom layer and the value of R inside it. Comparison restricted to a subset of PcP-P residuals with PcP reflection points under Eurasia with global S tomographic models $SAW24B16$ (solid line, variance reduction 57%), and models $SB4L18$ and $S362D1$ (thick dashed line, variance reduction 60% and 52%, respectively). The thin dashed line corresponds to the best fitting depth profile of R using the global PcP-P dataset and model $SAW24B16$ (variance reduction 10%). Shaded area represents the uncertainty in the thickness of the lowermost layer for the parametrization used.

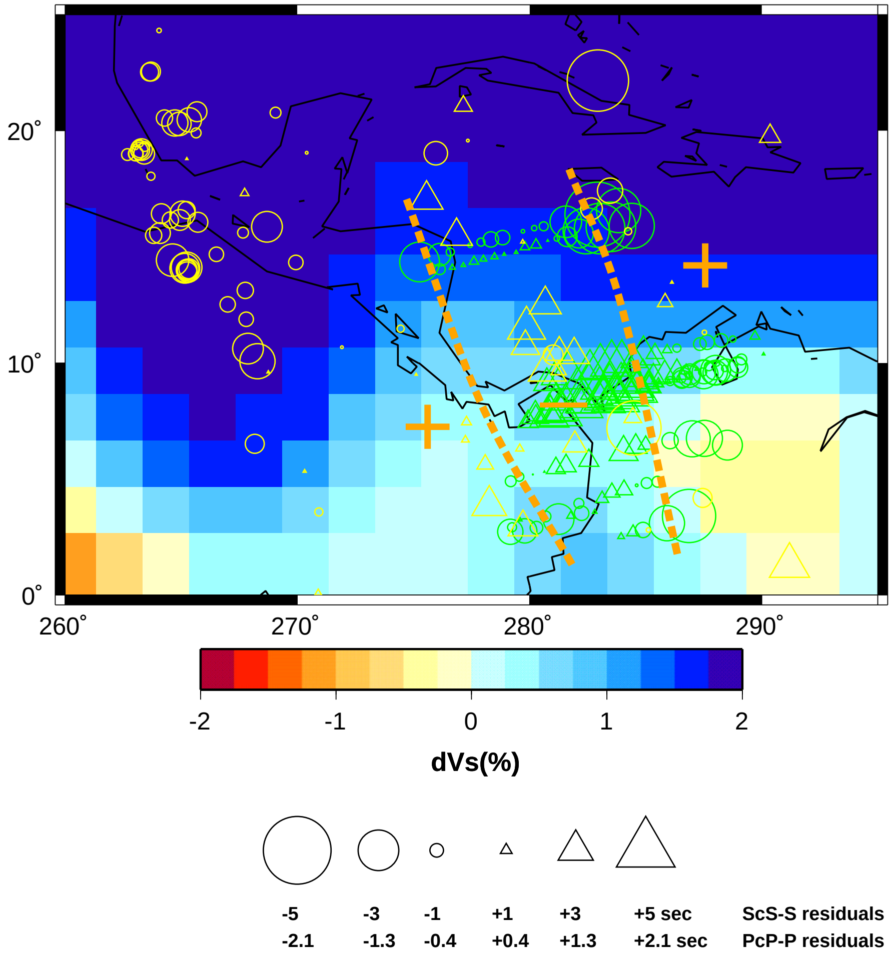

Figure 4.5. PcP-P (yellow symbols) and ScS-S (green symbols) travel time residuals plotted at the surface projections of PcP and ScS bouncing points beneath central America. The size of symbols is scaled in such a way that the largest absolute PcP-P residual corresponds to the largest absolute ScS-S residual. The background model is $SAW24B16$. Orange dashed lines delineate the slow velocity anomaly found in study by [*Wysession et al.*, 2001]

.

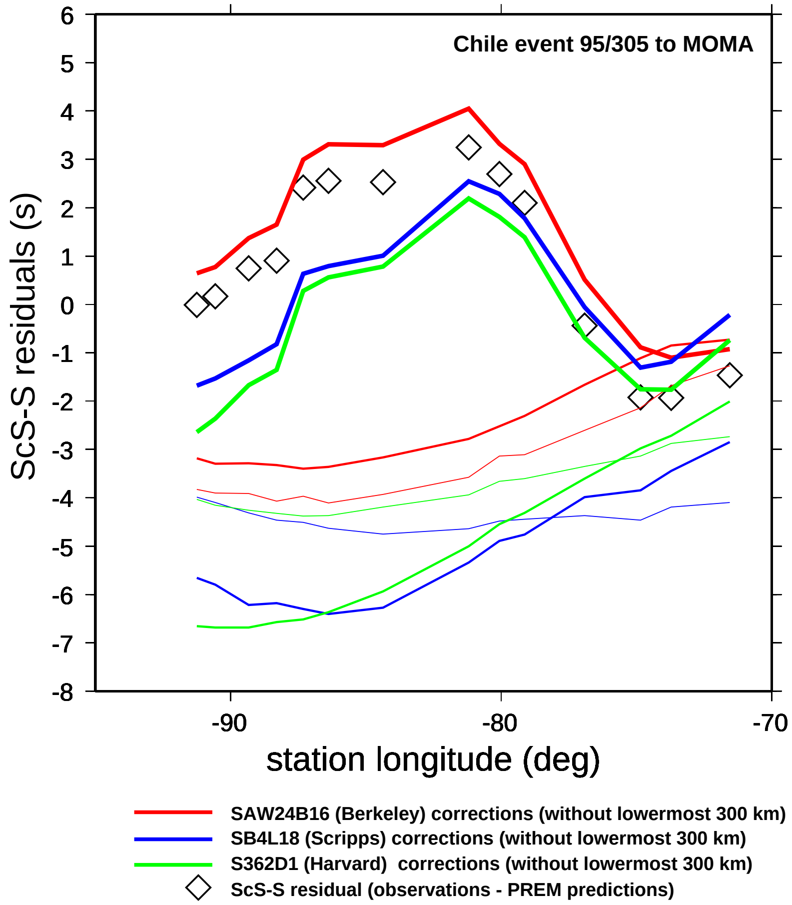

Figure 4.6. ScS-S residuals (diamonds) and mantle corrections (lines) for 3 S tomographic models from Figure 4.3, for a single event recorded at MOMA array in United States [*Wysession et al.*, 2001]. Thick, medium and thin solid lines represent ScS-S, S and ScS mantle corrections, respectively.

Figure 4.7. **(top)** PcP-P travel time residuals plotted at the surface projections of PcP bouncing points for south Atlantic/south Africa region. The largest triangle and circle correspond to residuals of +3 s and -1.5 s, respectively. The background model is $SAW24B16$. Green crosses are ScS reflection points. The AB line connects South Sandwich Island region with the Tanzania network, and the CD line connects the same region with BGCA station; **(middle)** Cross-section through $SAW24B16$ along profile AB, with P and PcP paths from a South Sandwich Islands region event to SUR, BOSA and LBTB stations and a south Atlantic ridge event to Tanzania network; **(bottom)** Cross-section through $SAW24B16$ along profile CD, with P and PcP paths from a South Sandwich Islands region event to BGCA station.

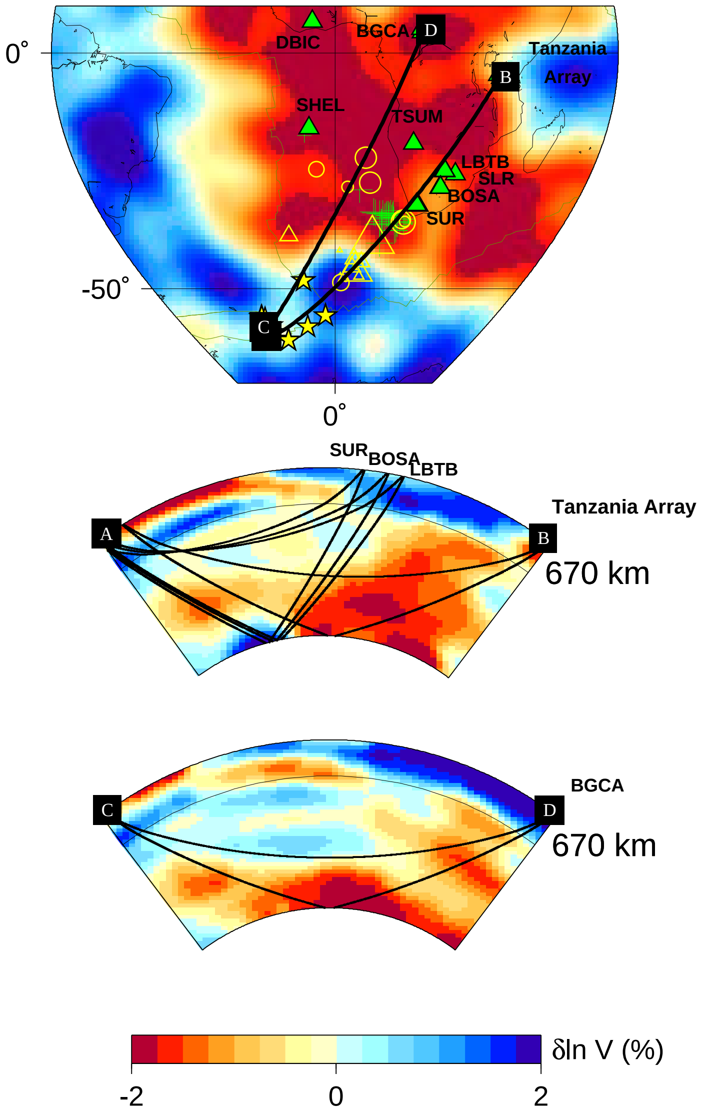
0°
-50°
0°
DBIC
BGCA
D
Tanzania
Array
B
SHEL
TSUM
LBTB
SLR
BOSA
SUR
C
SUR
BOSA
LBTB
Tanzania Array
A
B
670 km
BGCA
C
D
670 km
δln V (%)
-2
0
2

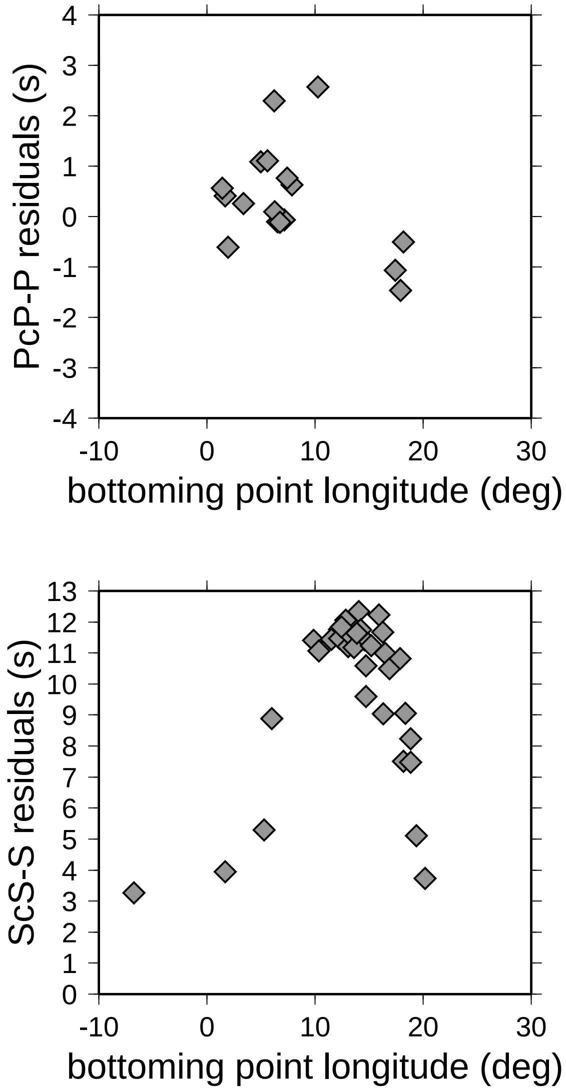

Figure 4.8. **(top)** Subset of PcP-P travel time residuals for paths associated with the AB profile from Figure 4.7, plotted as a function of PcP bouncing points longitude. The residuals are calculated with respect to $ak135$ model, and corrected for ellipticity; **(bottom)** ScS-S residuals originating from the two events in the south Atlantic: 07/25/94 (-56.343, -27.395) and 04/14/95 (-60.843, -20.023), plotted as a function of PcP bouncing points longitude. The S residuals are calculated with respect to $PREM$ model, and corrected for ellipticity.

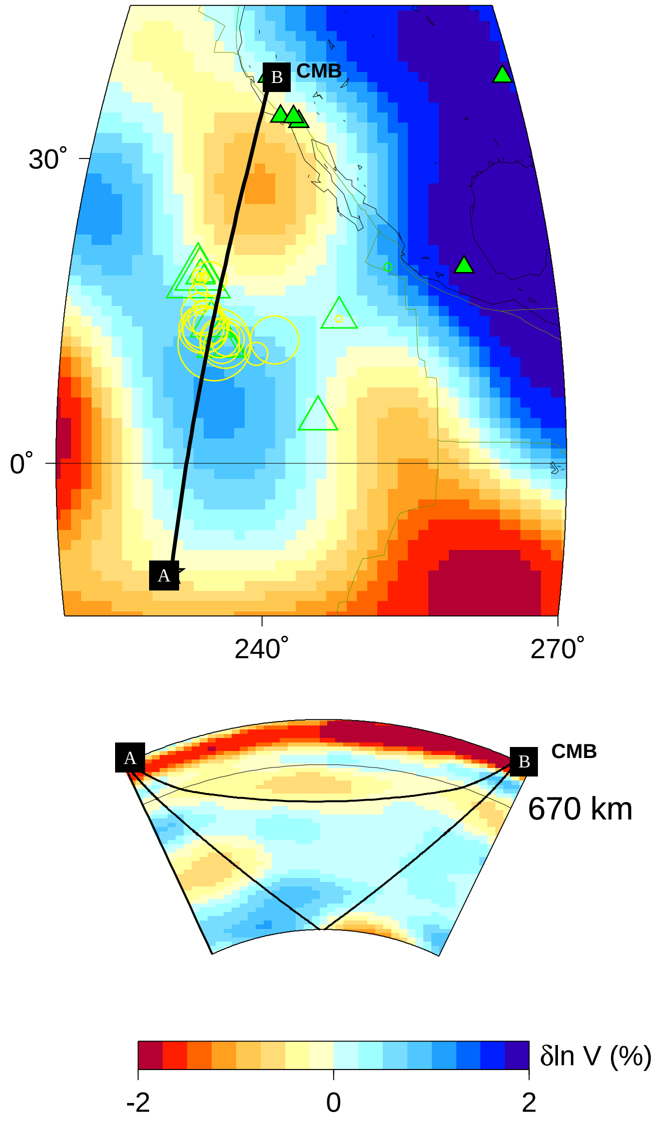

Figure 4.9. **(top)** PcP-P (yellow symbols) and ScS-S (green symbols) travel time residuals plotted at the surface projections of PcP and ScS bouncing points for eastern Pacific region. The largest triangle and circle correspond to residuals of +9 s and -2.2 s, respectively. The background model is $SAW24B16$. The AB line connects the 94/02/12 event with station CMB in California; **(bottom)** Cross-section through $SAW24B16$ along profile AB, with the corresponding PcP and P paths.

General Conclusions

- In an analysis of November 1997 Long Valley Caldera swarm earthquakes, we have found a strong evidence for anomalous seismic radiation, characterized by non-double couple moment tensors with significant volumetric components.
- We propose that the anomalous events may have been triggered by processes related to high-pressure fluid injection or pressurization of fluid saturated faults due to magmatic heating, and rule out near-source structure bias effects in a related study.
- In an analysis of September 29, 1996 anomalous volcanic event originated beneath Bárdarbunga caldera in Iceland, we found that the non-double couple moment tensor is characterized by a strong CLVD component, and no evidence for a significant isotropic (volumetric) component driving the source radiation process. We currently study other earthquakes in this area, in order to understand a physical mechanism that produces CLVD signature.
- By forward modeling and inversion of velocity structure in the lowermost mantle, we showed that over 90% of travel time residuals of core related phases PKP(AB-DF), can be explained by heterogeneous structural effects on travel times in the lowermost mantle.
- We derived a P velocity tomographic model of the D" layer, characterized by prominent fast features under mid America and east Asia, a fast belt across Pacific, a slow region under the southwestern Pacific and southern Africa, as well as sharp transitions from fast to slow, for instance under Alaska and south Atlantic.
- We demonstrated that the exclusion or inclusion of polar PKP(DF) paths doesn't

change the derived P velocity model of D” significantly. In addition, accounting for a radial model of inner core anisotropy, compatible with normal mode splitting data, prior to inversion, produces a model of D” that is very similar to the models for which inner core anisotropy is not included.

- We showed that either the short scale heterogeneity in D”, or a combination of medium scale heterogeneity in D” and seismic anisotropy in the inner core, have to be invoked in order to explain a significant portion of the PKP(BC-DF) travel time residuals.
- We documented the existence of compositional variations in D” using core reflected waves PcP and ScS in combination with P and S waves, respectively. In some regions of D”, the combined ScS-S and PcP-P datasets imply short scale lateral variations that are not resolved by global tomographic models (central America).
- While in some areas (central America and southeastern Africa) we don’t find excessive values for the ratio $R = \partial lnV_s / \partial lnV_p$ (~ 2.5), in the heart of the African Plume and on the edge of the Pacific Plume, variations in P and S velocities appear to be incompatible, indicating an non-thermal origin of velocity heterogeneities.

Bibliography

Agnon, A. and M. S. T. Bukowinski, δ_s at high pressure and $\partial lnV_s/\partial lnV_p$ in the lower mantle, *Geophys. Res. Lett.*, **17**, 1,149-1,152, 1990.

Aki, K. and P. Richards, Quantitative Seismology, Theory and Methods (freeman, San Francisco), p. 932, 1980.

Barker, J. S. and C. A. Langston, A teleseismic body-wave analysis of the May 1980 Mammoth Lakes, California, earthquakes, *Bull. Seism. Soc. Am.*, **73**, 419-434, 1983.

Bataille, K. and S. M. Flatte, Inhomogeneities near the core-mantle boundary inferred from short-period scattered PKP waves recorded at the GDSN, *J. Geophys. Res.*, **93**, 15,057-15,064, 1988.

Berryman, J. G., Seismic velocity decrement ratios for regions of partial melt in the lower mantle, *Geophys. Res. Lett.*, **27**, 421-424, 2000.

Bijwaard, H., W. Spakman and R. Engdahl, Closing the gap between regional and global travel time tomography, *J. Geophys. Res.*, **103**, 30,055-30,078, 1998.

Bokelmann, G. H. R., and P. G. Silver, The Caribbean lower mantle from a portable study, *Eos Trans. Am. Geophys. Union*, **72**, 339, 1991.

Bolton, H. F., Long period travel times and the structure of the mantle, *PhD Thesis*, University of California, San Diego, 1996.

Bolton, H. and G. Masters, Travel times of P and S from the global digital seismic networks: Implications for the relative variation of P and S velocity in the mantle, *J. Geophys Res.*, **106**, 13,527-13,540, 2001.

Boschi, L. J. and A. M. Dziewonski, Whole Earth tomography from delay times of P, PcP, PKP phases: lateral heterogeneities in the outer core, or radial anisotropy in the mantle?", *J. Geophys. Res.*, *105*, 13,675-13,696, 2000.

Bréger, L. and B. Romanowicz, Three dimensional structure at the base of the mantle beneath the Central Pacific, *Science*, **382**, 244-248, 1998.

Bréger, L., B. Romanowicz and H. Tkalčić, PKP(BC-DF) travel time residuals and short scale heterogeneity in the deep earth, *Geophys. Res. Lett.*, **26,** 3,169-3,172, 1999.

Bréger, L., H. Tkalčić, and B. Romanowicz, The effect of D" on PKP(AB-DF) travel time residuals and possible implications for inner core structure, *Earth Planet. Sci. Lett.*, **175**, 133-143, 2000.

Bréger, L., B. Romanowicz, and C. Ng, The pacific plume as seen by S, ScS, and SKS, *Geophys. Res. Lett.*, **28,** 1,859-1,862, 2001.

Campus, P, P. Suhadolc, G. F. Panza, J. Sileny, Complete moment tensor retrieval for weak events: Application to orogenic and volcanic areas, *Tectonophysics*, **261**, 147-163, 1996.

Castle, J. C. and R. D. van der Hilst, The core-mantle boundary under the Gulf of Alaska: no ULVZ for shear waves, *Earth Planet. Sci. Lett.*, **176**, 311-321, 2000.

Cormier, V. F. and G. L. Choy, A search for lateral heterogeneity in the inner core from differential travel times near PKP-D and PKP-C, *Geophys. Res. Lett.*, **13**, 1,553-1,556, 1986.

Creager, K. C. and T. H. Jordan, Aspherical structure of the core-mantle boundary from PKP travel times, *Geophys. Res. Lett.*, **13**, 1,497-1,500, 1986.

Creager, K. C., Anisotropy of the inner core from differential travel times of the phases PKP and PKIKP, *Nature*, **356**, 309-314, 1992.

Creager, K. C., Large-scale variations in inner core anisotropy, *J. Geophys. Res.*, **104**, 23,127-23,139, 1999.

Doornbos, D. J., Seismic wave scattering near caustics: observation of PKKP precursors, *Nature*, **247**, 34-35, 1974.

Dreger, D. S. and D. V. Helmberger, Determination of source parameters at regional distances with 3-component sparse network data, *J. Geophys. Res.*, **98**, 8,107-8,125, 1993.

Dreger, D. S., H. Tkalčić, and M. Johnston, Dilational processes accompanying earthquakes in the Long Valley Caldera, *Science*, **288**, 122-125, 2000.

Dreger, D. S. and B. Woods, Regional distance seismic moment tensors of nuclear explosions, *submitted to Tectonophysics*, 2001.

Durek, J. and B. Romanowicz, Inner core anisotropy inferred by direct inversion of normal mode spectra, *Geophys. J. Int.*, **139**, 599-622, 1999.

Dufumier H. L. and L. Rivera, On the resolution of the isotropic component in moment tensor inversion, *Geophys. J. Int.*, **13**, 595-606, 1997.

Du, Z. and G. R. Foulger, Variation in the crustal structure across central Iceland, *Geophys. J. Int.*, **145**, 246-264, 2001.

Dziewonski, A. M. and D. L. Anderson, Preliminary reference Earth model, *Phys. Earth planet. Inter.*, **25**, 297-356, 1981.

Dziewonski, A. M., J. H. Woodhouse, D. Giardini, X. Li and A. Morelli, Global images of the Earth interior, *Eos Trans. Am. Geophys. Union*, **67**, 1100, 1986.

Ekstrom, G. and A. M. Dziewonski, Eos, **64**, 262, 1983.

Engdahl, E. R., R. D. van der Hilst, and R. P. Buland, Global teleseismic earthquake relocation with improved travel times and procedures for depth determination, *Bull. Seism. Soc. Am.*, **88** No 3, 722-743, 1998.

Forte, A. M. and J. X. Mitrovica, Deep-mantle high-viscosity flow and thermochemical structure inferred from seismic and geodynamic data, *Nature*, **410**, 1,049-1,056, 2001.

Frohlich, C., Earthquakes with non-double-couple mechanisms, *Science*, **264**, 804-809, 1994.

Garcia, R. and A. Souriau, Amplitude of the core mantle boundary topography estimated by stochastic analysis of core phases, *Phys. Earth planet. Inter.*, **117**, 345-359, 2000.

Garnero, E. J. and D. V. Helmberger, 1995. A very slow basal layer underlying large-scale low velocity anomalies in the lower mantle beneath the Pacific: evidence from core phases, *Phys. Earth planet. Inter.*, **91**, 161-176, 1995.

Garnero, E. J. and D. V. Helmberger, Seismic detection of a thin laterally varying boundary layer at the base of the mantle beneath the central-pacific, *Geophys. Res. Lett.*, **23**, 977-980, 1996.

Garnero, E. J., J. S. Ravenaugh, Q. Williams, T. Lay, and L. H. Kellogg, Ultralow velocity zone at the core-mantle boundary, in *The Core-Mantle Boundary, ed. M. Gurnis, M. E. Wysession, E. Knittle, B. A. Buffet*, 319-334, Washington DC, AGU, 1998.

Garnero, E. J., Heterogeneity of the lowermost mantle, *Annu. Rev. Earth Planet. Sci.*, **28**, 509-537, 2000.

Given, J. W., T. C. Wallace, and H. Kanamori, Teleseismic analysis of the 1980 Mammoth Lakes earthquake sequence, *Bull. Seism. Soc. Am.*, **72**, 1,093-1,109, 1982.

Grand, S. P., R. D. van der Hilst, and S. Widiyantoro, Global Seismic Tomography: A Snapshot of Convection in the Earth, *GSA Today*, **7**, No 4, 1-7, 1997.

Gu, Y. and A. M. Dziewonski, Shear velocity of the mantle and discontinuities in the pattern of lateral heterogeneities, *J. Geophys. Res.*, **106**, 11,169-11,199, 2001.

Haddon, R. A. W. and J. R. Cleary, Evidence for scattering of seismic PKP waves near the mantle-core boundary, *Phys. Earth planet. Inter.*, **8**, 211-234, 1974.

Hara T., K. Kuge, H. Kawakatsu, Determination of the isotropic component of deep focus earthquakes by inversion of normal-mode data, *Geophys. J. Int.*, **127**, 515-528, 1996.

Hill, D. P., R. A. Bailey, A. S. Ryall, Active tectonic and magmatic processes beneath Long Valley Caldera, eastern California - An overview, *J. Geophys. Res.*, **90**, 1,111-1,120, 1985.

Hill, D. P., Eos, **79**, E949, 1998.

van der Hilst, R.D., S. Widiyantoro and E.R. Engdahl, Evidence of deep mantle circulation from global tomography, *Nature*, **386**, 578-584, 1997.

Husebye, E. S., D. W. King, and R. A. W. Haddon, Precursors to PKIKP and seismic wave scattering near the mantle-core boundary, *J. Geophys. Res.*, **81**, 1,870-1,882, 1976.

Isaak, D. G., O. L. Anderson and R. E. Cohen, The relationship between shear and compressional velocities at high pressures: Reconciliation of seismic tomography and mineral physics, *Geophys. Res. Lett.*, **19**, 741-744, 1992.

Ishii, M. and J. Tromp, Normal-mode and free-air gravity constraints on lateral variations in velocity and density of Earth's mantle, *Science*, **285**, 1,231-1,236, 1999.

Jeanloz, R. and H. R. Wenk, Convection and anisotropy of the inner core, *Geophys. Res. Lett.*, **15**, 72-75, 1988.

Johnston M. J. S., A. T. Linde, M. T. Gladwin, and R. D. Borcherdt, Fault failure with moderate earthquakes, *Tectonophysics*, **144**, 189-206, 1987.

Jost, M. L. and R. B. Hermann, A student's guide and review to moment tensors, *Seism. Res. Lett.*, **60**, 37-57, 1989.

Julian, B. R., Evidence for dyke intrusion earthquake mechanisms near Long-Valley caldera, California, *Nature*, **303**, 323-325, 1983.

Julian, B. R. and S. A. Sipkin, Earthquake processes in the Long Valley Caldera area, California, *J. Geophys. Res.*, **90**, 1,155-1,169, 1985.

Kanamori, H. and D. L. Anderson, Theoretical basis of some empirical relations in seismology, *Bull. Seism. Soc. Am.*, **65**, 1,073-1,095, 1975.

Kárason, H. and R. D. van der Hilst, Improving global tomography models of P-wavespeed I: incorporation of differential times for refracted and diffracted core phases (PKP, Pdiff), *J. Geophys. Res.*, **106**, 6,569-6,587, 2001.

Karato, S., Inner core anisotropy due to the magnetic field-induced preferred orientation of iron, *Science*, **262**, 1,708-1,711, 1993.

Karato, S., Importance of anelasticity in the interpretation of seismic tomography, *Geophys. Res. Lett.*, **20**, 1,623-1,626, 1993.

Kawakatsu H., Observability of the isotropic component of a moment tensor, *Geophys. J. Int.*, **126**, 525-544, 1996.

Kennett, B. L. N., E. R. Engdahl, and R. Buland, Constrains on seismic velocities in the Earth from traveltimes, *Geophys. J. Int.*, **122**, 108-124, 1995.

Kennett, B. L. N., S. Widiyantoro and R. D. van der Hilst, Joint seismic tomography for bulk-sound and shear wavespeed in the Earth's mantle, *J. Geophys. Res.*, **103**, 12,469-12,493, 1998.

Knopoff L., M. J. Randall, Compensated linear-vector dipole - a possible mechanism for deep earthquakes, *J. Geophys. Res.*, **75**, 4,957-, 1970.

Kuge K., T. Lay, Systematic non-double-couple components of earthquake mechanisms -The role of fault zone irregularity, *J. Geophys. Res.*, **99**, 15,457-15,467, 1994.

Kuo, B-Y., Amplitude of Sdiff across Asia: effects of velocity gradient and Qs in the D" region and the asphericity of the mantle, *Earth Planet. Sci. Lett.*, **173**, 101-112, 1999.

Langbein, J., S. Wilkinson, J. Feinberg, and M. Johnston, Eos, **79**, E963, 1998.

Li, X.D. and B. Romanowicz, Global mantle shear-velocity model developed using nonlinear asymptotic coupling theory, *J. Geophys. Res.*, **101**, 22,245-22,272, 1996.

Masters, G. and F. Gilbert, Structure of the inner core inferred from observations of its spheroidal shear models, *Geophys. Res. Lett.*, **8**, 569-571, 1981.

Masters G., S. Johnson, G. Laske, and B. Bolton, A shear-velocity model of the mantle, *Philos. Trans. R. Soc. Lond. A*, **354**, 1,385-1,411, 1996.

Masters G., H. Bolton, and G. Laske, Joint Seismic Tomography for P and S Velocities: How Pervasive are Chemical Anomalies in the Mantle?, *EOS Trans. AGU*, **80**, S14, 1999.

McSweeney, T. J., K. C. Creager, and R. T. Merrill, Depth extent of inner-core seismic anisotropy and implications for geomagnetism, *Phys. Earth planet. Inter.*, **101**, 131-156, 1997.

Mégnin, C. and B. Romanowicz, The 3D shear velocity structure of the mantle from the inversion of body, surface, and higher mode waveforms, *Geophys. J. Int.*, *143*, 709-728, 2000.

Menke, W., Geophysical Data Analysis: Discrete Inverse Theory, Academic Press, New York, 96-97, 1989.

Miller A. D., G. R. Foulger, B. R. Julian, Non-double-couple earthquakes, 2. observations, *Rev. Geophys.*, **36**, 551-568, 1998.

Morelli, A., A. M. Dziewonski, and J. H. Woodhouse, Anisotropy of the core inferred from PKIKP travel times, *Geophys. Res. Lett.*, **13**, 1,545-1,548, 1986.

Nettles, M. and G. Ekstrom, Faulting mechanism of anomalous earthquakes near Bárdarbunga Volcano, Iceland, *J. Geophys. Res.*, **103**, 17,973-17,983, 1998.

Ni, S. and D. V. Helmberger, Horizontal transition from fast (slab) to slow (plume) structures at the core-mantle boundary, *Earth Planet. Sci. Lett.*, **187**, 310-310, 2001.

Nolet, G., Seismic wave propagation and seismic tomography, in: *Nolet, G. (Editor), Seismic Tomography, D. Reidel Publishing Company, Dordrecht*, 1987.

Obayashi, M. and Y. Fukao, P and PcP travel time tomography for the core-mantle boundary, *J. Geophys. Res.*, **102**, 17,825-17,841, 1997.

Panning, M., D. S. Dreger, and H. Tkalčić, Near-source velocity structure and isotropic moment tensors: a case study of the Long Valley Caldera, *Geophys. Res. Lett.*, **28**, 1,815-1,818, 2001.

Pasyanos, M. E., D. S. Dreger, and B. Romanowicz, Toward real-time estimation of regional moment tensors, *Bull. Seism. Soc. Am.*, **86**, 1,255-1,269, 1996.

Poupinet, G., R. Pillet, and A. Souriau, Possible heterogeneity of the Earth's core deduced from PKIKP travel times, *Nature*, **305**, 204-206, 1983.

Press, W. H., S. A. Teukolsky, W. T. Vetterling and B. P. Flannery, Numerical Recipes in C, 2nd ed., Cambridge University Press, 1994.

Ritsema, J., S. Ni, D. V. Helmberger and H. P. Crotwell, Evidence for strong shear velocity reductions and velocity gradients in the lower mantle beneath Africa, *Geophys. Res. Lett.*, **25**, 4,245-4,248, 1998.

Ritsema, J., H.-J. van Heijst, and J. Woodhouse, Complex shear wave velocity structure imaged beneath Africa and Iceland, *Science*, **286**, 1,925-1,928, 1999.

Ritsema, J. and H.-J. van der Heijst, Constraints on the correlation of P-wave and S-wave velocity heterogeneity in the mantle from P, PP, PPP, and PKPab travel-times, *submitted.*

Ritzwoller, M. G., G. Masters, and F. Gilbert, Observations of anomalous splitting and their interpretation in terms of aspherical structure, *J. Geophys. Res.*, **91**, 10,203-10,228, 1986.

Robertson, G. S. and J. H. Woodhouse, Ratio of relative S to P velocity heterogeneity in the lower mantle, *J. Geophys. Res.*, **101**, 20,041-20,052, 1996.

Rodgers, A. and J. Wahr, Inference of core-mantle boundary topography from ISC PcP and PKP travel times, *Geophys. J. Int.*, **115**, 991-1,011, 1993.

Romanowicz, B. and L. Bréger, Anomalous splitting of free oscillations: A reevaluation of possible interpretations, *J. Geophys. Res.*, **105**, 21,559-21,578, 2000.

Romanowicz, B., H. Tkalčić, and L. Bréger, On the Origin of Complexity in PKP Travel Time Data From Broadband Records, submitted to AGU Volume on Inner core and lower mantle, AGU Geodynamic Series, V. Dehant, Editor, 2001.

Romanowicz, B, Can we resolve 3D density heterogeneity in the lower mantle?, *Geophys. Res. Lett.*, **28**, 1,107-1,110, 2001.

Romanowicz, B., X.-D. Li, and J. Durek, Anisotropy in the inner core: Could it be due to low-order convection?, *Science*, **274**, 963-966, 1986.

Russell, S. A., T. Lay, and E. J. Garnero, Seismic evidence for small-scale dynamics in the lowermost mantle at the root of the Hawaiian hotspot, *Nature*, **393**, 255-258, 1998.

Sacks, I. S., J. A. Snoke, and L. Beach, Lateral heterogeneity at the base of the mantle revealed by observations of amplitudes of PKP phases, *Geophys. J. R. astr. Soc.*, **59**, 379-387, 1979.

Saltzer, R. L., R. D. van der Hilst, and H. Kárason, Comparing P and S wave heterogeneity in the mantle, *Geophys. Res. Lett.*, **28**, 1,335-1,338, 2001.

Snocke, J. A. and I. S. Sacks, Seismic modeling of lateral heterogeneity at the base of the mantle, *Geophys. J. R. astr. Soc.*, **86**, 801-814, 1986.

Souriau, A. and B. Romanowicz, Anisotropy in inner core attenuation: A new type of data to constrain the nature of the solid core, *Geophys. Res. Lett.*, **23**, 1-4, 1996.

Souriau, A. and G. Poupinet, Lateral variations in P velocity and attenuation in the D" layer, from diffracted P waves, *Phys. Earth planet. Inter.*, **84**, 227-234, 1994.

Su, W-J, R. L. Woodward, and A. M. Dziewonski, Degree 12 model of shear velocity heterogeneity in the mantle, *J. Geophys. Res.*, **99**, 6,945-6,980, 1994.

Su, W and A. M. Dziewonski, Simultaneous inversion for 3-D variations in shear and bulk velocity in the mantle, *Phys. Earth Planet. Int.*, **100**, 135-156, 1997.

Sylvander, M. and A. Souriau, Mapping S-velocity heterogeneities in the D" region, from SmKS differential travel times, *Phys. Earth planet. Inter.*, **94**, 1-21, 1996.

Sylvander, M. and A. Souriau, P-velocity structure of the core-mantle boundary region inferred from PKP(AB)-PKP(BC) differential travel times, *Geophys. Res. Lett.*, **23**, 853-856, 1996.

Sylvander, M., B. Ponce, and A. Souriau, Seismic velocities at the core-mantle boundary inferred from P waves diffracted around the core, *Phys. Earth planet. Inter.*, **101**, 189-202, 1997.

Tanaka, S. and H. Hamaguchi, Degree one heterogeneity and hemispherical variation of anisotropy in the inner core from PKP(BC)-PKP(DF) times, *J. Geophys. Res.*, **102**, 2,925-2,938, 1997.

Tkalčić, H., B. Romanowicz, and N. Houy, Constraints on D" structure using PKP(AB-DF), PKP(BC-DF) and PcP-P travel time data from broadband records, *Geophys. J. Int., in press*, 2001.

Tkalčić, H. and B. Romanowicz, Short scale heterogeneity in the lowermost mantle: insights from PcP-P and ScS-S data, *submitted to Earth Planet. Sci. Lett.*, 2001.

Tkalčić, H., D. S. Dreger, and Z. Du, Non-double-couple source mechanisms of Icelanic earthquakes, *in preparation*, 2002.

Tromp, J., Support for anisotropy of the Earth's inner core from free oscillations, *Nature*, **366**, 678-681, 1993.

Tromp, J., Normal-mode splitting observations from the great 1994 Bolivia and Kuril Island earthquakes: constraints on the structure of the mantle and inner core, *GSA Today*, **5**, 137-151, 1995.

U. S. Geological Survey Hazards Program, Long Valley Caldera monitoring Report, 1997.

Vasco, D.W. and L.R. Johnson, Whole earth structure estimated from seismic arrival times, *J. Geophys. Res.*, **103**, 2,633-2,671, 1998.

Vinnik, L., L. Bréger, and B. Romanowicz, Anisotropic structures at the base of the Earth's mantle, *Nature*, **393**, 255-258, 1998.

Wallace, T., J. Given, H. Kanamori, A discrepancy between long-period and short-period mechanisms of earthquakes near the Long Valley caldera, *Geophys. Res. Lett.*, **9**, 1,131-1,134, 1982.

Wallace, T. C., A reexamination of the moment tensor solutions of the 1980 Mammoth Lakes Earthquakes, *J. Geophys. Res.*, **90**, 1,171-1,176, 1985.

Widmer, R., G. Masters, and F. Gilbert, Observably split multiplets-data analysis and interpretation in terms of large-scale aspherical structure, *Geophys. J. Int.*, **111**, 559-576, 1992.

Williams, Q. and E. J. Garnero, Seismic evidence for partial melt at the base of Earth's mantle, *Science*, **273**, 1528-1530, 1996.

Weber, P. and P. Machetel, Convection within the inner core and thermal implications, *Geophys. Res. Lett.*, **19**, 2,107-2,110, 1992.

Wen, L., Seismic evidence for a rapidly-varying compositional anomaly at the base of the Earth's mantle beneath Indian ocean, *submitted to Earth Planet. Sci. Lett.*.

Woodhouse, J. H., D. Giardini, and X.-D. Li, Evidence for inner core anisotropy from splitting in free oscillation data, *Geophys. Res. Lett.*, **13**, 1,549-1,552, 1986.

Wysession, M. E., E. A. Okal, and C. R. Bina, The structure of the core-mantle boundary from diffracted waves, *J. Geophys. Res.*, **97**, 8,749-8,764, 1992.

Wysession, M. E., R. W. Valenzuela, A. Zhu, and L. Bartko, Investigating the base of the mantle using differential travel times, *Phys. Earth planet. Inter.*, **92**, 67-84, 1995.

Wysession, M. E., Large-scale structure at the core-mantle boundary from diffracted waves, *Nature*, **382**, 244-248, 1996.

Wysession, M. E., K. M. Fischer, G. I. Al-eqabi and P. J. Shore, Using MOMA broadband array, ScS-S data to image smaller-scale structures at the base of the mantle, *Geophys. Res. Lett.*, **190**, 167-170, 2001.

Zheng, T. Y., Z. X. Yao, and P. C. Liu, The 14 November 1986 Taiwan earthquake - an event with isotropic component, *Phys. Earth planet. Inter.*, **91**, 285-298, 1995.